Impact of strain and composition on structural and piezo-/ferroelectric properties of epitaxial $NaNbO_3$ and $K_xNa_{1-x}NbO_3$ thin films and superlattices grown by PLD

vorgelegt von

Diplom-Physiker

Jan Sellmann

geb. in Lippstadt

von der Fakultät II – Mathematik und Naturwissenschaften

der Technischen Universität Berlin

zur Erlangung des akademischen Grades

Doktor der Naturwissenschaften

Dr. rer. nat.

genehmigte Dissertation

Promotionsausschuss:

Vorsitzende: Prof. Dr. rer. nat. Regine von Klitzing

Gutachter: Prof. Dr.-Ing. Matthias Bickermann

Gutachter: Prof. Dr. rer. nat. Michael Lorenz

Tag der wissenschaftlichen Aussprache: 21. Mai 2015

Berlin 2016

Abstract

The subject of this thesis is the systematic study of the impact of pulsed laser deposition (PLD) conditions on the growth mode, strain state and film composition of ferroelectric $NaNbO_3$ and $K_xNa_{1-x}NbO_3$ thin films and superlattices. Lattice mismatched (011)$NdGaO_3$, (001)$SrTiO_3$, (011)$DyScO_3$, (011)$TbScO_3$ and (011)$NdScO_3$ single crystalline substrates have been used in order to induce tensile or compressive biaxial lattice strain of different magnitude in the films.
Coherent 2D growth of thin $NaNbO_3$ films was achieved by optimizations of the growth process. The key interests were to adjust the deposition conditions allowing for near stoichiometric film growth and to analyze the dependence of ferroelectric domain formation and local hysteresis loops on the composition of films, incorporating different biaxial lattice strains.
The amount of sodium and oxygen vacancies in the films was found to be critically affected by the oxygen background pressure and the Na/Nb ratio in the applied targets. By increasing the oxygen pressure from 0.05 mbar to 2 mbar or the Na/Nb ratio in the targets up to 1.17, a substantial reduction of sodium and oxygen vacancies was achieved. No extended defects were found in fully tensilely strained films deposited under thus optimized deposition conditions. In contrast, in compressively strained films deposited under otherwise identical conditions, the presence of columnar defects was observed, which provide stress relief in compressively strained films.
In films incorporating full tensile lattice strain, regular lateral ferroelectric a_1/a_2 domain patterns were obtained only in the case of near-stoichiometric growth. In ferroelectric films under partially relaxed tensile lattice strain, typically $a_1/c/a_2/c$ patterns are observed. In partially relaxed PLD-grown $NaNbO_3$ films, additionally a vertical polarization evolves, resulting in an a_1c/a_2c domain pattern.
Distinct local ferroelectric hysteresis loops were observed in near-stoichiometric films under low compressive lattice strain. Thus, it was confirmed that a ferroelectric room temperature phase can be induced by biaxial lattice strain in $NaNbO_3$, which is antiferroelectric in the unstrained state.
In the case of $K_xNa_{1-x}NbO_3$, the key interest was to investigate the impact of K/Na ratio and biaxial lattice strain on local piezoelectric coefficients. It was found that the thickness up to which $K_xNa_{1-x}NbO_3$ films could be deposited in a 2D-growth mode is lower compared to $NaNbO_3$ films, which is correlated to the amount of incorporated K. As a promising alternative to the growth of single films, superlattices with alternating layers under compressive and tensile lattice strain were deposited on $DyScO_3$ substrates. This way, both 2D growth and full in-plane lattice strain of the individual layers were retained for remarkably increased thicknesses compared to single films.
In agreement with theoretical predictions made for ferroelectric/ferroelectric superlattices, 2D-grown, fully strained $NaNbO_3/K_{0.5}Na_{0.5}NbO_3$ superlattices on $DyScO_3$ substrates were found to exhibit very promising local piezo/ferroelectric properties.

Zusammenfassung

Das Ziel dieser Arbeit war die systematische Untersuchung des Einflusses von Wachstumsbedingungen der Laserstrahlverdampfung (PLD) auf den Wachstumsmodus, den Verspannungszustand und die Zusammensetzung von $NaNbO_3$- und $K_xNa_{1-x}NbO_3$-Dünnschichten und Übergittern. Einkristalline (011)$NdGaO_3$, (001)$SrTiO_3$, (011)$DyScO_3$, (011)$TbScO_3$ und (011)$NdScO_3$ Substrate mit kontrollierter Gitter-Fehlanpassung wurden verwendet, um biaxial kompressive oder tensile Gitterverspannungen in den Filmen zu erzeugen.
Im Fall von $NaNbO_3$ lag der Fokus auf der Erforschung von Abscheidebedingungen, die ein nahezu stöchiometrisches, 2D Film-Wachstum ermöglichen. Es wurde untersucht, wie sich Sauerstoff- und Natriumvakanzen auf (i) die ferroelektrische Domänenbildung in tensil und (ii) lokale Hysteresen in kompressiv verspannten Filmen auswirken.
Es wird gezeigt, dass die Dichte von Natrium- und Sauerstoffvakanzen kritisch von dem Sauerstoffhintergrunddruck während des Wachstums und dem Na/Nb-Verhältnis des verwendeten Targets abhängt. Eine signifikante Verringerung dieser Vakanzdichte konnte sowohl durch Anheben des Sauerstoff-Hintergrunddruckes von 0,05 auf 2 mbar, als auch durch die Verwendung eines Targets mit einem Na/Nb-Verhältnis von 1,17 erreicht werden.
In nahezu stöchiometrischen, tensil verspannten Filmen wurden keine ausgedehnten Defekte beobachtet. Im Gegensatz dazu sind säulenartige Defekte in kompressiv verspannten Filmen präsent, die unter ansonsten identischen Wachstums-Bedingungen abgeschieden wurden. Es wurde ermittelt, dass dieser Defekt-typ in der Lage ist, kompressive Verspannung in den Filmen abzubauen.
In tensil verspannten Filmen konnten gut geordnete laterale ferroelektrische a_1/a_2 Domänen nur beobachtet werden, wenn die Filme nahezu stöchiometrisch waren. Die Art der Domänenkonfiguration in Filmen unter reduzierter tensiler Verspannung (a_1c/a_2c) weicht deutlich von üblicherweise beobachteten $a_1/c/a_2/c$ Domänen ab.
Gut ausgeprägte lokale ferroelektrische Hysteresen konnten in nahezu stöchiometrischen Filmen unter geringer kompressiver Verspannung nachgewiesen werden. Damit wurde bestätigt, dass bei Raumtemperatur durch Gitterverspannung eine stabile ferroelektrische Phase in $NaNbO_3$ erzeugt werden kann, welches im relaxierten Zustand antiferroelektrisch ist.
Im Fall von $K_xNa_{1-x}NbO_3$ lag das Hauptaugenmerk auf der Untersuchung des Zusammenhanges zwischen dem K/Na-Verhältnis und Gitterverspannungen auf der einen und den lokalen piezoelektrischen Koeffizienten auf der anderen Seite. Dabei wurde 2D-Wachstum von voll kompressiv verspannten Filmen gegenüber nahezu stöchiometrischer Film-Abscheidung priorisiert. Die Dicke, bis zu der glatte $K_xNa_{1-x}NbO_3$-Schichten abgeschieden werden konnten war deutlich geringer als im Fall von ähnlich verspannten $NaNbO_3$ Filmen. Als alternativer Ansatz wurde die Abscheidung von Übergittern mit alternierenden Schichten unter kompressiver und tensiler Verspannung auf $DyScO_3$ Substraten verfolgt. Auf diese Weise war es möglich sowohl 2D-Wachstum als auch voll kompressiv verspannte Systeme für signifikant dickere Schicht-Stapel im Vergleich zu Einzelschichten zu erreichen.
Theoretische Vorhersagen lassen auf exzellente ferro/piezoelektrische Eigenschaften von Übergittern aus zwei ferroelektrischen Materialien schließen. In dieser Arbeit wird gezeigt, dass 2D-gewachsene und voll kompressiv verspannte $NaNbO_3/K_{0.5}Na_{0.5}NbO_3$-Übergitter auf $DyScO_3$ Substraten viel versprechende lokale piezoelektrische Eigenschaften haben.

Publications in international Journals

M. Schmidbauer, J. Sellmann, D. Braun, A. Kwasniewski, A. Duk, and J. Schwarzkopf, „Ferroelectric domain structure of $NaNbO_3$ epitaxial thin films grown on (110) $DyScO_3$ substrates", *Physica Status Solidi RRL*, pp. 1–5, 2014.

J. Sellmann, J. Schwarzkopf, A. Kwasniewski, M. Schmidbauer, D. Braun, and A. Duk, "Strained ferroelectric $NaNbO_3$ thin films: Impact of pulsed laser deposition growth conditions on structural properties", Thin Solid Films, vol. 570, pp. 107-113, 2014.

Conference presentations

J. Sellmann, J. Schwarzkopf, A. Duk, A. Kwasniewski, M. Schmidbauer, R. Fornari; "Growth of strained, ferroelectric $NaNbO_3$ thin films by pulsed laser deposition" (oral); DPG Spring Meeting of the Condensed Matter Division (Berlin, 2012-03-25 - 2012-03-30)

J. Sellmann, J. Schwarzkopf, A. Duk, A. Kwasniewski, M. Schmidbauer, R. Fornari; "Growth of strained piezoelectric $NaNbO_3$ thin films by pulsed laser deposition" (oral); SuperFOx-2012 (Como (IT), 2012-06-09 - 2012-06-12)

J. Sellmann, J. Schwarzkopf, A. Duk, A. Kwasniewski, M. Schmidbauer, S. Gnanapragasam, T. Markurt, R. Fornari; "Investigation of growth conditions on structural and ferroelectric properties of strained $NaNbO_3$ thin films grown by PLD" (oral); DPG Spring Meeting of the Condensed Matter Division (Regensburg, 2013-03-10 - 2013-03-15)

J. Sellmann, J. Schwarzkopf, A. Duk, D. Braun, S. Gnanapragasam, A. Kwasniewski, M. Schmidbauer, T. Markurt, R. Fornari; „Epitaxial PLD-Growth of strained Ferroelectric $K_xNa_{1-x}NbO_3$ thin films" (poster); European Materials Research Socitey, Spring Meeting (Strasbourg, FR, 2013-05-27 - 2013-05-31)

J. Sellmann, J. Schwarzkopf, A. Duk, D. Braun, S. Gnanapragasam, A. Kwasniewski, M. Schmidbauer, T. Markurt, P. Müller, M. Albrecht; „Growth of epitaxially strained, ferroelectric $NaNbO_3$ thin films by Pulsed Laser Deposition" (oral); 14. Kinetikseminar (Berlin, Germany, 2013-11-21 - 2013-11-22)

J. Sellmann, J. Schwarzkopf, D. Braun, A. Duk, A. Kwasniewski, M. Schmidbauer; "Epitaxial PLD-Growth of strained Ferroelectric $K_xNa_{1-x}NbO_3$ thin films and superlattices" (oral); DPG Spring Meeting of the Condensed Matter Division (Dresden, 2014-03-30 - 2014-04-04)

J Sellmann, J. Schwarzkopf, D. Braun, A. Kwasniewski, M. Schmidbauer; "Film ratio dependece of piezo/ferroelectric properties in strained $K_{0.5}Na_{0.5}NbO_3$-based superlattices on $DyScO_3$" (oral); European Materials Research Socitey, Fall Meeting 2014 (Warsaw, PL, 2014-09-15 - 2014-09-18)

Contents

List of Abbreviations

1D	One Dimensional
2D	Two Dimensional
AFM	Atomic Force Microscopy
DART	Dual AC Resonance Tracking
EDX	Energy Dispersive X-Ray Spectroscopy
FeRAM	Ferroelectric Random Access Memory
GIXD	Grazing Incidence X-Ray Diffraction
HAADF-STEM	High Angular Dark Field Scanning Transmission Electron Microscopy
HR-XRD	High-Resolution X-Ray Diffraction
HRTEM	High-Resolution Transmission Electron Microscopy
ICP-OES	Inductively Coupled Plasma Optical Emission Spectroscopy
LPFM	Lateral Piezoresponse Force Microscopy
MBE	Molecular Beam Epitaxy
MOCVD	Metal-Organic Chemical Vapor Deposition
o	Orthorhombic (unit cell)
oop	Out-of-Plane
pc	Pseudocubic (unit cell)
PFM	Piezoresponse Force Microscopy
PLD	Pulsed Laser Deposition
PZT	Lead Zirconate Titanate
RE	Rare-Earth
RHEED	Reflection High Energy Electron Diffraction
RMS	Root Mean Square
RSM	Reciprocal Space Map / Mapping
SAW	Surface Acoustic Wave
SEM	Scanning Electron Microscopy
TEM	Transmission Electron Microscopy
VPFM	Vertical Piezoresponse Force Microscopy

Introduction

Metal-oxides in general and perovskites in particular are known to exhibit an exceptionally large variety of functionalities. These properties include, but are not limited to, large dielectric constants [1] and piezo- and/or ferroelectric [2], ferromagnetic [3], superconducting [4] and non-linear optical properties [5], which depend strongly on the precise structure and composition of the materials. The reproducible growth of perovskite ceramics and single crystals (e.g. piezoelectric $PbZr_xTi_{1-x}O_3$ and frequency-doubling $KNbO_3$) is already successfully pursued for decades [4]. In contrast, growth of thin films is a major topic of current research. Film deposition offers some advantages in opposite to bulk crystal growth. It allows the combination of complex metal-oxides with different electronic components and thus enables the fabrication of multifunctional devices. For example, the coupling of ferroelectric and ferromagnetic components at the interface of film heterostructures provides access to the fabrication of multiferroic memory devices [6]. Furthermore, the interface between two adjacent materials can give rise to new effects, which are not found in the bulk material, for example, the formation of a 2D-electron gas at the $LaAlO_3/SrTiO_3$ interface [7]. Additionally, through the use of tailored lattice mismatch between substrates and films, biaxial lattice strain can enhance individual functional properties [8] or induce properties which do not exist in corresponding bulk material (for instance ferroelectricity in $SrTiO_3$ [9]). Via oriented growth, the film´s anisotropy can be tuned for applications e.g. relying on vertical (FeRAM) or lateral (SAW) electric polarization, further enhancing the versatility of metal-oxides [10].

Piezoelectric and ferroelectric perovskite compounds in particular are used in a wide range of applications, e.g. in actuators [11], resonators [12], transducers [13] and non-volatile ferroelectric RAM [14]. The most prominent materials for large-scale industrial production are lead-titanate based compounds such as $PbZr_xTi_{1-x}O_3$ (PZT). The advantages of PZT are high electromechanical coupling coefficients and excellent ferro- and dielectric properties [15]. In contrast, they exhibit environmental [16] and long-term functional problems, like ferroelectric fatigue [17] and degeneration effects [18]. Several alternative materials with promising piezo- and ferroelectric properties are under thorough investigation, including $BaTiO_3$ [19] and $BiFeO_3$ [8]. It has been demonstrated in detail that in these materials the biaxial lattice strain affects the Curie temperature and electric polarization direction [20], to name only a few. Solid solutions of different perovskites often exhibit one or more phase transitions where phase symmetry changes. Remanent polarization and piezoelectric coefficients have been found to be enhanced by exploiting the fact, that a morphotropic phase boundary exists [21], separating different phases of solid solutions with different parent material ratios, for instance in $PbZr_xTi_{1-x}O_3$.

Lead-free alkali niobates such as $NaNbO_3$, $KNbO_3$ and their solid solutions $K_xNa_{1-x}NbO_3$ show very promising piezo- and ferroelectric properties as bulk ceramics and single crystals [22].

Compared to many other ferroelectric materials, $NaNbO_3$ has small lattice parameters. Thus there are several closely lattice matched substrates available, inducing tensile biaxial lattice strain in thin films, (e.g. $DyScO_3$ and $TbScO_3$). Ferroelectric thin films with tensile strain are known to exhibit domain configurations not present in bulk materials. For example, the presence of $a_1/a_2/a_1/a_2$-domains [23] with exclusive in-plane polarization or a/c-domains with alternating vertical and lateral polarization has been reported [24]. However, the high volatility of Na_2O and K_2O [25] entails difficulties for the growth of near stoichiometric alkali-niobate thin films. The formation of well-ordered domain arrangements depends crucially on the number of point defects such as vacancies in the films [26]. Thus, the presence of regularly arranged domains can serve as an indicator for near-stoichiometric film growth. However, rarely papers deal with the growth of epitaxial $(Na,K)NbO_3$ thin films. No systematic study of the correlation between deposition conditions, film structure and their ferroelectric properties has been performed, which is indispensable for optimizing film properties. Prior to this work (i.e. before July 2011) no publications on fully strained $NaNbO_3$ or $K_xNa_{1-x}NbO_3$ films and the influence of incorporated lattice strain on their domain formation/ferroelectric properties have been made.

In the present work, the combined availability of suitable single crystalline substrates and measurement techniques allowed the detailed investigation of the impact of PLD-growth conditions on growth mode, composition and subsequently the formation of ferroelectric domains and hysteresis curves of fully strained $NaNbO_3$ films. Such a systematic study for the promising class of alkaline niobates has not been published in literature yet, and will potentially allow the targeted adjustment of film properties by the choice of the deposition parameters and substrate material.

For bulk materials, an enhancement of the piezoelectric response is observed, when Na in $NaNbO_3$ is partially replaced by K, forming the solid solution $K_xNa_{1-x}NbO_3$, with $x = 0.5$ generally yielding the most promising results [22, 27, 28].

In the case of piezoelectric properties, the influence of point defects is considered to be significantly less pronounced than in the case of domain formation. Thus, for $K_xNa_{1-x}NbO_3$ thin films, achieving 2D growth of fully compressively strained films is prioritized over near stoichiometric film deposition.

The growth of superlattices allows retaining 2D growth as well as full in-plane lattice strain to higher film thicknesses. Thereby, several different films are deposited, alternating between tensile and compressive lattice strain. Additionally, ferroelectric/ferroelectric superlattices are predicted to exhibit excellent piezo/ferroelectric properties [29]. However, only very few experimental reports on the growth and the resulting ferroelectric properties of these structures have been made and in particular none of them for $NaNbO_3/K_xNa_{1-x}NbO_3$ superlattices.

Chapter 1 briefly introduces materials with perovskite-like structure, piezo-and ferroelectricity, epitaxial film growth and biaxial lattice strain, including some theoretical aspects.

Chapter 2 describes PLD method for epitaxy and the subsequent material characterization used in the course of this work, focusing on pulsed laser deposition and x-ray diffraction techniques.

Chapter 3 describes the materials employed as substrates and for film growth.

Chapter 4 presents the preparation and characterization of the PLD-targets used for film deposition.

Chapter 5 states results on how PLD growth conditions and target composition affect (i) stoichiometry, orientation and strain state of $NaNbO_3$ films and (ii) the ferroelectric domain configuration and hysteresis loops.

Chapter 6 focuses on the impact of compositional changes with regard to the K/Na ratio of 2D-grown $K_xNa_{1-x}NbO_3$-based films and superlattices under several distinct biaxial lattice strains, with a detailed description and analysis of structural and piezo/ferroelectric properties of ferroelectric/ferroelectric $NaNbO_3/K_{0.5}Na_{0.5}NbO_3$ and paraelectric/ferroelectric $SrTiO_3/K_{0.5}Na_{0.5}NbO_3$ superlattices on $DyScO_3$ substrates.

Chapter 1: Basic Principles

1.1 Perovskites

All substrate and film materials studied in this work are of the general composition ABO_3 with A being mono- to trivalent and B tri- to pentavalent cations. This group of materials is usually called perovskite. The name goes back to the Russian mineralogist and politician Lew Alexejewitsch Perowski, who first found the mineral $CaTiO_3$ in the Ural Mountains. Most materials of the ABO_3 type do not have a cubic structure. Depending on composition, pressure and temperature they rather exhibit cubic, tetragonal, orthorhombic and rhombohedra symmetries.

A common empirical approach to characterize the stability of perovskites is the Goldschmidt tolerance factor [30]. It is calculated from the ionic radii of the A (R_A), B (R_B) and O (R_O) ions:

$$t = \frac{R_O + R_A}{(R_O + R_B)\sqrt{2}} \quad (1.1).$$

Materials with a tolerance factor $t > 1.05$ (A-cations too large) or $t < 0.71$ (cations are too small, $R_A \approx R_B$) do not crystalize in the perovskite structure under equilibrium conditions [31].

As a typical example for cubic perovskites serves $SrTiO_3$, which crystallizes in a structure with Pm-3m space group at room temperature (RT), see Fig. 1.1(a). The A (Sr^{2+}) cation is located in the cube´s center, the B (Ti^{4+}) cations on the cube´s corners and the O^{2-} anions in the center between the B cations. This way regular BO_6-octahedra are formed. The symmetry of the BO_6-octahedra strongly determines the materials piezo- and ferroelectric properties. Due to the centro-symmetric structure of cubic perovskites, no piezoelectric effect occurs. Most perovskites undergo phase transitions at certain temperatures, however, resulting in non-cubic structures.

In the case of tetragonal crystal structure, the central B-cation is shifted up- or downwards along the long axis whereas the oxygen anions are shifted in the opposite direction. This can result in the formation of a local build in electric field which strongly determines the piezo- and ferroelectric properties, see chapter 1.2 (Principles of Piezo- and Ferroelectricity) for further details. For example, bulk $KNbO_3$ ($t \sim 0.96$) exhibits the tetragonal phase (Amm2 or Bmm2) in the temperature range between 225 °C and 435 °C [32].

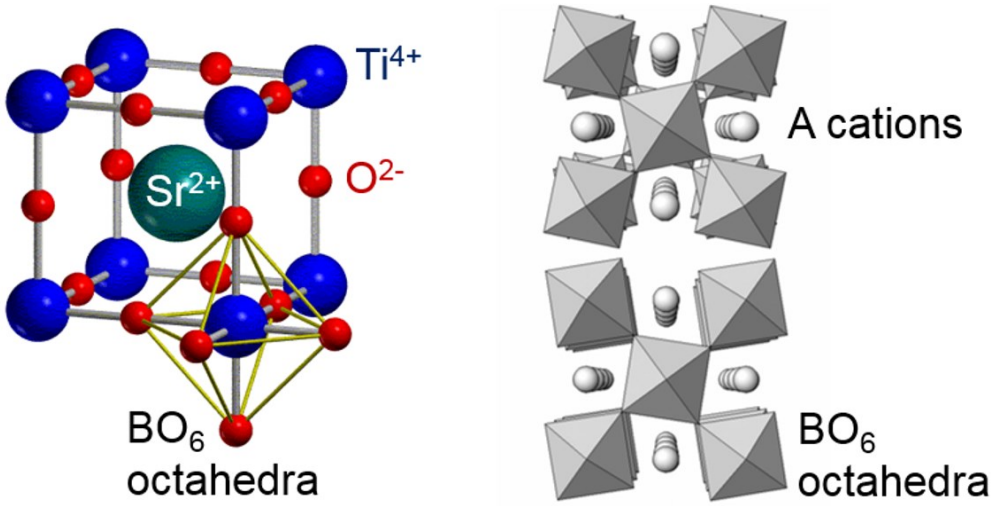

Fig. 1.1: (a) Cubic $SrTiO_3$ in the space group Pm-3m, adapted from [33], (b) rotation of the BO_6 octahedra in the tetragonal I4/mcm (top – $a^0a^0c^-$) and the P4/mbm (bottom - $a^0a^0c^+$) space group viewed down the c-axis. Adapted from [34]. The B-site cations are located at the center of the octahedra.

If the Goldschmidt tolerance factor *t* is less 0.9, then the A ions are too small to fill the octahedral interstices. These empty regions in the lattice can be minimized by rotating and tilting the BO_6-octahedra. Accordingly, the oxygen anions are not located at the center of the cube´s faces anymore, which results in a reduction of the symmetry and more complex unit cells as compared to tetragonal space groups I4/mcm (Fig. 1.1(b), top) and P4/mbm (Fig. 1.1(b), bottom).

Depending on the octahedral rotations, there can be different tetragonal, orthorhombic and rhombohedral structures The Glazer notation gives an adequate description. This model is based only on the differing lattice parameters and the octahedra rotations around the three original cubic axes of the BO_6 octahedra [35]. The orthogonal axes x, y, z are equivalent to the ones of the aristotype cubic cell. The letters a, b and c are here used to imply unequal magnitudes of the rotations. E.g. if the magnitude of rotation is equal in all three directions only the letter “a” is used. The superscript “0” implies no rotation around the corresponding axis whereas “-“ and “+” denote the phase of the rotation relative to the neighboring layers. Rotations out of phase (in phase) are labeled with the superscript “-“ (“+”). In this way, undistorted systems (e.g. $SrTiO_3$ and $KNbO_3$ at RT) are given by $a^0a^0a^0$. The difference between out of phase and in phase rotations are visualized in Fig. 1.1(b) by looking along the c-axis on the tilt systems $a^0a^0c^-$ (top) and $a^0a^0c^+$ (bottom).

At RT bulk $NaNbO_3$ (space group Pbcm) exhibits the rather complicated tilt system of $a^-b^+a^-/a^-b^-a^-$ [36]. Here, the rotations around the x- and z-axes are equal in magnitude and out of phase with respect to their next neighbor (Fig. 1.2(a)). The rotation around the y-axis is different in

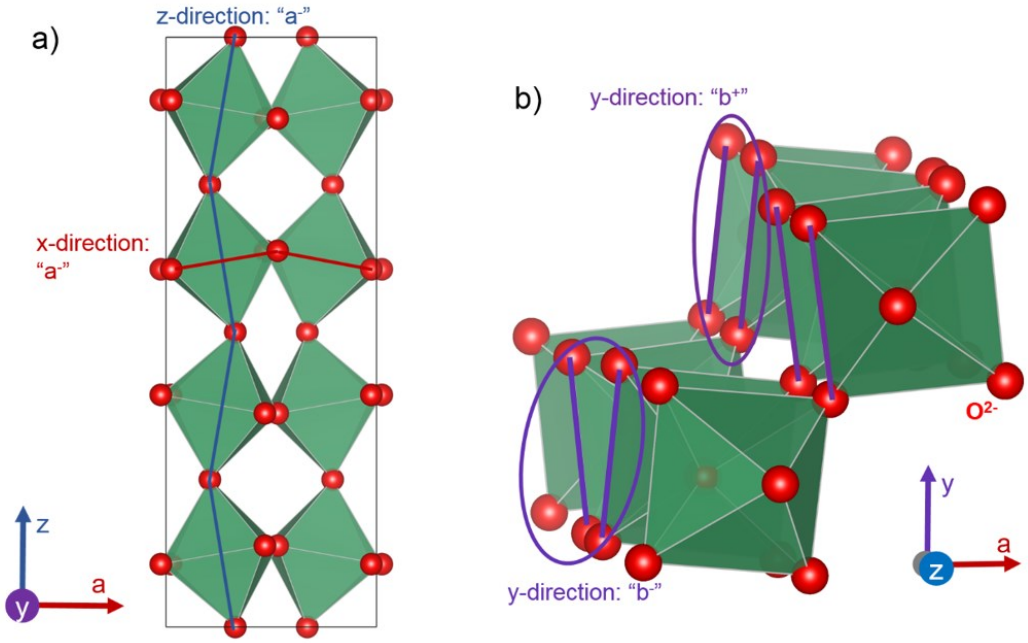

Fig. 1.2: Orthorhombic space group Pbcm of bulk $NaNbO_3$ at RT visualizing the octahedra rotations (a) in x- and z- direction and (b) in y-direction. Na and Nb ions not shown.

magnitude. Also, in phase and out of phase rotations of the next neighbors alternate (Fig. 1.2(b)). The resulting orthorhombic unit cell consists of eight pseudocubic subcells.

In certain orthorhombic perovskites (e.g. $NaNbO_3$), there is a shift of the B-cation out of the central position of a few tenth of an angstrom (Å), similar to the case described for tetragonal perovskites. In this way, a transition arises from a non-polar to a polar state, inducing piezo-, ferro- or antiferroelectric behavior. The direction of the polarization is strongly determined by the rotation of the BO_6-octahedra. For example, in bulk $NaNbO_3$ at RT the polarization direction of the b^- tilted subcells is out-of-phase with respect to the b^+ tilted subcells, resulting in an anti-ferroelectric system.

Typical examples for ferroelectric perovskites are materials based on $PbTiO_3$, $BaTiO_3$ or $(Na,K)NbO_3$.

Except for $SrTiO_3$, all other film and substrate materials used in this work are orthorhombic at room temperature. The employed substrates exhibit no intrinsic piezoelectric properties.

1.2 Principles of Piezo- and Ferroelectricity

1.2.1 Definitions of piezo-, pyro- and ferroelectricity

A material is piezoelectric if external mechanical forces can change its polarization along one or more directions. The resulting electric field induces a voltage across the specimen, typically depending in a linear fashion on the applied pressure (direct piezoelectric effect). This effect is reversible. In the converse case, the material can be deformed when exposed to an electric field (reverse piezoelectric effect).

Piezoelectric behavior can only occur in polar systems and is therefore directly related to the structural symmetry of the crystals. Of the 32 crystal classes (point groups) 11 classes exhibit an inversion center and are thus non-polar (see Fig. 1.3). 21 point groups are non-centrosymmetric, only one of them - point group 432 - exhibits no piezoelectricity. Of the remaining 20 piezoelectric point groups, 10 are pyroelectric, which means that they exhibit a single unique polarization axis.

The pyroelectric effect is defined as the ability of a material to react to a temporal temperature change with a separation of charge [37]. A change in temperature therefore results in a change in polarization. Such a behavior is possible only in materials with a single unique polar direction axis. Therefore, a pyroelectric material is always piezoelectric but not necessarily vice versa.

A ferroelectric material is characterized by (i) its ability to exhibit a spontaneous electric polarization in two possibly antiparallel directions and (ii) the possibility to switch the polarization direction by an external electric field. Ferroelectric behavior will be explained in more detail in the following section.

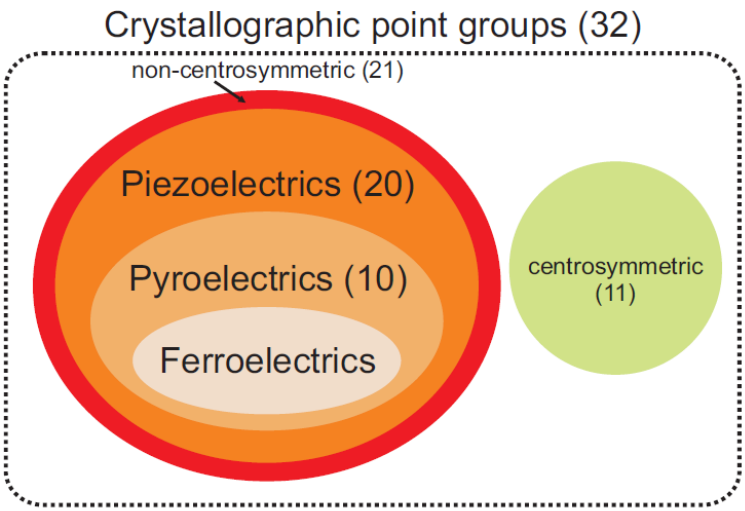

Fig. 1.3: Schematic illustration of the relationships between piezo-, pyro- and ferroelectric point groups (from [38]).

1.2.2 Ferroelectricity

The occurrence of a spontaneous polarization alone does not necessarily result in a ferroelectric behavior. On top of that, the spontaneous polarization has to be reversible by applying a suitable external electric field. An example for a pyroelectric but not ferroelectric material is GaN; here, a reversal of the internal electric field would require the exchange of Ga^{3+} and N^{3-} planes.

The polarization of ferroelectric perovskites originates from the displacement of the B-cations relative to the center position of the unit cell [39].The polarization *P* is defined as the dipole moment per unit volume, averaged over the volume of a unit cell [39]. The total dipole moment depends linearly on the displacement length [40].

However, ferroelectricity is an effect not confined to one single cell. Instead, various factors contribute to overall macroscopic polarization [41]. Among those factors are electrical and mechanical boundary conditions, which critically depend on the employed substrate and the composition and thickness of the ferroelectric material itself, depolarization fields and the electrodes [42].

1.2.3 Ferroelectric Domains

In practice, the direction of spontaneous polarization in ferroelectric materials is generally not uniform over the whole crystal. Electric dipoles contributing to the spontaneous polarization may align in certain small sub regions of a crystal. These regions are called *ferroelectric domains*. The interface between such regions is called *domain wall*. While in ferromagnetic materials the magnetic orientation varies gradually between two adjacent domains (resulting in large domain walls [39]), the change of electric dipole orientation in ferroelectric materials is rather abrupt. Thus, the thickness of ferroelectric domain walls is only about a few lattice unit cells lengths. The classification of domain patterns is based on the direction of and the angle between the polarization vectors of adjacent domains (in orthorhombic systems typically 60°, 90°, 120° or 180°). Although further possibilities exist, e.g., polarization directions like M_i and r (exhibiting both lateral and vertical polarization components), here I will concentrate on the c, a_1 and a_2 polarizations and their combinations.

The c direction is used for out of plane polarizations. c domains are separated by an angle of 180° (180° domains), so that in one domain the polarization points upwards while in the neighboring domains the polarization points downwards (Fig. 1.4(a)).

Two examples for 90° domains are a_1/a_2 domains, where both polarization directions lie in the plane (Fig. 1.4(b)), and a_1/c-domains (Fig. 1.4(c)) exhibiting alternating domains with only lateral (a_1) and vertical (c) polarization components. In 90° domains the domain walls can be electrically neutral (head to tail arrangement) or charged (head to head arrangement), although

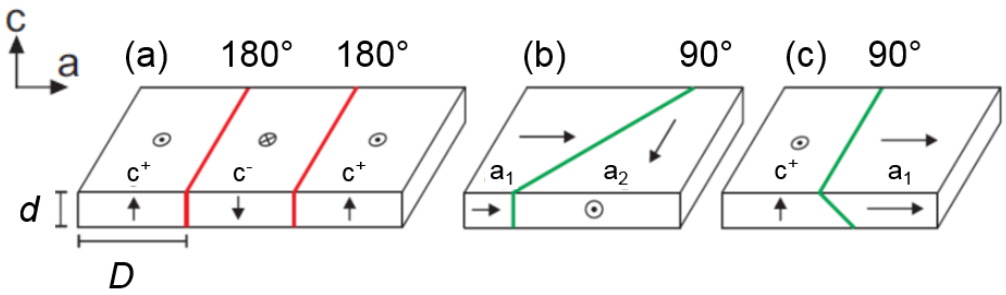

Fig. 1.4: Examples for possible ferroelectric domain configurations: (a) 180° c-domains, (b) 90° a_1/a_2-domains and (c) 90° a_1/c-domains with head to tail configuration. With *d* the film thickness and *D* the domain width. Adapted from [38].

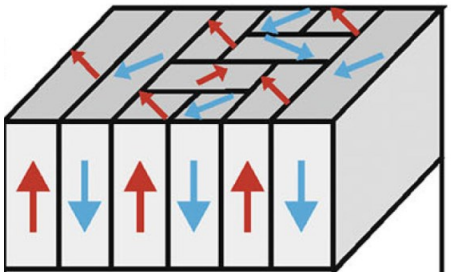

Fig. 1.5: Visualization of a coexistence of a_1, a_2 and c polarization components in individual domains [43].

the neutral head to tail arrangement is generally considered to be energetically more favorable [44].

A coexistence of vertical (c) as well as lateral (a_1, a_2) polarization components in one domain is also possible (Fig. 1.5) [45].

Two main aspects of domain formation have to be considered:

(a) In-plane domains of laterally polarized materials with a phase change of the polarization of 90° relative to their next neighbors were found to reduce mechanical stress at the film-substrate interface [46]. They are therefore called ferroelastic domains. However, in some cases, the polarization direction of ferroelastic domains was found to be impossible to switch. These domains are thus not ferroelectric.

(b) In films with a polarization component perpendicular to the basal plane, a depolarization field is formed by charge accumulation at the film's surface and interfaces. The charge accumulation responsible for the depolarization field can be neutralized macroscopically by the formation of alternating domains, with vertical polarization components pointing up and down respectively. While the suppression of the depolarization field reduces the free energy

by W_E, the formation of domain walls leads to an increase of the free energy by W_W. These energies can be expressed as [41]:

$$W_E = \frac{\varepsilon^* D V P_0^2}{d} \quad (1.2).$$

$$W_W = \frac{\sigma V}{D} \quad (1.3).$$

D is the domain width, P_0 the domain polarization, V the crystal volume and d the crystal thickness. ϵ^* depends on the dielectric constant of the ferroelectric material [38] and σ is the energy per unit area of the domain wall. Analogous to the width of ferromagnetic domains described by Landau and Lifschitz [47] and Kittel [48], the minimization of both energies $W_E - W_W = 0$ gives a square root dependence of the domain width on the crystal thickness in equilibrium of the form [46]:

$$D = \sqrt{d \frac{\sigma}{\varepsilon^* P_0^2}} \quad (1.4).$$

In the derivation of the preceding equations, the interactions of e.g. free charge carriers, internal stress or defects have not been considered. They can result in a variety of domain structures in real films. If the film thickness is very small, the square root dependence in Eq. 1.4 is not applicable for lateral 90° ferroelastic domains. Under these circumstances elastic interactions between the domains and the substrate extend over distances exceeding the film thickness ($D > t$) [46, 49, 50].

This idealized picture of domain formation, however, does not fully explain the domain arrangement of complex ferroelectric systems where the origin of ferroelectric domains is not fully understood.

1.2.4 Ferroelectric hysteresis loop

The ferroelectric hysteresis loop of the polarization P is a double-valued function of the applied electric field E [51].

A typical P-E hysteresis loop is depicted in Fig. 1.6. In an unpoled state, domains with polarization directions up and down are equally present and the starting point of the macroscopic polarization is zero (O).

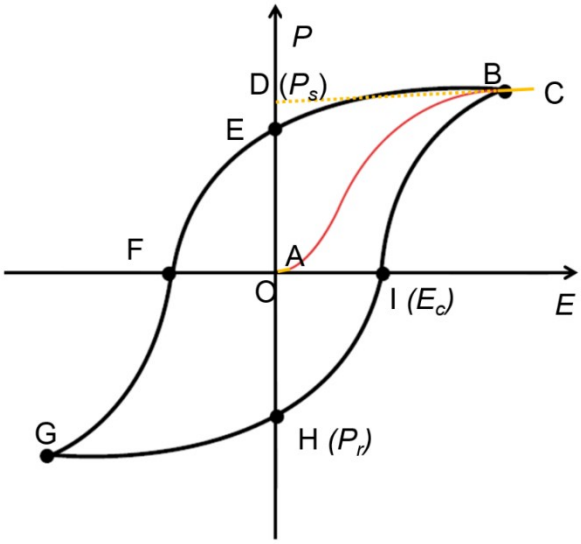

Fig. 1.6: Typical *P-E* ferroelectric hysteresis loop.

At first (O to A) the polarization depends linearly on the electric field similar to the case of a paraelectric material [52]:

$$P = \varepsilon_0(\varepsilon_r - 1)E \quad (1.5).$$

Here, the electric field is not sufficient to switch domains. With increasing electric field (A to B) a rising fraction of domains opposing the external electric field are switched and contribute to the increased net polarization until all ferroelectric domains are directed along the external field. This results in saturation in which a single macroscopic monodomain is formed below the contact pads. The remaining linear component (B to C) can be used to extrapolate the spontaneous polarization P_s without external electric field (D).

As the external field weakens, a significant reduction of the polarization is observed (C to G) but remains non-zero when the electric field is zero (E). The retained value is the remanent polarization P_r. At this point some domains of opposite polarity have formed (in a real ferroelectric material) but a net macroscopic polarization remains along the direction of the electric field applied before.

When the electric field reaches a certain (negative) value E_c (coercive field strength), the remanent polarization can be removed (F). A continued decrease of the electric field to higher negative values results again in reaching single macroscopic domain status but with opposite polarization direction (G). Increasing the external electric field results in a similar behavior as described before (G to C).

1.2.5 Phase transitions and Curie temperature

Most ferroelectric materials exhibit at least one paraelectric cubic phase at high temperatures. Upon cooling, the material undergoes a phase transition from para- to ferroelectric. The corresponding transition temperature is called the Curie temperature or Curie point T_c. Commonly; one distinguishes between first-order and second-order phase transitions. First-order phase transitions experience a discontinuity in P_s at T_c (Fig. 1.7(a)) with a finite maximum of the permittivity ε at this point, which can be orders of magnitude higher as compared to other temperatures [39, 40]. Second-order phase transitions are continuous in P_s but discontinuous in dP_s/dT at T_c (Fig. 1.7(b)) [53], resulting in exceptionally large dielectric constants in vicinity of the transition point.

In order to visualize a paraelectric to ferroelectric phase transition it is useful to consider the behavior of $BaTiO_3$. At temperatures above the Curie point (T_c), $BaTiO_3$ is cubic with the oxygen anions at the face centers, the titan cations in the cube centers and the barium cations on the cube corners (see Fig. 1.8(a)). The system is non-polar. In particular, the position of barium serves as an inversion center. Cooling the system below T_c gives rise to a structural phase transition, which transforms the cubic structure into a tetragonal one (Fig. 1.8(b)). This phase (P4mm) has a polar axis along the elongated tetragonal axis. The crystal exhibits minimal energy when the Ti^{4+} ion is shifted either upwards or downwards from the center of the unit cell. Both positions are energetically equivalent. The displacement of the Ti^{4+} ion results in a shift of the oxygen ions in the opposite direction. The resulting charge separation thus generates the corresponding spontaneous polarization.

Further cooling of the material results in additional phase changes to orthorhombic and rhombohedral at 5°C and -90°C, respectively [54]. Notably, $BaTiO_3$ exhibits a typical phase transition sequence for ferroelectric materials. While $KNbO_3$ has similar phase transitions, $NaNbO_3$ is more complicated as will be discussed in chapter 3 (Materials).

In more complex materials with a Goldschmidt tolerance factor of typically less than 0.9 also rotations and/or tilting of the BO_6 octahedra occur, see Chapter 1.1 (Perovskites).

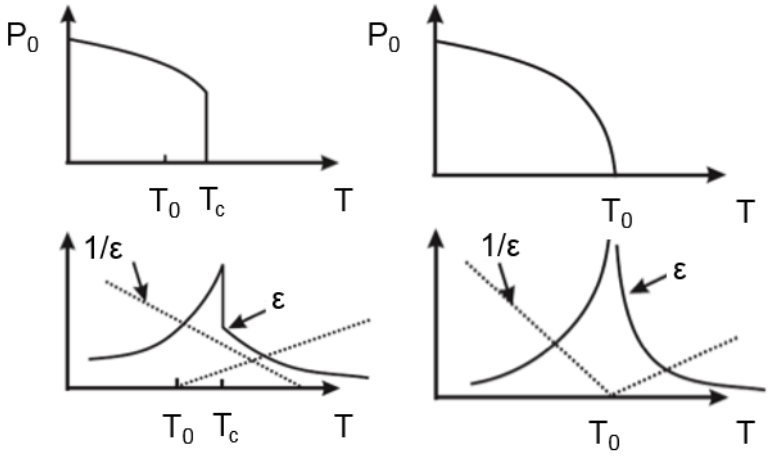

Fig. 1.7: (a) first order and (b) second order paraelectric to ferroelectric phase transitions. Adapted from mini.physics.sunysb.edu/~mdawber/research.htm.

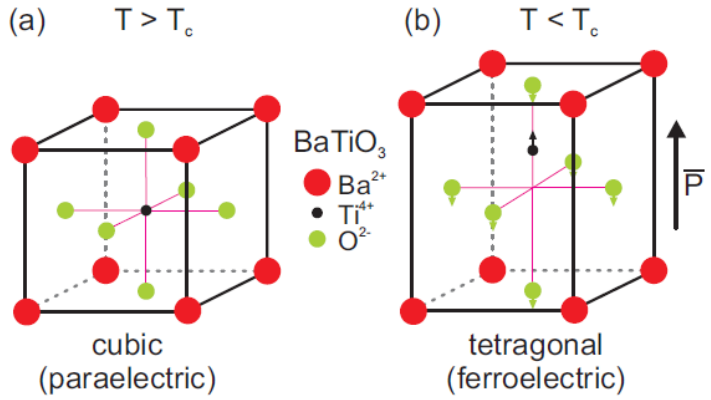

Fig. 1.8: (a) Cubic $BaTiO_3$. The high temperature centrosymmetric unit cell at $T > T_c$ gives rise to a paraelectric phase. (b) Tetragonal $BaTiO_3$. At $T < T_c$ the shifts of the Ti^{4+} and O^{2-} ions generate an electric dipole exhibiting a spontaneous polarization. Adapted from [39].

1.3 Epitaxy

1.3.1 Growth process

Epitaxy is the ordered and directional growth of a film material on a substrate. The word originates from Greek with “epi” and “taxis” meaning “from above” and “in an ordered manner”, respectively. In an epitaxial growth process, the source material is transported to a substrate to interact with (Fig. 1.9). It is suitable to describe the epitaxial process as a series of individual basic steps, which can occur simultaneously for different particles during a real growth process.

The basic deposition steps are:

a) Adsorption of adatoms at the substrate surface
b) Surface diffusion of the absorbed adatoms
c) Desorption of adatoms from the substrate surface
d) Nucleation of islands
e) Film development by coalescence of islands

In general, an adatom can desorb from the surface either while the described steps are in progress or right after completion of any of them. The thermodynamical stability of an adsorbed particle depends strongly on the number of available bonding partners. A single nucleated adatom on a flat surface (one bonding partner) is less stable than one that is located for example at a step edge (two bonding partners). The desorption rate is also significantly affected by the system's temperature as well as the background pressure of the ambient gas. The diffusion length depends on the substrate temperature and the kinetic energy of the adsorbed species. An activation energy (effective diffusion barrier energy) has to be overcome in order to allow diffusion [55]. The higher thermodynamical stability of certain nucleation areas such as steps or kinks also affects diffusion [55]. This means that a particle that is already located at a comparatively stable site with lower free energy is less likely to overcome the effective diffusion barrier.

The surface kinetics are described by the binding energies E_a (between condensing atom and substrate) and E_b (between condensing atoms) as well as the diffusion energy E_d. Typically, the diffusion energy is small compared to the bonding energies so that $E_d << E_a$.

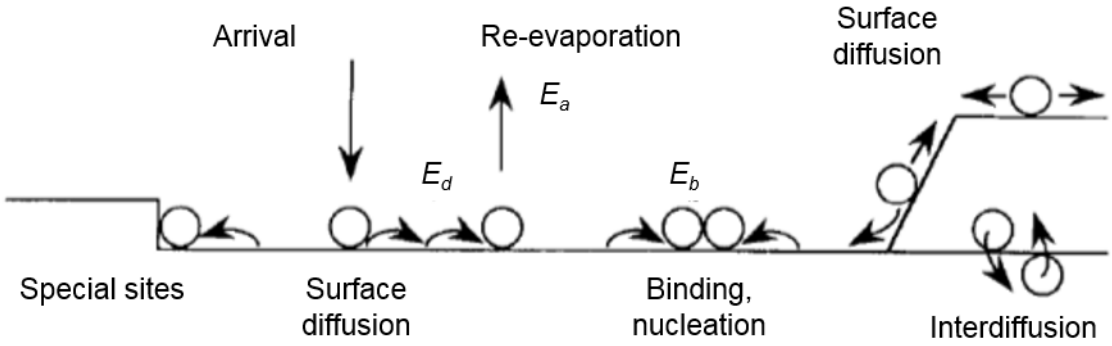

Fig. 1.9: Schematic illustration of processes contribution to epitaxial growth. Adapted from [56].

Adatoms arrive at the substrate with rate R and form local clusters, which become more stable as the lateral cluster size increases. A high value of R leads to a high supersaturation of adatoms on the substrate surface. The nucleation density n_x thus strongly depends on the adatom arrival rate R (cluster size) and the substrate temperature (balance between diffusion and desorption). For a concise review of this topic, I refer to publications by John A. Venables [56, 57].

Homo- and Heteroepitaxy

In the case of homoepitaxial growth, substrate material and adatoms are of the same material. Heteroepitaxial growth describes the deposition of a material different from the substrate. In the latter case, differences in unit cell lattice parameters lead to the incorporation of lattice strain into the developing film, introducing stress energy.

1.3.2 Growth modes

The present section introduces five modes for epitaxial thin film growth. The main ones regarding flat surfaces are the 2-D Frank-van der Merve, the 3-D Volmer-Weber and the transitional 2-D to 3-D Stranski-Krastanow growth modes. The determining factor for these growth modes is the change of the surface free energy of the film-substrate system:

$$\Delta\gamma = \gamma_f + \gamma_i - \gamma_s \quad (1.6).$$

There are three contributions, namely the surface free energy γ_f, the interface energy γ_i and the substrate energy γ_s. Thereby, the interface energy strongly depends on the strain in the film induced by the lattice mismatch between film and substrate.

Frank-van der Merwe

In the case of 2D growth, a new layer starts to adsorb only after the previous layer is completely covered (Fig. 1.10(a)). For this to occur, the sum of the film's free surface and interfacial energy has to be less than the surface free energy of the substrate ($\Delta\gamma < 0$) [58]. In this case, the particle-substrate attraction is higher than the particle-particle attraction, so that adatoms overcoming the diffusion barrier are more likely to nucleate without desorption on the substrate, as compared to binding to an already nucleated adatom. This results in the 2-D growth of a wetting layer. Films that are grown without lattice stress generally continue to grow in the Frank-van der Merve mode. The surface free energy of the film depends on the nucleation rate, so that high supersaturation is unfavorable for 2D growth [56, 57].

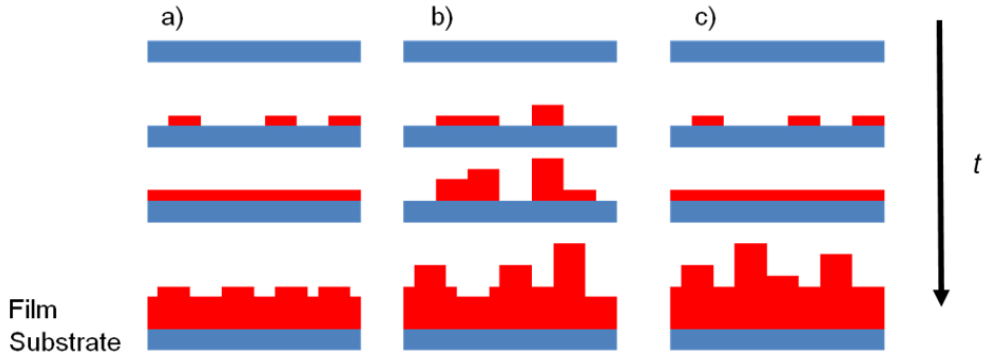

Fig. 1.10: Epitaxial growth modes (a) Frank-van der Merwe (2-D), (b) Volmer-Weber (3-D)) and (c) Stranski-Krastanow (2D to 3D).

Volmer-Weber

Energetically, the situation in 3D-island growth is reversed with regard to 2D growth ($\Delta\gamma > 0$). Accordingly, particle-particle attraction is higher than particle-substrate attraction, so that islands evolve before a film layer is completed. The individual islands grow both in vertical and lateral direction, generally resulting in island coalescence (Fig. 1.10(b)). This leads to the formation of a covered film surface, which is comprised of a certain amount of grains. In some cases, post-process annealing at high temperatures can result in the merging of neighboring islands and thus improve the crystalline quality of the film.

Stranski-Krastanow

In this growth mode, deposition begins with the assembly of 2D layers. Depending e.g. on lattice mismatch and supersaturation, the layer reaches a certain thickness threshold, concomitant with the interface's surface free energy exceeding $\Delta\gamma > 0$. Consequently, there occurs a transition to 3D-island growth, in analogy to Volmer-Weber growth (Fig. 1.10(c)).

On surfaces with morphological steps, additional growth modes can occur:

Step-flow

If the preferential nucleation site of the adatoms is located at the edges of the steps and the diffusion length is of the order of the terrace width, then a unidirectional step-flow can arise. In this case, the original morphology of the substrate stays constant during film growth, only the locations of the edges "flow" in a progressing fashion (Fig. 1.11(a)). The step-flow growth mode generally requires a sufficient diffusion length as compared to the terrace width of the steps. If supersaturation is excessive, the adsorbents are more likely to form relatively stable clusters

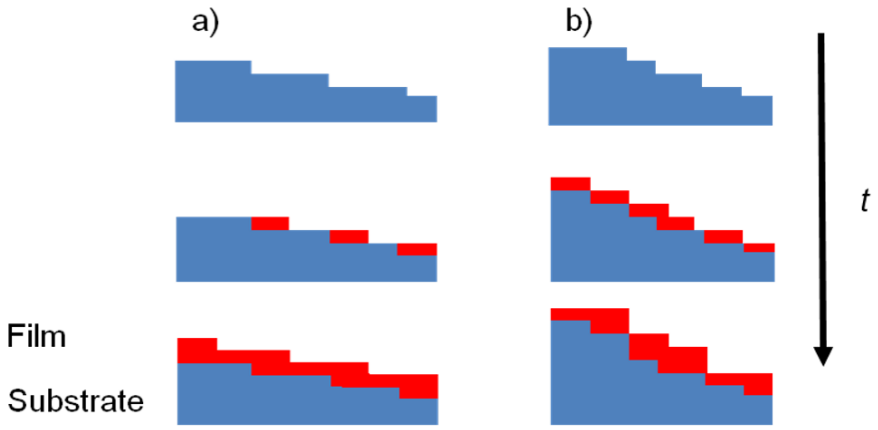

Fig. 1.11: (a) Step-flow and (b) step-bunching growth modes.

before they reach the step-edges, resulting in layer wise 2D or 3D island growth on the steps [56, 57].

Similar to 2-D growth, step-flow growth can transform into 3-D island growth when $\Delta\gamma > 0$ due to lattice stress.

Step-bunching

A high step-density (small terrace width) together with a high growth rate can result in the merging of higher and lower steps (Fig. 1.11(b)). This behavior leads to the evolution of terraces with higher steps heights of two, three or even more monolayers. In order to achieve step-flow growth and avoid step-bunching, it is necessary to choose the terrace width (a result of the angular mismatch during cutting) carefully.

1.3.3 Plastic lattice relaxation

If there is a mismatch between the lattice structure of substrate and film during epitaxial growth, then there arises a non-zero lattice strain. As the film increases in thickness, its strain energy increases as well. Plastic relaxation of the film lattice occurs by incorporating dislocations at the critical thickness h_c, when the energy required for defect formation is less than the strain energy. h_c depends on strain and chemical potential of the deposited films, as well as on the substrate's defect density. One approach to determine the critical thickness h_c of a film under induced stress due to lattice mismatch is the Matthews-Blakeslee model [59]:

$$h_c = \frac{b}{2\pi f}\frac{(1-\nu cos^2\alpha)}{(1+\nu)cos\lambda}\left(ln\frac{h_c}{b}+1\right) \quad (1.7).$$

Here, b is the strength of the dislocations, ν the poisson ratio of the film and f is the lattice mismatch between film and substrate material. The angle α lies between the dislocation line and the burgers vector and λ is the angle between the slip direction and the direction perpendicular to the line of intersection of the slip plane and the interface.

However, this approach is based on the assumption that misfit dislocations present in the substrate bend by slip under the influence of resolved shear stress, which is not well suited for substrates with a very low dislocation density. Here the calculated critical thickness is found to be about one order of magnitude smaller than the experimental one [60].

An alternative formula is given by Matthews et al. [61], assuming the nucleation of dislocations at the surface of the film. The dislocations then extend into the film. This generally results in an increased theoretical critical thickness, roughly by one order of magnitude as compared to the Matthews-Blakeslee model.

Cohen-Solal et al. [62] have proposed a phenomenological model for calculating the critical thickness of strained layers:

$$h_c = A^* f_m^{-3/2} \quad (1.8),$$

with:

$$f_m = \frac{a_f - a_s}{a_s} \quad (1.9).$$

A^* is an adjustable parameter and depends on material properties of the film and the defect density of the substrate. The in-plane lattice parameters of film and substrate are given by a_f and a_s, respectively. If substrates with very low defect densities (such as $DyScO_3$, 10^2-10^5 cm^{-2} [63]) are used, A^* is expected to depend on the film material only. By equation (1.8), h_c is monotonically decreasing in f for positive A^*. An increased lattice mismatch therefore results in a decreased theoretical critical thickness. In the present work, this behavior was also observed for thin films of $NaNbO_3$, see chapter 5 ($NaNbO_3$).

1.4 Biaxial strain

1.4.1 Volume change

The films deposited in the course of this work experience biaxial lattice stress due to the mismatch between the in-plane lattice parameters of film and substrate. In contrast, the films are considered to be free in the out-of-plane direction and thus have the ability to react on the induced biaxial in-plane strain. If the lattice is under compressive (tensile) strain, it will expand (contract) in the free direction. This behavior is called the Poisson effect and is quantified by Poisson's ratio ν.

The general definition of the Poisson's ratio for crystals is [64]:

$$\nu_{ji} = \frac{S'_{ij}}{S'_{jj}} \quad (1.10).$$

Given the material's elastic compliances S_{ij}, it is therefore possible to calculate Poisson's ratio along certain directions. The average Poisson ratio of a stable material attains values between -1 and 0.5. A material with ν = 0.5 (e.g. rubber) is incompressible which means that its unit cell

volume is not affected by lattice strain. On the other hand ν = 0 (e.g. cork) will result in no expansion or contraction of the free direction upon external pressure. Under the assumption of a biaxial isotropic lattice strain, the relative change of the unit cell volume of strained lattice compared to unstrained lattice is given by [65],

$$\frac{\Delta V}{V} = \frac{1-2\nu}{1-\nu} * 2\frac{\Delta a}{a} \quad (1.11),$$

where V is the unit cell volume and $(\Delta a/a)$ is the lattice mismatch. In the case of anisotropic biaxial in-plane strain $\Delta a/a \neq \Delta b/b$. In this case, equation (1.12) provides a valuable approximation:

$$\frac{\Delta V}{V} = \frac{1-2\nu}{1-\nu} * \left(\frac{\Delta a}{a} + \frac{\Delta b}{b}\right) \quad (1.12).$$

The out-of-plane lattice parameter depends on biaxial in-plane strain as follows:

$$\frac{\Delta c}{c} = \frac{-\nu}{1-\nu} * \left(\frac{\Delta a}{a} + \frac{\Delta b}{b}\right) \quad (1.13).$$

For metal oxides ν is typically in the range of 0.25 – 0.4 [66].

1.4.2 Elastic strain energy density

Most of the materials used in this work have an orthorhombic symmetry with anisotropic lattice parameters, which is evident from comparing the pseudocubic lattice parameters (see chapter 3 (Materials)). In the case of $NaNbO_3$ and $KNbO_3$, the anisotropy reaches up to about 0.9 % and 1.6 %, respectively. For comparison, the anisotropy of $DyScO_3$ is only about 0.1 %. It is therefore not immediately obvious, which film orientation results in minimal biaxial stress on each substrate. For computing the stress energy in dependence of film orientation, it is necessary to know the elastic constants of the film material. While there is some data on the parameters of $KNbO_3$ (Table 1.1) [67], no such information is available for $NaNbO_3$ at this time. I will assume that the stiffness parameters (C_{ij}) of both materials are similar.

According to Hook´s law, the elastic strain energy density of a film is calculated by [68]:

$$F(\varepsilon) = \frac{1}{2}\sum_{klmn} C_{klmn}\varepsilon_{kl}\varepsilon_{mn} \quad (1.14).$$

The anisotropic lattice mismatches between film and substrate are given by ε_{kl} with $k,l \in$ [x,y,z]. Orthorhombic lattice parameters are often transformed into the pseudocubic notation. Then the elastic energy reads [68]:

$$F(\varepsilon) = \frac{C_{11}}{2}\left(\varepsilon_{xx}^2 + \varepsilon_{yy}^2 + \varepsilon_{zz}^2\right) + 2C_{44}\left(\varepsilon_{xy}^2 + \varepsilon_{xz}^2 + \varepsilon_{yz}^2\right) + C_{12}\left(\varepsilon_{xx}\varepsilon_{yy} + \varepsilon_{xx}\varepsilon_{zz} + \varepsilon_{yy}\varepsilon_{zz}\right)$$

$$(1.15).$$

with C_{ij} in the Voigt notation ($\sigma_{ij} = C_{ijkl}\,\varepsilon_{kl}$ transforms to $\sigma_i = C_{ij}\,\varepsilon_j$).

Table 1.1: Stiffness parameters C_{ij} of orthorhombic $KNbO_3$ (Voigt notation).

C_{11}	C_{22}	C_{33}	C_{12}	C_{13}	C_{23}	C_{44}	C_{55}	C_{66}
224	273	245	102	182	130	75	28.5	95

For estimating the free energy density, the following assumptions were used:

1) Film and substrate material are regarded as (pseudo)cubic.
2) The film is regarded as an elastic continuum.
3) The surface is free of traction.
4) The film is semi-infinite.
5) The in-plane lattice parameters of the film at the interface are equal to those of the substrate.
6) Shear strain can be neglected.

The lattice mismatch distortions ε_{xx}, ε_{yy} of the remaining non-zero components are known. For materials with a monoclinic distortion angle, like e.g. $NaNbO_3$ and $KNbO_3$, the third assumption is justified only, when this angle is small (< 1°). Under these assumptions elastic strain energy density $F(\varepsilon)$ of a strained film on a lattice mismatched substrate simplifies to:

$$F(\varepsilon) = \frac{1}{2}\left(\varepsilon_{xx}^2 C_{11} + \varepsilon_{yy}^2 C_{22} + 2\varepsilon_{xx}\varepsilon_{yy} C_{12}\right) \qquad (1.16).$$

The orientation of fully strained films is expected to coincide with the orientation that exhibits the lowest strain energy.

Chapter 2: Methods

2.1 Pulsed Laser Deposition – PLD

Pulsed laser deposition (PLD) is a physical vapor deposition technique (PVD) that is widely used in research due to its versatility. In principle, congruent transfer of the target material to a film can be achieved for a wide range of materials. The possibility to easily switch targets during one deposition run allows the fabrication of many different heterostructures and superlattices. However, the substrate size is limited in PLD, so that it is almost exclusively applied in fundamental research.

In the PLD set-up, a pulsed laser beam is focused via an optical system, including lenses, mirrors and apertures, onto a solid target in an evacuated process chamber. The energy of the laser pulses is absorbed at the target surface. This causes a rapid temperature increase at the surface and a Coulomb explosion, resulting in a directed plume consisting of charged particles, free radicals and molecule clusters along the surface normal of the target, regardless of the laser shots´ angle of incidence. The ablated species exhibit kinetic energies between 1 and several hundred eV [69]. Although the substrate is usually heated, it is much cooler than the plasma plume resulting in the condensation of the ablated species at the substrate surface. A brief description of PLD principles is given below. For further information, I refer to books edited by Chrisey and Hubler [70], R. Eason [71] and M. Lorenz and M. S. R. Rao [72].

2.1.1 Plasma Model

For the propagation of the plasma plume, two models (drag force and shock wave) are proposed [73], [74]. The drag force model is considered to accurately explain the plume behavior at low ambient gas pressure (< 0.1 mbar). In this case, the scattering collisions between the ablated species and ambient gas molecules occurs are elastic. The trajectories of the ablated species depend on their respective mass. Heavier particles remain highly forward directed. In contrast, lighter ones are scattered to higher angles and quickly lose their kinetic energy. For collinear collisions one finds the following relation [75]:

$$\frac{\Delta E_{kin1}}{E_{kin1}} = \frac{4mM_A}{(m+M_A)^2} \qquad (2.1).$$

Here, m and M_A are the mass of the ablated particle and of the ambient gas molecule, respectively. E_{kin} is the kinetic energy of the ablated species. Thus, in the range of about 0.01 to ~0.1 mbar background pressure, discriminative thermalization can occur resulting in both thermal (light) and non-thermal (heavy) constituents of the ablated species [76, 77]. This often leads to off-stoichiometry in the films, due to a considerable loss of the lighter species in the plasma plume.

In the case of higher background pressure, D. B. Geohegan [78] has shown that the drag force model is still able to describe the initial expansion. However, at later stages the plume propagation becomes dominated by a shock wave behavior. The formation of such a blast wave may arise only when the mass of the accumulated gas surrounding the particles of the shock wave exceeds the mass of the ablated species [79], [80]. If a sufficient fraction of plume particles collides with gas particles, then they may jointly form a collective shock wave in target normal direction [81]. It is not possible to predict the precise circumstances of the transition from drag force to shock wave like propagation for any given material.

The plasma temperature is in the order of 10^5 K and therefore significantly higher than the temperature of the target surface. After the absorption of the laser pulse and the ejection of the plasma, the target cools down. During this time, volatile elements such as alkali and lead atoms thermally evaporate at significant rates. The energies of these particles are not sufficient for a contribution to the film growth, but can result in locally off-stoichiometric targets [82].

2.1.2 Growth parameters

The epitaxial growth of complex materials like perovskites in 2D-growth mode by means of PLD can be achieved only when the deposition parameters are well adjusted. The influence of the main deposition parameters on film growth will briefly be discussed in the following.

Background gas and pressure

Depending on the ablated material, reducing, inert and oxidizing atmospheres can have a significant impact on the thermodynamic stability of the films. If the background gas atoms or molecules are part of the film composition (e.g. O_2 for oxides or N_2 for nitrides) the pressure also influences the supersaturation. Deposition of oxides at low oxygen background pressures is reported to result in a high density of oxygen vacancies in the films [83].

The kinetic energy of the plasma particles is reduced by collisions with the ambient gas. Thermalized particles in the plasma plume have significantly reduced kinetic energy upon reaching the substrate. Subsequently a reduced number of adatoms is able to overcome the diffusion barrier on the substrate surface [55]. Enhanced surface diffusion can be achieved by increasing the thermal energy of the adatoms with the help of elevated substrate temperatures. On the other hand, very low ambient gas pressure causes the adatom energies at the substrate to exceed the threshold energy for sputtering, typically in the range of 10 to 50 eV [84]. The sputter threshold energy depends on the material. Thus, preferential resputtering at the substrate surface can occur.

In this work, background gas pressures between 10^{-5} and 2 mbar O_2 have been used. The mean free path length of a particle travelling at high velocity through an ambient gas is given by [85]:

$$l = \frac{\mu}{p}\sqrt{\frac{\pi k_B T}{m}} \qquad (2.2).$$

In this equation μ, p and m are the viscosity, pressure and the molecular mass of the ambient gas, respectively. T is the temperature and k_B is the Boltzmann constant. With a viscosity of $1.91*10^{-7}$ mbar*s [86] and a molecular mass of $4.98*10^{-26}$ kg for gaseous O_2, the mean free path length has been estimated for various gas pressures and is presented in Table 2.1.

Table 2.1: Estimated mean free path length of particles and number of average collisions after 50 mm in O_2 ambient gas at various background pressures.

p (mbar)	*l* (mm)	*avg. collisions after 50 mm*
2	< 0.1	1080
0.7	0.1	390
0.05	2	28
10^{-2}	10	5
10^{-3}	~10^2	1
10^{-5}	~10^4	0

Typical target to substrate distances range from 30 mm to 100 mm. Maintaining background pressure as low as 10^{-5} mbar has therefore a significant effect on the number of experienced collisions as the ablated species move to the substrate. A complete thermalization of the particles is expected for the case of 0.7 mbar and higher pressures. In the range between 0.05 mbar and 0.01 mbar the mean free path length significantly increases. This will affect the spread of particles of different mass. A discriminative thermalization as described above is expected, if light plasma particles such as O or Na are present. At ambient pressures of approximately 10^{-2} mbar and below, no thermalization due to collisions is expected. Resputtering due to the high kinetic energy of the ablated species is reported to have negative effects on film growth [87].

a) Substrate temperature

A higher substrate temperature results in higher diffusion lengths on the substrate and allows the growth of well-ordered films. However, the desorption rate of the adatoms also increases, thereby the growth rate decreases. Calculations by the program Factsage showed that volatile materials exhibit reduced thermodynamic stability at high temperatures, with a dependence on the background pressure. Due to their high vapor pressure, materials like potassium exhibit a

significantly higher desorption rate at a temperature of 900 °C in pure oxygen background pressures of 2 mbar as compared to niobium and sodium. In this way, the substrate temperature affects the composition of the deposited film.

b) Laser fluence

The laser fluence directly determines the kinetic energy and the amount of ablated species in the plasma plume. It has been reported that the laser fluence of the ablation spot can influence the composition of the films as was shown for the Sr/Ti ratio in $SrTiO_3$ films [88], where increased fluence resulted in a decreased Sr/Ti ratio in the films due to preferential ablation of Sr (Ti) at low (high) laser fluence [89].

c) Pulse repetition rate

An increased pulse frequency results in an increased growth rate per time. The non-continuous nature of PLD allows short steps of post-annealing after each pulse. A high pulse frequency reduces the time for diffusion and desorption to occur before the next pulse is shot. In addition, the target spot hit by a previous laser will not have sufficiently solidified if the repetition rate is too high leading to the expulsion of droplets (see below). This behavior is more significant for small targets.

d) Target to substrate distance

With increasing distance between target and substrate, the average number of collisions of plasma particles with the background gas molecules increases. This results in reduced kinetic energy and a larger inhomogeneity between heavy and light constituents at the substrate. In addition, due to the spread of the plasma plume, the supersaturation of the adatoms is reduced with increased distance, resulting in a reduced growth rate. The supersaturation also affects the growth mode (see chapter 1.3.2).

2.1.3 Limitations

The lateral homogenous growth of thin films by a standard PLD set-up on substrates with a size of 1 cm² is well established. The deposition on significantly larger substrates remains a challenge due to the directional plasma plume. In the set-up of Vanketesan et al., laterally homogeneous growth of $YBa_2Cu_3O_{7-x}$ could only be achieved around the highly forward directed area, with small deviation angles $\theta < 20°$ [90]. Although this limitation can be compensated by the use of several laser beams and targets at once [91] or by rotating the substrate [92], the PLD technique is almost exclusively applied in research.

A common problem in PLD is the expulsion of microparticles and droplets from the target. Microparticles are formed, if the energy of the laser pulses is not absorbed directly at the

surface. In this case, target material evaporates inside the target, at sites located a few µm beneath the mostly solid surface. The resulting pressure can be powerful enough to expulse µm-sized solid pieces. If they reach the substrate, epitaxial film growth is negatively affected with regard to surface roughness and crystal quality [93]. It is therefore very important that the laser wavelength and fluence is suitable for the applied targets. Commonly, UV KrF- or XeCl-excimer laser are used operating above the plasma frequency of the targets. Depending on the precise material, other types of lasers are also in use.

Droplets are clusters of liquid target material, which are sucked away from a molten target surface. They are generated by sudden fluctuations in the size of the plasma plume, resulting in a sudden pressure drop. This behavior is caused by fluctuations of the laser fluence between individual laser pulses and/or the deposition from unevenly ablated or molten target surfaces. Therefore, it is important to keep the laser fluence constant between the individual shots. Moreover, the target should be homogenous and rotate and toggle during deposition. Target motion not only ensures that the ablation is uniform, but also that the laser impact site is given enough time to cool down and properly solidify before being hit again.

2.1.4 PLD system used in this work

The PLD system used in this work is equipped with a KrF excimer laser operating at a wavelength of 248 nm. A target revolver that fits four targets allows the deposition of heterostructures and superlattices and enables rotation and toggling of the targets during deposition. The use of a fluence control system allows to start deposition runs with controlled laser fluence. Typically, a fluence of 2.2 J/cm² was used. The combination of target rotation and toggling as well as constant laser fluence proved effective in minimizing droplet and microparticle formation and enabled film growth with reproducible deposition rates. Furthermore, the laser window is shielded from the directional plasma plume. This way almost negligible deposition occurs on the laser window resulting in a constant fluence throughout one deposition run. This allows achieving both reproducible growth rates and reduces the generation of droplets. The substrate can be heated up to 1000 °C both in high vacuum and in oxygen atmosphere. The target to substrate distance can be adjusted in the range between 45 mm and 90 mm. It is possible to manually rotate and slightly tilt the substrate holder, which allows precise alignment for the in-situ RHEED system. In contrast, no automated rotation of the substrate is possible during deposition. However, since the substrates were placed in the center of the plume and only substrates with a maximum size of 1 cm² were used, no problems with lateral film homogeneity have been observed. A schematic overview of the applied PLD-setup is given in Fig. 2.1. The optical lenses maintain a well-defined laser spot allowing for the control of the laser fluence. Characteristic images of the plasma plumes of NaNbO3

depositions at 0.05 mbar oxygen (a) dominated by drag force and 2 mbar oxygen (b) dominated by shock wave propagation background pressure are presented in Fig. 2.2.

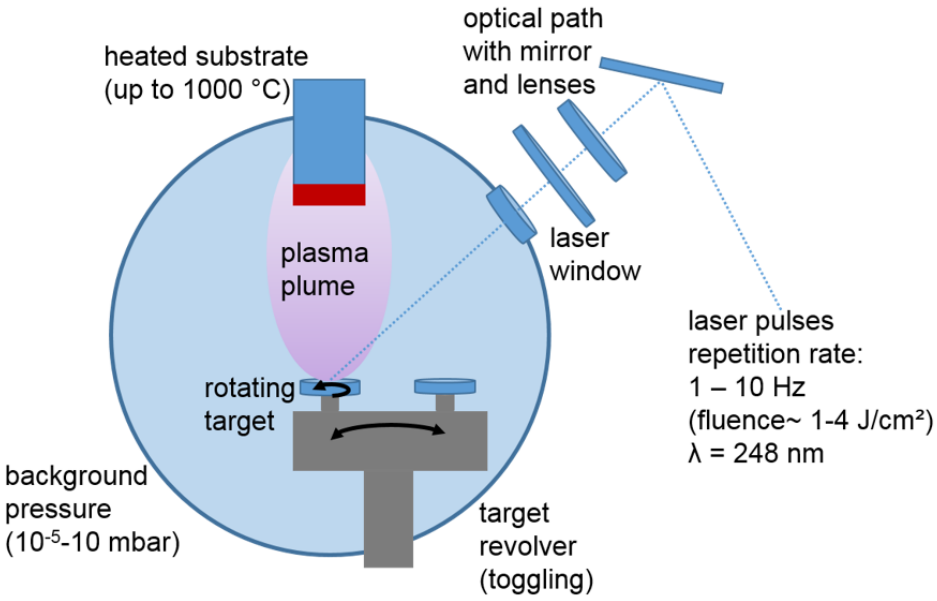

Fig. 2.1: Schematic overview of the PLD-setup used in this work.

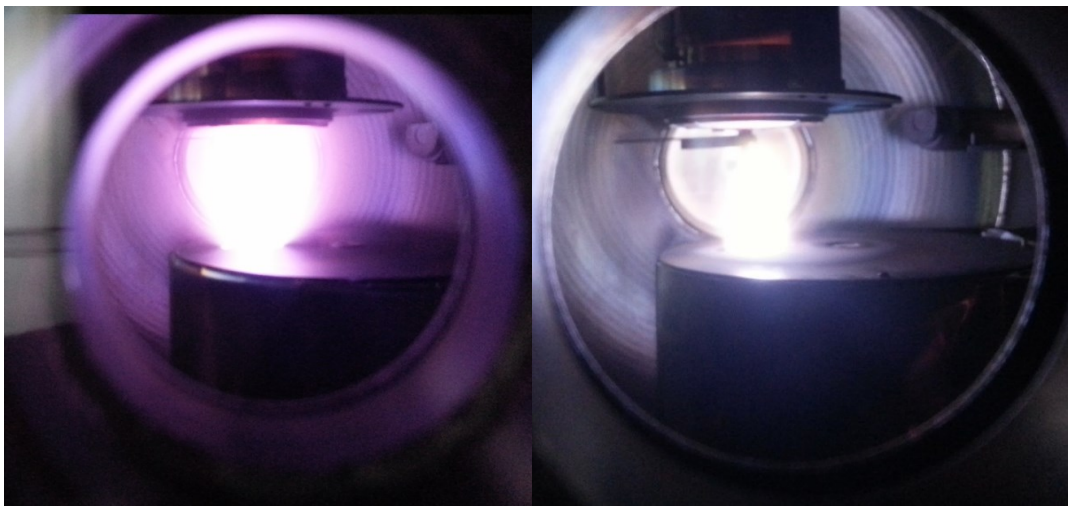

Fig. 2.2: Plasma plume of $NaNbO_3$ depositions at (a) 0.05 mbar and (b) 2 mbar oxygen background pressure.

2.2 Reflection high energy electron diffraction

The structural development of surfaces can be monitored by reflection high energy electron diffraction (RHEED). Electrons with energies between 5 and 100 keV are directed towards the film surface under grazing incidence (~1° to 3°). The diffracted beam is visualized on a fluorescence screen. Due to the grazing incidence of the beam, the electrons only interact with atoms close to the surface. For a more detailed description of RHEED principles I refer to the chapter by I. Boscovic *et al.* in the book "In Situ Process Diagnostics and Intelligent Materials Processing" [94].

2.2.1 RHEED Patterns

Figure 2.3(a) depicts a typical diffraction pattern of a smooth surface of $NaNbO_3$. The occurrence of diffraction rods can be explained by means of kinematic theory, while the Kikuchi lines are addressed by dynamic theory. The periodic 3D-lattice points in real space are converted via a Fourier transformation into periodic net planes in reciprocal space. The Laue conditions for constructive interference $\underline{G} = \underline{k} - \underline{k}'$ must be fulfilled for the elastically scattered electron beam. $\underline{G}$ is the reciprocal lattice vector; $\underline{k}$ and $\underline{k}'$ are the wave vectors of the incidence and the diffracted beam, respectively. A well-established way to visualize and explain the pattern obtained from the Laue conditions is the Ewald Sphere (Fig. 2.4). Since the wavelength of the electrons is short (0.0068 nm at 30 keV), the radius of the Ewald Sphere is very large compared to typical reciprocal lattice vectors ($|k| \sim 900\ nm^{-1}$, $|G| \sim 15\ nm^{-1}$). Due to the low penetration depth, the lattice periodicity appears in the surface plane with an almost infinite periodic distance vertical to the surface. Thus, the reciprocal lattice points of the vertical direction are located infinitely close to each other and the reciprocal lattice points of a 3D lattice degenerate into rods. The diffraction reflexes occur at the intersections of the reciprocal rods with the Ewald sphere. A perfect 2D lattice should therefore show very sharp diffraction spots. In real 2D lattices, however, reduced in-plane symmetry (e.g. by surface steps visible in an Atomic Force Microscopy (AFM) image (Fig. 2.3(b))) results in a broadening of the reciprocal lattice lines [94]. Furthermore, the radius of the Ewald sphere is finite, due to the dispersion in electron wavelength. Hence, the intersection with the Ewald sphere is blurred and a rod-like diffraction pattern perpendicular to the crystal surface develops (Fig. 2.3(a)). The vertical diffraction stripes exhibit a prominent lateral blur. It is possible to calculate the lattice parameter parallel to the surface if the distance *d* between fluorescence screen and substrate and the distance t between the diffraction rods are known. However, in general this approach is rather inaccurate. X-ray diffraction reciprocal space maps in vicinity of various asymmetric Bragg reflections of the substrates allow the determination of the in plane lattice parameters of the films more precisely (see chapter 2.5 (XRD)).

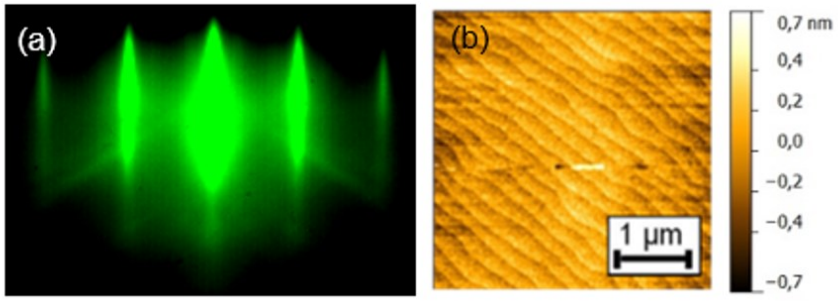

Fig. 2.3: (a) Typical RHEED diffraction pattern of a $NaNbO_3$ film exhibiting a step-and-terrace surface morphology. The vertical (diagonal) stripes are diffraction rods (Kikuchi lines). (b) AFM image of the sample observed in (a).

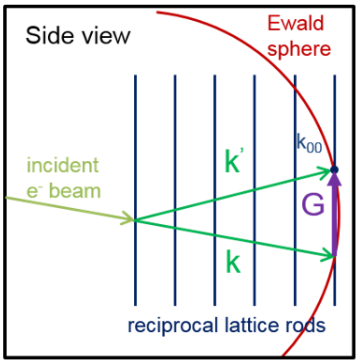

Fig. 2.4: Schematic side view of the Ewald sphere its intersection with and the reciprocal lattice. k_{00} marks the specular spot.

Multiple scattering processes and the strong interaction between electrons and the crystals´ atoms play an important role in RHEED investigations. These effects are considered in dynamic scattering theory. Prominent examples for multiple scattering processes are the Kikuchi-lines and –bands, visible in Fig. 2.3. Since their position is determined by the crystal orientation, they can be used to precisely align the crystal. The occurrence of Kikuchi-lines is often more prominent on periodically stepped surfaces.

2.2.2 In-situ determination of the growth mode

As scattering of the electron beam from the surface is diffuse, the intensity of the diffracted beam is strongly determined by the surface topography. The development of the intensity during deposition contains information about the growth mode:

(a) Constant intensity: During step-flow growth, the step density of the substrate surface is constant and no intensity variation is expected [95].

(b) RHEED oscillations: In the case of 2D-layer-by-layer growth the initially smooth film surface is covered by several islands of the height of one monocell. Subsequently, the layer closes to become smooth again, just before new islands assemble again, and so forth (see Fig. 2.5) [96]. Diffuse scattering on the edges of more and more islands decreases the intensity of the diffracted beam. The minimum intensity is expected for semi-completed layers. When more than half of the layer is covered, then the beam intensity recovers, reaching its maximum for completed layers. The resulting intensity oscillations can be used for in-situ control of film thickness and allow to stop film growth at a defined surface coverage. Usually one would stop with a smooth completed layer, but other scenarios are possible as well.

(c) Decreasing intensity: If the film surface roughens continuously during the growth process, as it is the case in 3D-island growth, the intensity of the diffracted electron beam is expected to decrease without the occurrence of oscillations. A rough surface formed by 3D crystallites also generates a spotted diffraction pattern, due to bulk like diffraction. As the pathlength of the incident electrons is high and they can pass through surface features. A typical example for this behavior can be seen in Fig. 2.6, where the diffraction pattern of a $NaNbO_3$ with a 3D-island surface morphology is shown.

For intensity measurements of the zero order reflection ($k' = 0$) it is advisable to align the incident electron beam and the crystal surface in such a way that the Kikuchi lines do not intersect with the specular spot. In this way, fluctuations of the Kikuchi line intensity (e.g. due to a change in position of step edges) have no impact on the development of the zero order diffraction intensity during film growth.

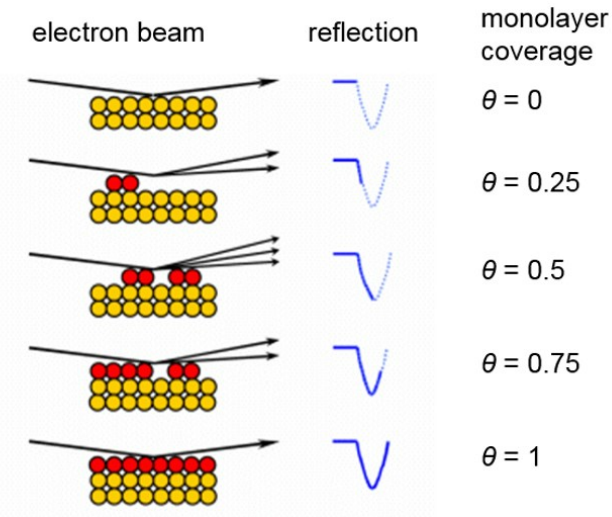

Fig. 2.5: Schematic illustration of RHEED intensity oscillations during 2D-layer-by-layer growth. Adapted from [97].

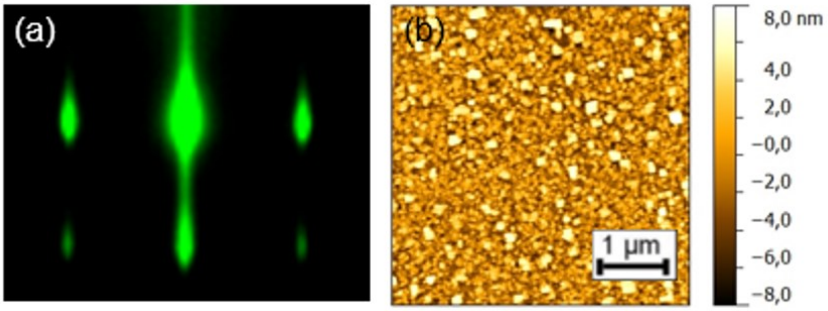

Fig. 2.6: (a) Typical RHEED diffraction pattern of a $NaNbO_3$ film exhibiting a 3D-island surface morphology. (b) AFM image of the sample observed in (a).

2.2.3 RHEED system used in this work

The RHEED system used in this work is a KSA 400 (K-Space Associates). The electron emitter energy has been set to 30 keV. High gas pressures significantly reduce both mean free path length and kinetic energy of the electrons. Moreover, they reduce the service interval of the electron emitter. In order to employ RHEED at relatively high pressures of about 0.1 mbar, differential pumps have been maintaining a lower pressure at the filament. In this way, the maintenance interval of the tungsten filament is greatly increased and the acceleration path is protected against spontaneous discharges at high voltage. In the PLD set up used employed in the present work, the maximum background pressure compatible with the RHEED system is 0.3 mbar.

2.3 Atomic Force Microscopy

Invented by Binning, Quate and Gerber in 1986, the atomic force microscope (AFM) moves a sharp probe tip in a raster-like scan over the sample surface [98]. The tip is located at the end of a rectangular cantilever with length and width of about 100-500 µm and 10-40 µm, respectively. The stiffness or spring constant k of the cantilever is typically in the range between 0.01-40 Nm^{-1}. Typically, the tip height is a few µm and the radius of curvature at the apex in the range between 10 and 20 nm. The tip is usually made from silicon or silicon nitride and can be coated with materials exhibiting conductive or magnetic properties, depending on its application.

Figure 2.7 schematically depicts the principle of AFM. Either the tip is fixed during measurement while the sample is placed on a moveable stage or vice versa. Piezo stack actuators control the displacement in XY-direction so that the sample can be scanned in a raster-like fashion. If the tip is brought into contact with a sample (range of repulsive forces shown in Fig. 2.8), the probe traces the surface topography via deflection and/or torsion of the cantilever. In this way, one obtains a three-dimensional map of the surface. In the contact

mode, a hard tip can damage a soft surface whereas a soft tip can be damaged by scanning a rough surface.

In order to avoid these problems I have exclusively used the intermittent contact or tapping mode. Here, the cantilever oscillates close to its resonance frequency. Upon approaching the surface, the free oscillation amplitude (some 100-200 nm) decreases significantly due to attractive interactions between cantilever and surface related to Van-der-Waals forces. During the measurement, a feedback loop maintains a constant oscillation amplitude by adjusting the height via the Z-piezo. Laser light reflections from the cantilever are detected by means of a four-quadrant photodiode. In this way, not only height adjustments of the Z-piezo but also cantilever deflection and torsion changes can be measured.

In the intermittent contact or tapping mode, the attractive long-range van-der-Waals forces dominate compared to short-range forces caused by an overlap of orbitals (see Fig. 2.8). All measurements were conducted in air. In this case, a thin water layer covering sample surface and probe gives rise to additional capillary forces.

The AFM measurements have been performed on a MFP-3D stand-alone atomic force microscope (Asylum Research) and a Dimension Icon device (Bruker nanosurface division). Typical spring constants of the cantilevers were about 2 N/m.

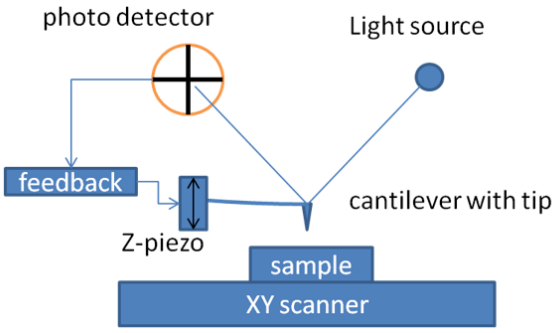

Fig. 2.7: Schematic principle of AFM

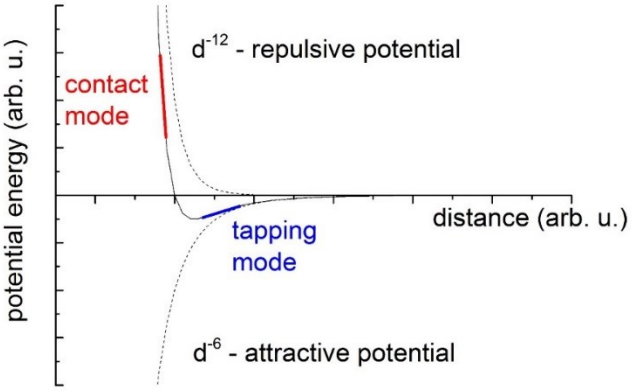

Fig. 2.8: Potential energies in dependence of the distance between tip and surface.

2.4 Piezoresponse Force Microscopy

For Piezoresponse Force Microscopy (PFM), a conductive tip is mounted on an AFM device in contact mode. An electric AC voltage is applied to the tip and interacts with the sample via the inverse piezoelectric effect. The resulting sample oscillations are measured via the subsequent movement of the cantilever [99].

PFM signal response is determined by the local deformation of the sample right under the tip, which is influenced by magnitude and direction of the samples´ polarization relative to the applied electric field. As depicted in Fig. 2.9, the signal is detected by a quadrupole photodetector sensitive to both the vertical displacements (up and down) and the torsions of the cantilever (left and right). Thereby, the electric field is generally applied along the vertical (z) direction.

In vertical PFM (V-PFM, Fig. 2.9(a)), the polarization of the sample in z-direction is detected. The oscillation of the electric field results in a parallel sample oscillation ±Δz. This behavior is called longitudinal response and corresponds to the d_{zz} piezoelectric coefficient. It is possible to measure amplitude and phase of the induced response at the same time. If sample response and electric field are totally in-phase (0°) (Fig. 2.10(a)), then a positive polarity at the tip gives rise to an elongation of the sample. In contrast, if the phase shift between polarization and input signal is 180°, then the sample contracts (Fig. 2.10(b)). Accordingly, ferroelectric domains with varying polarization directions can be distinguished by detecting the phase shift between applied voltage and PFM.

Expansion (contraction) of the sample in vertical direction is accompanied by a simultaneous perpendicular contraction (expansion), which is referred to the transverse response (d_{31}) (see Fig. 2.9(a)). This behavior is more difficult to measure via PFM, especially for films with thickness in the order of 10 nm [38].

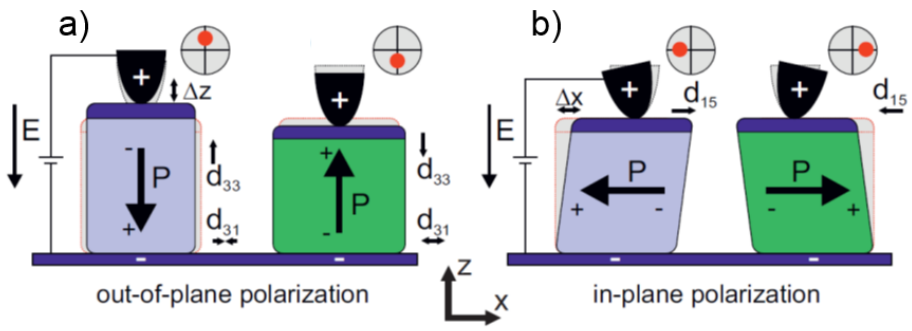

Fig. 2.9: Basic principle of (a) vertical and (b) lateral PFM measurements. Adapted from [100].

Lateral (x,y) sample polarization is perpendicular to the applied electric field. Accordingly, the sample oscillates in *x*- or *y*-direction. This is a shear movement *Δx*, *Δy* of the sample and leads to cantilever torsion as measured by the photo detector. This lateral signal (LPFM) is related to the shear coefficient d_{15}. It is important to note that non-zero in- and out-of-plane polarizations contribute to both the vertical and the lateral signal of the sample.

The PFM measurements presented in this work have been performed in contact mode on an MFP-3D standalone AFM (Asylum Research). Dual AC Resonance Tracking (DART) mode has been employed to track the cantilever resonance frequency, which depends on the precise electrical and mechanical boundary conditions for any given sample-cantilever interaction. These conditions are generally different for different measurement spots. In this way, a significantly improved signal to noise ratio (quality factor improved by a factor of 20-100) is achieved. For a more thorough description of the principles of PFM in general and DART in particular, I refer to the Thesis of A. Duk (pp. 33-42) [38] and the website of Asylum Research (http://www.asylumresearch.de/Applications/PFMAppNote/PFMAppNote.shtml).

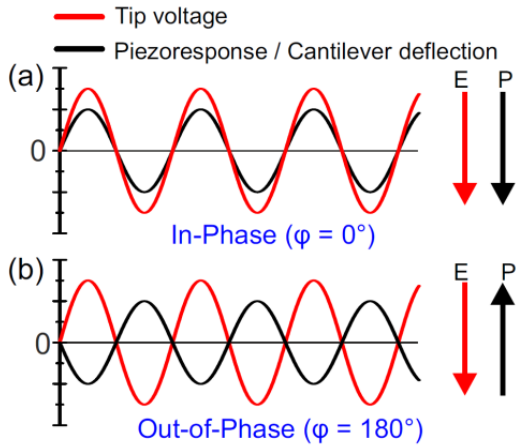

Fig. 2.10: (a) In-phase (φ = 0°) and (b) 180° out-of-phase relation of the driving voltage to the piezoresponse. Adapted from [100].

The PFM investigations were performed by Andreas Duk and Dorothee Braun.

2.5 X-Ray Diffraction

X-Ray diffraction (XRD) allows a detailed analysis of the crystal structure of powders, substrates and films. In this work it was used to determine the crystallographic phases of PLD-Targets (Powder XRD), the out-of-plane lattice parameters and thickness of films (*θ-2θ* scans), the in-plane lattice parameters and strain state (Reciprocal space maps), and the monoclinic distortion angle together with the transversal domain size of the films (Grazing incidence XRD).

2.5.1 Principle

A crystal structure is regarded as an infinite 3D periodic repetition of atoms, forming parallel net planes. The incident X-rays are reflected at these planes and interfere constructively if the Bragg equation is fulfilled [101]:

$$n * \lambda = 2d * \sin\theta_B \qquad (2.3)$$

Here, λ is the wavelength of the X-rays, n is the diffraction order (typically n =1), θ_B is the incident angle with respect to the net planes and d is their spacing (see Fig. 2.11).

2.5.2 High resolution *θ-2θ* scans

With the help of the Bragg equation, it is then possible to determine the out-of-plane lattice parameter d_f of a film via high resolution-XRD (HR-XRD). To this end, a *θ-2θ* scan is performed and the film peak position θ_f is compared with the one of the substrate (θ_f). If the lattice parameter d_s of the substrate is known, we have [102]:

$$\frac{\Delta d}{d} = \frac{d_f - d_s}{d_s} = -\frac{\Delta\theta}{\tan\theta_s} = -\frac{\theta_f - \theta_s}{\tan\theta_s} \qquad (2.4)$$

Destructive and constructive interference of X-rays reflected at film surface and film–substrate interface result in symmetrical thickness oscillations, appearing in the observed interference pattern. Thus, it is possible to infer the film thickness t from the angular spacing $\Delta\theta_o$ of the minima between the thickness fringes [102].

$$t = \frac{\lambda \sin\theta_f}{\Delta\theta_o \sin 2\theta_f} \qquad (2.5)$$

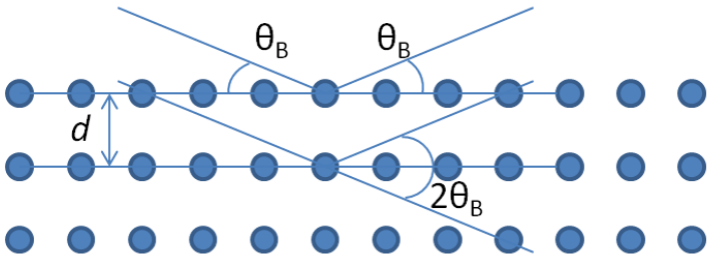

Fig. 2.11: Basic principle of Bragg reflection

Thickness oscillations occur only for well-ordered films with smooth surfaces and interfaces. *θ-2θ* scans are also suitable to analyze superlattice structures. The angular position of the 0-order peak of the superlattice is used to determine the average out-of-plane lattice parameter of the whole stack. From the angular spacing $\Delta\theta_{sat}$ between satellites of different order, the period Λ of the superlattice in real space can be determined [102].

$$\Lambda = \frac{\lambda}{\Delta\theta_{\mathrm{sat}} \cos\theta_{\mathrm{f}}} \quad (2.6)$$

Similar to single films, the overall thickness of the superlattice can be determined by the angular spacing of the minima $\Delta\theta_o$ of the thickness fringes.

For the high resolution X-ray diffraction (HRXRD) measurements presented in this work, a 2-bounce Ge 220 channel-cut crystal has been combined with a parabolic Göbel mirror, in order to select the Cu $K\alpha_1$ line (λ = 1.54056 Å) and to collimate the incident beam to about 11 arcsec.

2.5.3 Powder XRD

For powder XRD measurements, the sample is ground into powder form. In this way, every crystal phase present in the material occurs at various random orientations. In particular, representative proportions of each lattice feature are expected to suitably align with the surface normal of the sample. By identifying respective peaks occuring in the scan, it is then possible to determine which phases are present in the sample. The powder XRD measurements presented in this work have been performed under the Bragg-Brentano geometry using Cu Kα (λ = 1.541 Å) radiation. In order to investigate off-stoichiometry and compositional changes in alkali niobate targets, standardized quartz powder [103] (SiO_2) has been added to some of the samples.

2.5.4 Reciprocal space maps

In order to obtain reciprocal space maps of a Bragg reflection peak, the incident beam is directed to the sample surface under an inclination angle *ω*. At the same time, detector and incident beam enclose an angle of *2θ*. Therefore, the angle between the diffracted beam and the sample surface is *2θ-ω*. The components of the scattering vector parallel $q_\parallel$ and normal $q_\perp$ to the sample surface are given by [104]:

$$q_\parallel = \frac{2\pi}{\lambda}[\cos(2\theta - \omega) - \cos(\omega)] \quad (2.7)$$

$$q_\perp = \frac{2\pi}{\lambda}[\sin(2\theta - \omega) + \sin(\omega)] \quad (2.8)$$

Rotating the sample with the detector at rest is called ω-scan. Thereby, the scattering vector rotates while its length remains constant (Fig. 2.12). If sample and detector are simultaneously rotated with an angle-ratio of 1:2 (ω-2θ-scan), only the length of the scattering vector is affected. The combination of both methods allows scanning the reciprocal space in two

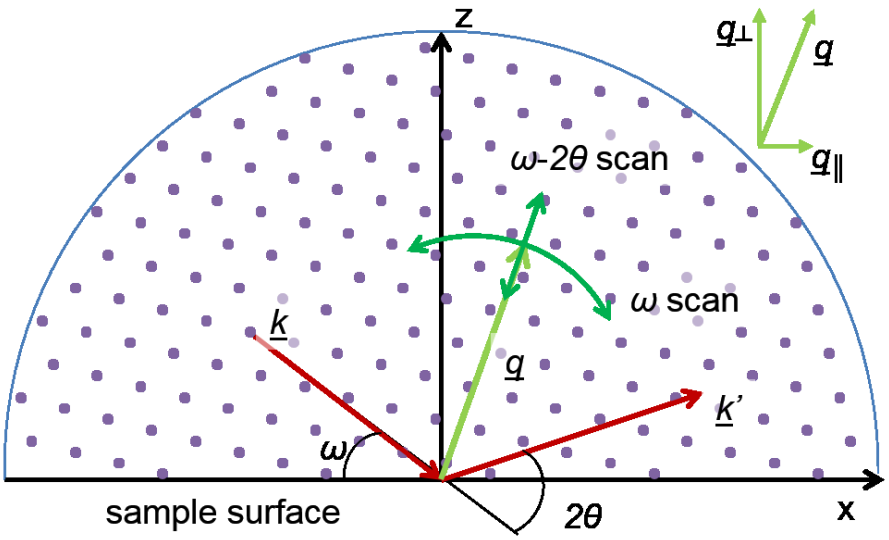

Fig. 2.12: 2D Ewald sphere projected on the x-z plane, HR-XRD scattering geometry with angles ω and 2θ and scattering vector q during angular ω scan and radial ω-2θ scan. Adapted from [105].

orthogonal directions. In this way, one obtains a two dimensional map of the reciprocal space. Scanning the substrate in vicinity of its asymmetric Bragg reflections, both in- and out-of-plane lattice parameters of the film relative to the substrate can be determined.

The direction of the diffracted beam has been measured by means of a linear position sensitive detector [106]. This allows fast data acquisition on the employed Bruker Discovery D8 system.

2.5.5 Grazing incidence

Grazing incidence X-ray diffraction (GIXD) operates close to the angle of total external reflection in order to maximize the signal from the film and suppress the substrate signal. The scattering geometry is shown in Fig. 2.13. Grazing incidence and diffracted beam angles are measured with respect to the sample surface are labeled α_i and α_f, respectively. Accordingly, θ_i and θ_f are the in-plane incident and diffracted angles (Fig. 2.13), whereby the scattering plane is almost perpendicular to the surface. Diffraction originates from planes that are nearly perpendicular to the sample surface. This technique is very sensitive to the in-plane lattice parameters. The surface selectivity of GIXD depends on how close the incidence angle approaches the angle of total external diffraction. In contrast, higher angles of grazing incidence result in higher penetration depths. This way, more information from deeper net planes, which can already be part of the substrate, are obtained. In order to achieve sufficient signal intensities (signal-to-noise ratio), it is often necessary to use radiation sources with high brilliance, such as synchrotrons.

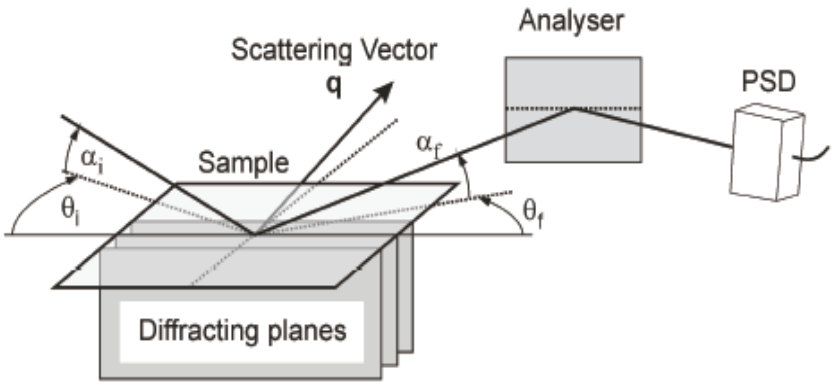

Fig. 2.13: Schematic illustration of a GIXD measurement setup. Adapted from [105].

The GIXD experiments presented in this work have been performed at the KMC-2 beam line at the BESSY synchrotron facility, using an X-ray energy of 8 keV. A two-dimensional position sensitive detector was used to measure the intensity distribution scattered from the sample [106].

Most of all X-ray diffraction measurements have been performed by Albert Kwasniewski and Martin Schmidbauer. The GIXD measurements at BESSY were assisted by Jutta Schwarzkopf, D. Többens and I. Zizak.

2.6 Inductively coupled plasma optical emission spectroscopy

Inductively coupled plasma optical emission spectroscopy (ICP OES) has been used to measure the composition of the ceramic targets with regard to Na, K and Nb. In this method, argon gas is ionized in an intense electric field. An aerosol of the sample dissolved in e.g. HNO_3-HF-H_2O_2 is transported into the plasma where evaporation and ionization take place (Fig. 2.14). Characteristic photon emission (λ in the range of 190 to 380 nm, http://www.geologie.uni-frankfurt.de/Staff/Homepages/Bahr/Kurzskript%20ICPOES.pdf) is caused by the excitation during breaking up and recombining of molecules and atoms. A spectroscopic analysis of the light emitted by the aerosol is performed by the use of a diffraction grating. The intensity of the wavelengths, which are characteristic for a material, provides information about its concentration. The chemicals used to create the aerosol from original samples contain nitrogen, oxygen and hydrogen; it is therefore not possible to determine the concentration of those atoms in the sample.

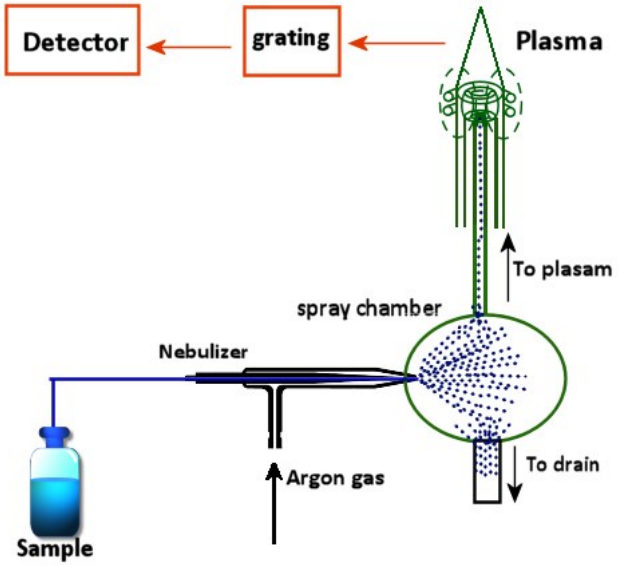

Fig. 2.14: Basic principle of ICP-OES. Taken from http://www.chemiasoft.com/chemd/node/52.

ICP-OES measurements presented in this work have been performed by Rainer Bertram with an IRIS Intrepid HR-DUO system by Thermo Fisher (USA) with about 0.5 % accuracy of the determined mass ratio of the constituents. The samples were prepared by microwave digestion with a HNO_3-HF-H_2O_2 mixture for 20 min at 240 °C.

2.7 Energy Dispersive X-Ray Spectroscopy

Energy Dispersive X-Ray Spectroscopy (EDX) measures the spectrum of X-rays emitted by a sample in order to probe the chemical composition on a local scale (0.1-1 µm). A focused electron beam is absorbed by the sample atoms, leading to the expulsion of shell electrons. Electrons with higher energy (usually occupying K, L or M levels) almost instantly recombine with the created electron hole, resulting in photon emissions. These emissions are characteristic for each element of the periodic table, which directly allows for a qualitative chemical analysis, provided that the characteristic lines of the elements in the sample do not coincide.

A quantitative analysis of the measured line intensities, however, is more difficult. First, it is necessary to calibrate the intensities measured by EDX with a sample of known composition and thickness. Second, the analysis of O/Na or O/Nb ratios for films on oxide substrates is not possible, because the oxygen contributions from substrate and film overlap. The films investigated in this work exhibit variations both in thickness and oxygen content. Therefore, it will only be shown how the growth parameters affect the ratios of Na/Nb.

The film stoichiometry was examined by a NOVA600 (FEI company) scanning electron microscope (SEM), allowing for energy-dispersive X-ray spectroscopy (EDX) with an EDAX (Lambdaspec) system. At 10 keV excitation energy, the Na line at 1.041 keV (Kα) and the Nb lines at 2.166 (Lα), 2.227 (Lβ) and 2.462 keV (Lγ) have been analyzed. Only the $NaNbO_3$ thin films on $TbScO_3$ and $SrTiO_3$ substrates have been investigated by EDX, as the Na and Nb lines do not overlap with other substrate contributions (Tb: 1.240 keV (Mα) , Sc: 4.090 keV (Lα), Sr: 1.806 keV (Lα) and Ti 4.509 keV (Kα)).

2.8 Transmission electron microscopy

High-resolution transmission electron microscopy (HRTEM) allows the structural investigation of a material on the atomic scale. The electron beam used in this method is commonly described by a planar wave. As it travels through the sample, its phase changes due to the interaction with the electric potential of the sample material. If the sample is sufficiently thin, the amplitude remains constant. Comparing the phases of incoming and outgoing wave allows deducing the electric potential distribution and to identify the position of atoms in the sample. The electron beam is focused by electron lenses before entering and after leaving the sample. These lenses are not ideal, however, and the phase change due to the two lenses does not match exactly. One of the most relevant resulting problems is spherical aberration. In order to optimize the resolution of TEM imaging, an aberration corrected FEI Titan 80-300 microscope has been used.

The atomic number distribution in the sample can be measured by high angle annular dark field high-resolution scanning transmission electron microscopy (HAADF-HRSTEM). Thereby one focuses the electron beam onto a single sample point, and captures the transmitted beam with a circular detector. In this way, only scattered electrons are visible (dark field imaging). If the sample thickness is constant, one can determine the local atomic mass from the detected intensity. However, the method is problematic for lighter elements like Na and O.

The sample preparation and TEM investigations have been done by Toni Markurt, Thilo Remmele, Sonia Ganapragasam and Philipp Müller.

Chapter 3: Materials

3.1 Substrates

3.1.1 $SrTiO_3$

Among the materials used in this work, only $SrTiO_3$ exhibits a cubic crystal structure (space group Pm3m) at room temperature (RT). The RT lattice parameter is 3.905 Å, with a thermal expansion coefficient of $3.23(2)*10^{-5}\ K^{-1}$ [107]. Both SrO and TiO_2 layers are neutral, as the electrical charge of the Sr^{2+} and Ti^{4+} cations is balanced by adjacent O^{2-} anions.

In order to obtain TiO_2 single terminated substrates, $SrTiO_3$ has undergone chemical as well as thermal treatment based on an approach by Koster et al. [108]. For this, the substrates were hydrolyzed in de-ionized water for 10 minutes, resulting in the formation of a Sr-hydroxyl-complex:

$$SrO_{(s)} + H_2O_{(l)} \rightarrow Sr(OH)_{2_{(S)}}$$

Compared to SrO, this hydroxyl-complex reacts significantly stronger to acidic treatment. The substrates were then etched in a buffered HF-solution (NH_4F-HF, pH = 4,6) for 30 s at room temperature:

$$Sr(OH)_{2_{(S)}} + 2\,HF_{(aq)} \rightarrow SrF_{2_{(aq)}} + 2\,H_2O_{(aq)}$$

After thoroughly rinsing the substrates in de-ionized water, they were thermally annealed under oxygen flow for 1 h at 1100 °C. According to M. R. Castell [109] and T. Nishimura et al. [110], this treatment yields TiO_2 terminated substrates.

The substrates are (001) oriented with a miscut of about 0.1° towards (010). In some cases conductive Nb-doped $SrTiO_3$ substrates have been used to serve as bottom electrodes.

3.1.2 Orthorhombic substrates

The crystal structure of all orthorhombic substrates used in this work exhibits the space group Pbmn. The substrates are $(110)_o$ oriented with a nominal miscut of 0.1° towards the $[001]_o$ or $[1\text{-}10]_o$ direction. The orthorhombic and pseudocubic RT lattice parameters are given in Table 3.1. For easier comparison of different substrates and films, the orthorhombic lattice parameters (denoted by the index “o”) have been converted into pseudocubic lattice parameters (denoted by the index “c”) according to Vaillionis et al. [111]:

$$a_c = \frac{c_o}{2}, \quad (3.1)$$

$$b_c = \frac{\sqrt{a_o^2 + b_o^2 - a_o b_o cos\gamma_o}}{2}, \quad (3.2)$$

$$c_c = \sqrt{\frac{a_o^2 + b_o^2 - 2b_c^2}{2}}, \quad (3.3)$$

$$\alpha_c = \text{acos}\left(\frac{b_c^2 + c_c^2 - a_o^2}{2b_c c_c}\right). \quad (3.4)$$

Figure 3.1 schematically illustrates the relationship between the orthorhombic and the pseudocubic unit cell. The pseudocubic unit cell is rotated by 45° with respect to the orthorhombic unit cell. Since the angle γ_o between $[110]_o$ and $[1\text{-}10]_o$ is 90° for the substrates presented in this chapter, it follows that $b_c = c_c$. The monoclinic angle α_c of the pseudocubic lattice cell is situated between b_c and c_c in the $(100)_c$ plane. The monoclinic distortion angle is given by $\beta_c = \alpha_c - 90°$.

The almost square-like surface unit cell of the rare earth (RE = Dy, Tb, Gd, Nd) scandate substrates (Table 3.1) implies a quasi-fourfold symmetry. However, the surface symmetry is only 2-fold according to the positions of the O^{2-} ions. They are aligned in straight rows along $[1\text{-}10]_o$ whereas a zig-zag pattern is observed along $[001]_o$. One particular example for the described behavior is $TbScO_3$, as illustrated in Fig. 3.2.

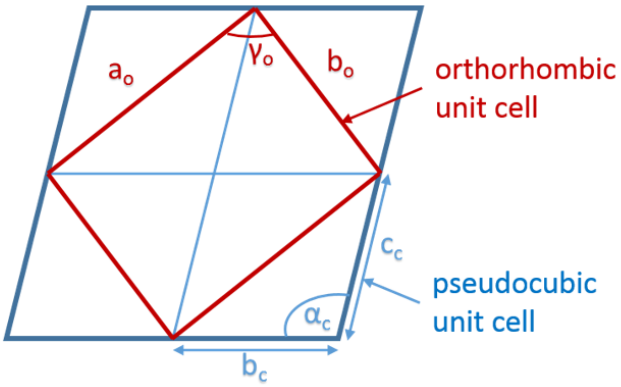

Fig. 3.1: Schematic illustration of the relationship between the orthorhombic and pseudocubic unit cell. Adapted from [111].

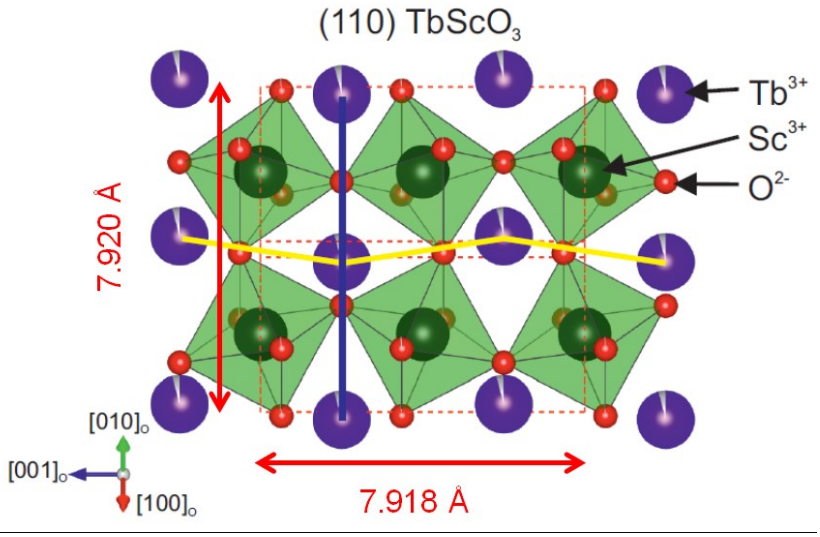

Fig. 3.2: $(110)_o$ lattice of $TbScO_3$. The red dashed line marks the orthorhombic unit cell boundaries. Adapted from [38].

Prior to depositions the substrates have been annealed in pure oxygen flow at various conditions (Table 3.1), in order to obtain single terminated surfaces, as described for $SrTiO_3$ above. From experiments, it is known that the different conditions listed in the table yield both single terminations and very smooth substrate surfaces [112, 113]. Thereby, no further chemical treatment was necessary. Since all cations in the rare-earth scandate and $NdGaO_3$ substrates attain oxidation levels of +3, AO^{+1} and BO_2^{-1} terminated surfaces have different polar states. Thermal treatment results in NdO terminated surfaces for $NdGaO_3$ substrates and ScO_2 terminated surfaces for all rare earth scandate substrates [113].

Table 3.1: Lattice parameters and thermal treatments of orthorhombic substrates [114, 115].

Substrates	***orthorhombic lattice parameters* (Å)**			**Pseudocubic lattice parameters (Å)**		**Annealing Temperature (°C)**	**Annealing Time (h)**
	a_o	b_o	c_o	a_c	$b_c = c_c$		
$NdGaO_3$ (110) [114]	5.428	5.498	7.708	3.854	3.863	1050	1
$DyScO_3$ (110) [114]	5.442	5.719	7.904	3.952	3.947	1050	10
$TbScO_3$ (110) [115]	5.466	5.731	7.917	3.959	3.960	1100	1
$NdScO_3$ (110) [115]	5.575	5.776	8.003	4.002	4.014	1000	10

3.2 Films

3.2.1 $NaNbO_3$

At room temperature, bulk $NaNbO_3$ is orthorhombic (space group Pbcm) with the lattice parameters a_o = 5.5687 Å, b_o = 5.5047 Å, and c_o = 15.523 Å [116]. The Goldschmidt tolerance factor is 0.84, which is a relatively small value. Accordingly, $NaNbO_3$ exhibits an antiferroelectric symmetry due to complex BO_6 octahedra rotations, described by $a^-b^+a^-/a^-b^-a^-$ in the Glazer notation (see chapter 1.1 (Perovskites)). When bulk $NaNbO_3$ is cooled down, it undergoes an unusual sequence of six phase transitions, going over from the high temperature cubic phase to the low temperature rhombohedral ferroelectric phase. Currently, these transitions are not fully understood (see Table 3.2) [117]. The Curie temperature is 641°C [118]. The RT antiferroelectric P-phase can be transformed to the ferroelectric phase by weak electric fields, doping or by applying high pressure, e.g. from the PFM measurement tip or stress due to lattice mismatch [118-120]. The pseudocubic lattice parameters of $NaNbO_3$ were calculated to a_c = 3.881 Å and b_c = c_c = 3.915 Å, with a monoclinic distortion angle β_c = 0.67° [23]. These numbers highlight the anisotropy of $NaNbO_3$. Depending on the applied substrate, different orientations (a_c or c_c) are possible for thin films grown epitaxially. The free energy density has been estimated (see chapter 1.4 (Biaxial strain)) for coherent film growth on different substrates based on the elastic coefficients of $KNbO_3$. With either a_c or b_c (=c_c) pointing in the vertical direction and two possible in-plane variants (rotated by 90°), there may be four different film orientations. The configuration with the lowest free energy density is presented in Table 3.3. Here, a_c-orientation (c_c -orientation) means that the pseudocubic a_c (c_c or b_c) axis is oriented along the out-of-plane direction.

Table 3.2: Phase transitions of bulk $NaNbO_3$. Adapted from [117].

Temperature (°C)	Phase	Symmetry	Tilt system
< -50 [122]	*N*	Rhombohedral	$a^- a^- a^-$
-50-373 [123]	*P*	Orthorhombic	$a^- b^+ a^- / a^- b^- a^-$
373-480 [124]	*R*	Orthorhombic	$a^- b^+ c^+ / a^- b^0 c^+$
480-520 [124]	*S*	Orthorhombic	$a^- b^+ c^+$
520-575 [124]	T_1	Orthorhombic	$a^- b^0 c^+$
575-641 [125]	T_2	Tetragonal	$a^0 a^0 c^+$
> 641 [118]	Cubic	Cubic	$a^0 a^0 a^0$

Table 3.3: Estimation of the minimal free energy density of strained $NaNbO_3$ thin films on various substrates. Also shown are the resulting lattice mismatches.

$NaNbO_3$ films on	Free energy density (GPa)	Film orientation	In plane lattice mismatch in $[1\text{-}10]_o/[100]_c$ direction (%)	In plane lattice mismatch in $[001]_o/[010]_c$ - direction (%)	Average in plane lattice mismatch (%)
$NdGaO_3$	$3.6*10^{-2}$	c_c	-1.33	-0.70	-1.02
$SrTiO_3$	$3.6*10^{-3}$	c_c	0.62	-0.26	0.18
$SrTiO_3$	$2.3*10^{-3}$	a_c	-0.26	-0.26	-0.26
$DyScO_3$	$2.8*10^{-2}$	a_c	0.82	0.95	0.89
$TbScO_3$	$4.5*10^{-2}$	a_c	1.15	1.12	1.14

During the course of this thesis, papers concentrating on the ferroelectric domains of PLD-grown [126], [127] and MOCVD-grown [23] $NaNbO_3$ films have been published. On the latter, the impact of biaxial-lattice strain on phase transitions [128] and ferroelectric properties [129] with film thicknesses up to 80 nm was also recently discussed.

3.2.2 $KNbO_3$

At room temperature, $KNbO_3$ is also orthorhombic (space group Amm2) [130]. Opposed to $NaNbO_3$, the Goldschmidt tolerance factor of $KNbO_3$ is large (0.96), so that there occurs practically no tilt in the octahedra. Bulk $KNbO_3$ exhibits three phase transitions during cooling, and goes over from cubic $\rightarrow$ tetragonal $\rightarrow$ orthorhombic $\rightarrow$rhombohedral [131] (see Fig. 3.3). It is ferroelectric at RT with lattice parameters a_o = 5.697 Å, b_o = 5.721 Å and c_o = 3.971 Å. The Curie temperature is 435 °C. According to Vaillionis et al., the pseudocubic lattice parameters are calculated to a_c = 3.971 Å and b_c = c_c = 4.037 Å. The monoclinic distortion angle β_c between the b_c and c_c direction is 0.24°. Again, a large anisotropy of the lattice parameters is apparent, similar to $NaNbO_3$. Table 3.4 shows the configuration with minimal in-plane stress, film surface orientation and the resulting in-plane lattice mismatch of $KNbO_3$ on the substrates used in this work.

Table 3.4: Minimal in plane stress of $KNbO_3$ on various substrates. Also shown are the resulting lattice mismatches.

$KNbO_3$ films on	Free energy density (GPa)	Film orientation	In plane lattice mismatch in $[1\text{-}10]_o/[100]_c$ direction (%)	In plane lattice mismatch in $[001]_o/[010]_c$ - direction (%)	Average in plane lattice mismatch (%)
$SrTiO_3$	$3.1*10^{-1}$	c_c	-4.08	-1.88	-2.98
$DyScO_3$	$1.3*10^{-1}$	c_c	-3.05	-0.70	-1.88
$TbScO_3$	$1.0*10^{-1}$	c_c	-2.73	-0.53	-1.63
$NdScO_3$	$1.7*10^{-2}$	c_c	-1.40	0.55	-0.43

3.2.3 $K_xNa_{1-x}NbO_3$

Solid solutions of $KNbO_3$ and $NaNbO_3$ are orthorhombic and stable for all x [0;1] at RT. The structural symmetry as well as the temperature induced phase transitions strongly depend on the compositional parameter x. Figure 3.3 presents the complex nature of the phase transitions in bulk $K_xNa_{1-x}NbO_3$, depending on composition x and temperature T [132]. Note, that $K_xNa_{1-x}NbO_3$ exhibits several morphotropic phase boundaries (MPB), i.e. structural phase changes due to changes in material composition, and not temperature. At $x \approx 0.2$ and ≈ 0.4 there is a change in the tilt system, while at $x \approx 0.5$ one observes a change in the monoclinic distortion angle [133]. Since ferroelectric materials at MPBs show excellent electromechanical properties, they are very interesting for technological applications [134]. For $x > 0.06$ bulk $K_xNa_{1-x}NbO_3$ is ferroelectric at RT.

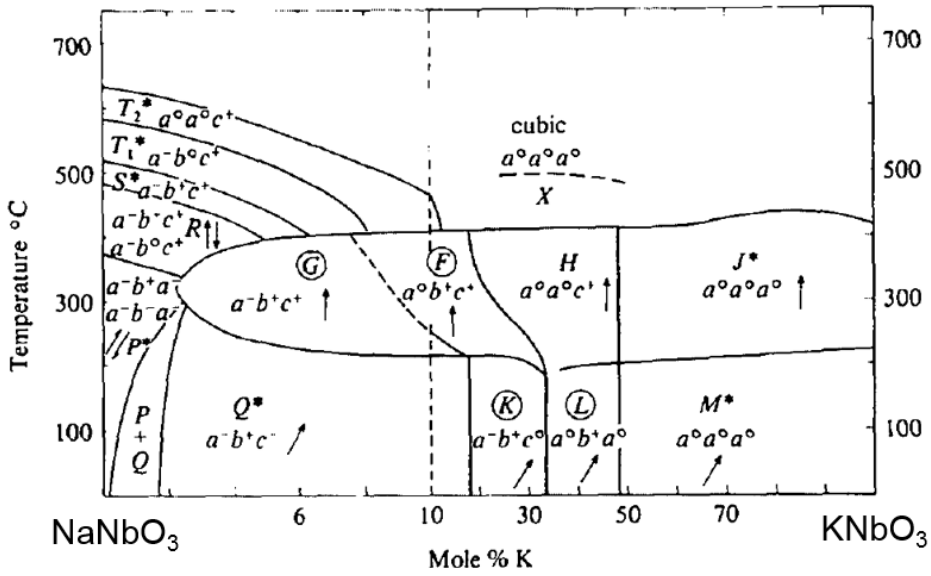

Fig. 3.3: Phase diagram of bulk $K_xNa_{1-x}NbO_3$ in dependence of x and T. Adapted from [132].

Due to the structural phase transition at MPBs, the lattice parameters do not follow the linear Vergard's law over the whole range of *x*. Instead, there are two approximately linear regimes ($x < 0.35$ and $x > 0.35$), as identified by Wu et al. [135] (Fig. 3.4). However, the lattice parameters presented by Wu et al. for $x = 0$ and $x = 1$ do not agree with the ones described in Chapters 3.2.1 and 3.2.2 on $NaNbO_3$ and $KNbO_3$, respectively. Discrepancies in reported lattice parameters are often observed in literature on oxide materials, which is usually attributed to slight variations in the exact composition of the material. In this work, the lattice parameters of the bulk $K_xNa_{1-x}NbO_3$ targets have therefore been determined by means of Powder XRD, with sufficient accuracy to estimate the lattice mismatch (see chapter 4 (Target preparation)). The resulting pseudocubic lattice parameters are given in Table 3.5. For $x = 0.25$, the lattice parameters could not be determined, as no statistical distribution of N and K ions was achieved in the target (see chapter 4 (Target preparation). To still have an estimate, the average value of $NaNbO_3$ and $K_{0.5}Na_{0.5}NbO_3$ has been used, which is in good agreement with the value determined by Wu et al..

Table 3.6 presents expected orientations and average lattice mismatch of $K_xNa_{1-x}NbO_3$ films with different composition *x* (based on the lattice parameters given in Table 3.5), and on various substrates.

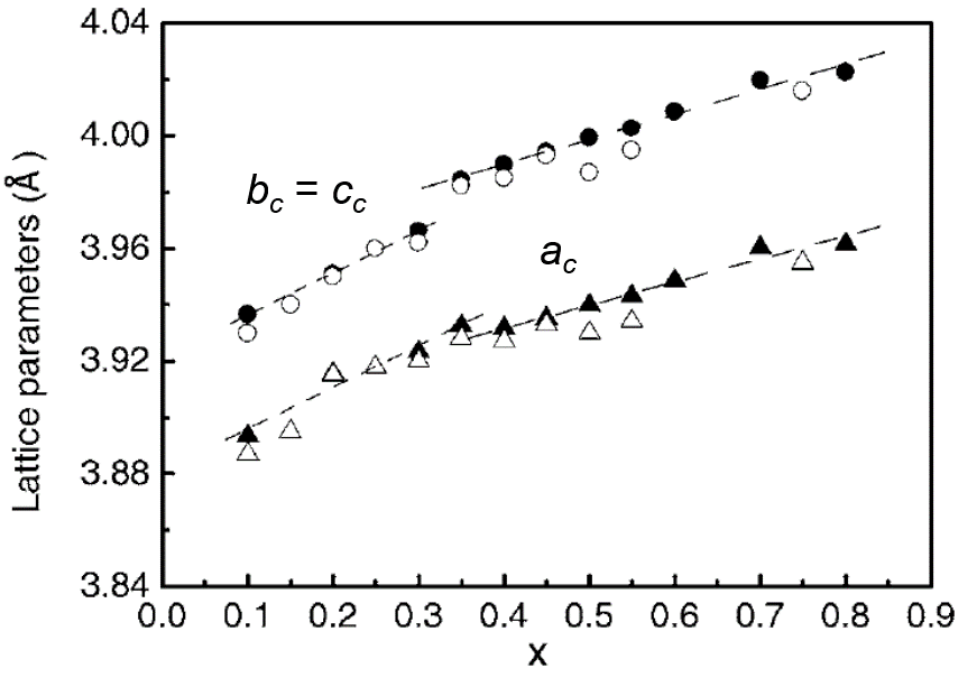

Fig. 3.4: Pseudocubic lattice parameters of $K_xNa_{1-x}NbO_3$ ceramics in dependence of *x*. Adapted from [135].

Table 3.5: Pseudocubic lattice parameters of the bulk $K_xNa_{1-x}NbO_3$ ceramics used as PLD targets for various *x*. Estimated error: ±0.003 Å.

$K_xNa_{1-x}NbO_3$	***pseudocubic lattice parameters***	
x	***a_c* (Å)**	***b_c* = *c_c* (Å)**
0.25	3.912	3.960
0.5	3.942	4.004
0.75	3.960	4.021

Table 3.6: Film orientation and average in plane lattice mismatch of $K_xNa_{1-x}NbO_3$ films for various *x* on the substrates used in this work.

Substrate	Expected film orientation			Average in plane lattice mismatch (%)		
	x = 0.25	*x* = 0.5	*x* = 0.75	*x* = 0.25	*x* = 0.5	*x* = 0.75
$SrTiO_3$	c_c	c_c	c_c	-0.8	-1.7	-2.2
$DyScO_3$	a_c	c_c	c_c	0.3	-0.6	-1.0
$NdScO_3$	a_c	a_c	a_c	1.2	0.1	-0.3

Chapter 4: Target preparation

$NaNbO_3$ films were deposited using a commercially available, stoichiometric ceramic target (SurfaceNet GmbH, Germany) as well as from self-made non-stoichiometric sodium excess targets with Na/Nb-ratios of 1.11, 1.22 and 1.50 in the raw material mixture. The $K_xNa_{1-x}NbO_3$ films with $x \leq 0.75$ were deposited from self-made targets with a compositional ratio of x in the powders used for the target fabrication. The targets were prepared by conventional solid-state reaction. Anhydrous sodium carbonate (Na_2CO_3, 99.997% purity), potassium carbonate (K_2CO_3, 99.997% purity) and niobium oxide (Nb_2O_5, 99.9985% purity) powders were mixed, milled and pressed into pellets of 2.5 cm in diameter at 2000 bar. Subsequently, the pellets were first calcined for six hours and in a second step sintered for 12 hours at 950 °C inside a Pt/Au crucible in ambient air.

4.1 $NaNbO_3$ targets

ICP-OES data of the ceramic $NaNbO_3$ targets shown in Table 4.1 reveal that the calcination and sintering process always slightly reduce the Na/Nb ratio in the targets (determined by ICP-OES) compared to the original powder mixture Na/Nb ratio. This is attributed to the high volatility of Na_2O at elevated temperatures [25]. It is striking that with increasing amount of Na_2CO_3 in the raw material powder the Na/Nb ratio in the sintered targets is increased. XRD powder measurements of the fabricated targets as well as of the commercial target with a nominal Na/Nb ratio of 1 are presented in Fig. 4.1. Only the commercial target exhibits a pure $NaNbO_3$ phase. For the ceramic targets with Na/Nb > 1 extra Bragg peaks appear in the diffraction pattern which is attributed to Na_3NbO_4 occurring additionally to the $NaNbO_3$ perovskite phase. The Bragg peaks of the extra phase are incrementally more pronounced with increasing Na excess in the targets (Fig. 4.1). The appearance of the Na_3NbO_4 phase for Na_2O rich conditions is in agreement with the Na_2O-Nb_2O_5 phase diagram [136]. No further phases have been observed by powder XRD. The influence of the sodium rich targets on film growth will be discussed in chapter 5.1.3.

Table 4.1: Na/Nb ratios of the self-made targets before and after conventional solid reaction.

	Na/Nb ratio before calcination and sintering		
	1.11	1.22	1.50
Na/Nb ratio of sintered targets	1.09 ± 0.02	1.17 ± 0.02	1.37 ± 0.02

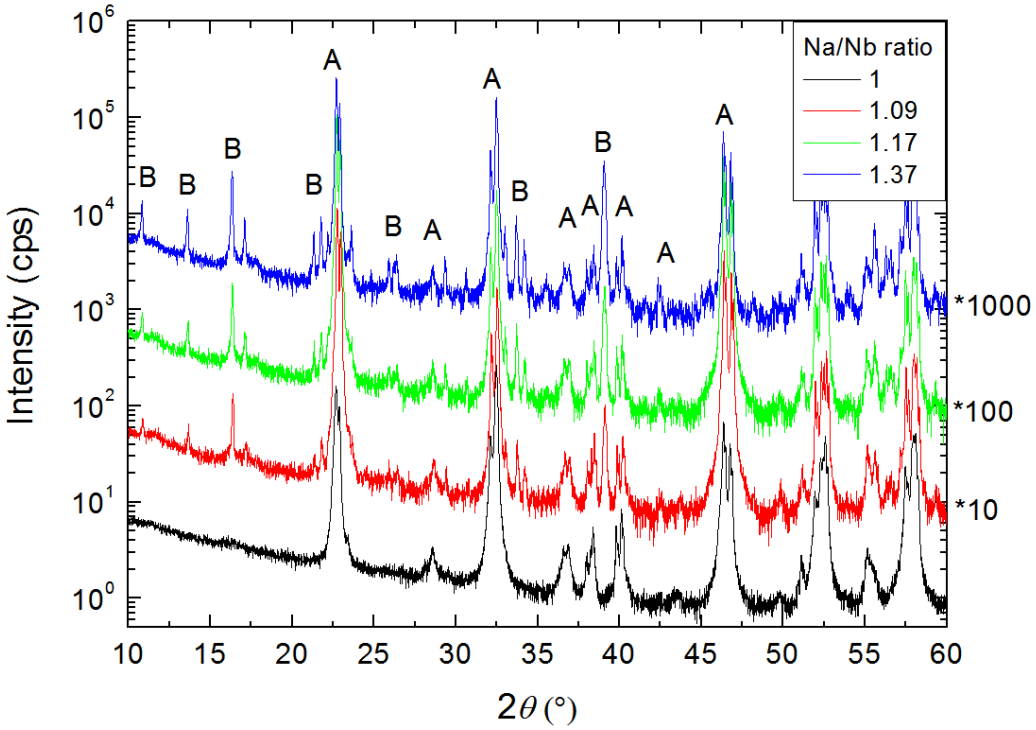

Fig. 4.1: Powder X-Ray diffraction patterns of $NaNbO_3$ targets with increasing Na/Nb ratio deduced from ICP-OES measurements (from bottom to top). The commercial target has a nominal Na/Nb ratio of 1. Sodium excess targets additionally exhibit a Na_3NbO_4 phase. $NaNbO_3$ and Na_3NbO_4 Bragg reflection peaks are marked by **A** and **B**, respectively.

4.2 $K_xNa_{1-x}NbO_3$ targets

$K_xNa_{1-x}NbO_3$ targets with a K/Na ratio in the raw target mixture corresponding to *x* have been investigated by ICP-OES for *x* = 0.25, 0.5 and 0.75 (Table 4.2). It can be seen that only for *x* = 0.5 the targeted K/Na ratio was not exactly produced, whereby the discrepancy is very small. For *x* = 0.75 the deviation from the stoichiometric ratio is within the error interval. Seemingly, the alkali to niobium ratio tends to decrease with increasing K content. This observation is explained by a still higher volatility of K compared to Na. In order to comprehensively describe the $K_xNa_{1-x}NbO_3$ films presented in chapter 6, the values 0.5 and 0.75 will be used for *x* in this work.

Table 4.2: K/Na ratios of the self-made targets before and after conventional solid reaction.

	x of K_xNa_{1-x} in powder before calcination and sintering		
	0.25	0.5	0.75
x of $K_xNa_{1-x}NbO_3$ sintered targets	0.25 ± 0.01	0.48 ± 0.01	0.76 ± 0.01
(K+Na)/Nb ratio of sintered targets	1.00 ± 0.02	0.98 ± 0.02	0.96 ± 0.02

Powder X-ray diffraction patterns of $K_xNa_{1-x}NbO_3$ targets with increasing *x* mixed with a SiO_2 (alpha quartz) standard as measured are shown in Fig. 4.2. It is clear that with increasing *x* the *2θ*-values of the targets peak positions decrease, which means that the lattice parameters increase as is expected for $K_xNa_{1-x}NbO_3$ (see chapter 3.2.3). The use of a SiO_2 (alpha quartz) standard allows a more quantitative investigation of the targets lattice parameters. The lattice parameters of $K_xNa_{1-x}NbO_3$ found in literature vary over a large interval, which is assumed to be due to deviations of the stoichiometric composition (vacancies), structural defects (e.g. dislocations) or impurities. The purpose of the investigation presented below was to determine the lattice parameters in the precise targets used for the deposition of the films discussed in this work within reasonable accuracy (~0.2%). This attempt was not successful in the case of *x* = 0.25 as here the diffraction peaks are very broad and smeared out over the different orientations. According to calculations by B. P. Burton and T. Nishimatsu [137] a solid solution with statistically distributed K and Na is expected for *x* = 0.25 for sintering temperatures above 1450°C (see Fig. 4.3). This high temperature was not achievable with the furnace used for this work. In contrast the diffraction peaks for *x* = 0, *x* = 0.5 and *x* = 0.75 are very sharp, which agrees with the above mentioned calculations, as for *x* ≥ 0.5 the formation of a solid solution is predicted already at ~500°C.

The SiO_2 standard was used to counter systematic errors of the measurements and calibrate peak positions related to the target materials relative to the peak position of the standard. The contribution of $K\alpha_2$ was suppressed by Rachinger-correction. This way, the net-plane distances *d* were determined from the *2θ*–values of the peak positions. For the various orientations both pseudocubic (index “c”) and orthorhombic (index “o”) lattice parameters are given in Table 4.3. Based on the standard deviation of the peak positions of SiO_2 as measured compared to literature data (data sheet 00-046-1045 International Centre for Diffraction Data) and the variations of the lattice parameters given in Table 4.3 an error of ±0.003 Å is assumed. For the purpose of estimating the lattice mismatch induced strain in the films on the different substrates, the derived values are sufficiently accurate.

Table 4.3: Lattice parameters of $K_xNa_{1-x}NbO_3$ ceramic targets. Estimated error: ±0.003 Å.

	Target composition		
Index	*x* = 0	*x* = 0.5	*x* = 0.75
$100_c = 001_o$	3.880	3.942	3.960
$001_c = 010_c$	3.916	4.004	4.021
100_o	5.569	5.678	5.703
010_o	5.510	5.619	5.672

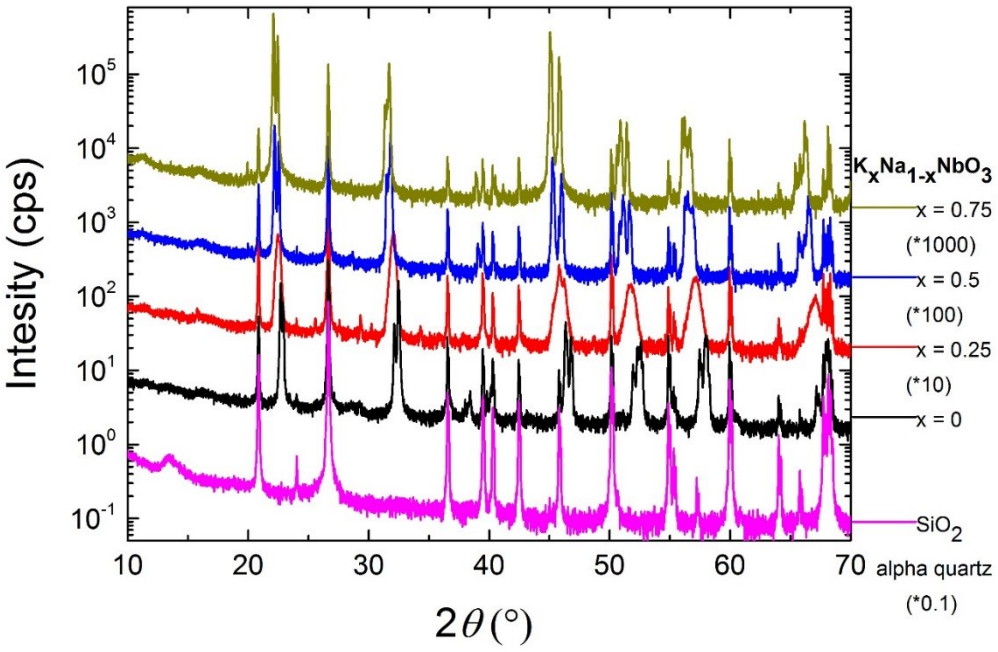

Fig. 4.2: Powder X-Ray diffraction patterns of $K_xNa_{1-x}NbO_3$ targets with increasing x mixed with a SiO_2 (alpha quartz) standard.

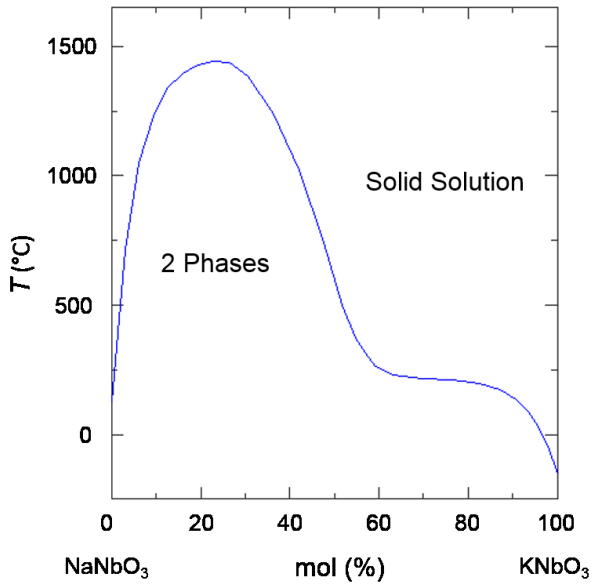

Fig. 4.3: Miscibility gap between $NaNbO_3$ and $KNbO_3$. Adapted from [137].

Chapter 5: Discussion and Results on $NaNbO_3$ thin films

In this chapter the surface morphology, lattice parameters of and vacancy density in $NaNbO_3$ films on $NdGaO_3$, $SrTiO_3$, $DyScO_3$ and $TbScO_3$ substrates in dependence on the deposition conditions will be analyzed. Comparison of the incorporated lattice strain in films on different lattice mismatched substrates is best achieved under stoichiometric 2D growth. Grain boundaries, which are present in films deposited in 3D-growth mode, are reported to incorporate a high density of misfit dislocations [138]. Thus, in this case, plastic lattice relaxation is expected to start at smaller film thicknesses compared to 2D-grown films. They can also be a source of laterally inhomogeneous film properties and are reported to have a deteriorating influence on domain wall formation and mobility (e.g. through pinning) in some cases [139]. Optimization of the growth process with regard to the film stoichiometry is of special interest. PLD growth of complex oxides often results in the incorporation of a high density of oxygen vacancies in the films. The high volatility of sodium results in a further challenge for stoichiometric film growth. Therefore, the impact of increasing oxygen background pressure and Na/Nb ratio in the PLD targets on the deposition process and the resulting Na/Nb ratio in the films will be shown. A detailed discussion in conjunction with ferroelectric domain formation and polarization direction of tensilely strained films revealed that growth under optimized conditions yielded well-ordered ferroelectric domain structures. The development of these domains with film thickness was found to be significantly different compared to films grown by MOCVD. The investigation of the local ferroelectric hysteresis loops of $NaNbO_3$ films on conductive Nb-doped $SrTiO_3$ substrates with low average biaxial strain in dependence of film stoichiometry will result in the susceptibility of the ferroelectric properties of $NaNbO_3$ on Na- and O-vacancies.

Distinction from previous works:
2D growth of fully strained $NaNbO_3$ films by PLD has been, apart from the results presented in this work, reported only very recently (2014) [140]. Tyunina et al. investigated the dependence of the Curie temperature of $NaNbO_3$ films on the lattice strain by ellipsometry measurements. However, no systematic investigations of the dependence of film stoichiometry on the deposition conditions and the subsequence impact on the ferroelectric properties have been reported for 2D-grown $NaNbO_3$ thin films, yet.

5.1 Optimization of film stoichiometry

In order to avoid structural degradation due to plastic lattice relaxation the film thickness in this section is limited to max. 15 nm, well below the critical thickness for all used film/substrate systems (see chapter 5.3).

5.1.1 Initial depositions at low pressure (0.05 mbar)

All films described in this subsection were deposited at 600°C substrate temperature and 0.05 mbar oxygen background pressure (see Table 5.1, the results presented in this chapter have in part been published in [141])). Lattice mismatched $NdGaO_3$, $SrTiO_3$, $DyScO_3$ and $TbScO_3$ substrates were used in order to induce different lattice strains in the films (see Table 3.3 in chapter 3 (Materials)).

Table 5.1: Deposition conditions of $NaNbO_3$ films on various substrates

Laser fluence (J/cm²)	2.2
Pulse repetition (Hz)	5
Target to substrate distance (mm)	54
Number of laser pulses	185
Substrate temperature (°C)	600
Oxygen background pressure (mbar)	0.05

2D growth

The films retained the step-and-terrace nature of the substrates when the film thickness was limited to 15 nm (Fig. 5.1). The average roughness of the film surface (RMS) is about 0.2 nm in all cases. The step-height and is about 0.4 nm and the step width are 150-330 nm, depending on the actual miscut of the stepped substrate. In-situ RHEED measurements of the intensity of the specular spot during growth of a $NaNbO_3$ film is exemplarily shown in Fig. 5.2(a) on $DyScO_3$. The intensity curves look similar on all other substrates used. After an initial increase, the measured intensity during growth is constant. The RHEED diffraction pattern taken after the deposition process had ended (Fig. 5.2(c)) is typical for a smooth crystalline surface. Together with the stepped surface morphology of the film, the constant intensity during the RHEED measurements reveals step-flow growth. The initial drop in the measured intensity is due to a change in the electronic surface states of film and substrate as is also visible from the low intensity of the bare substrate (Fig. 5.2(b)).

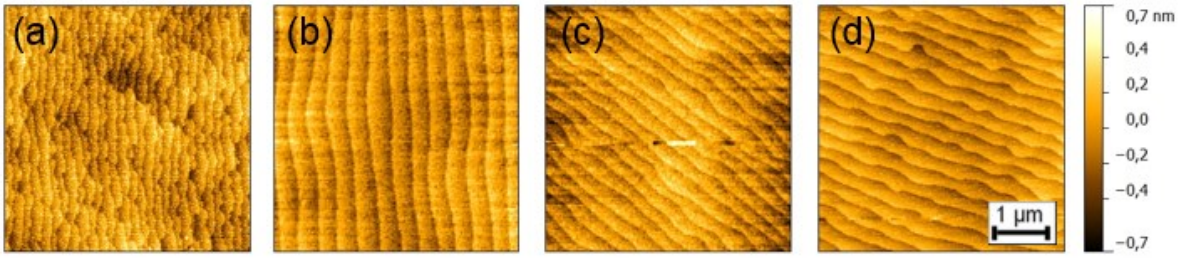

Fig. 5.1: Surface morphology (AFM) of a $NaNbO_3$ films deposited on (a) $NdGaO_3$, (b) $SrTiO_3$, (c) $DyScO_3$ and (d) $TbScO_3$ substrates.

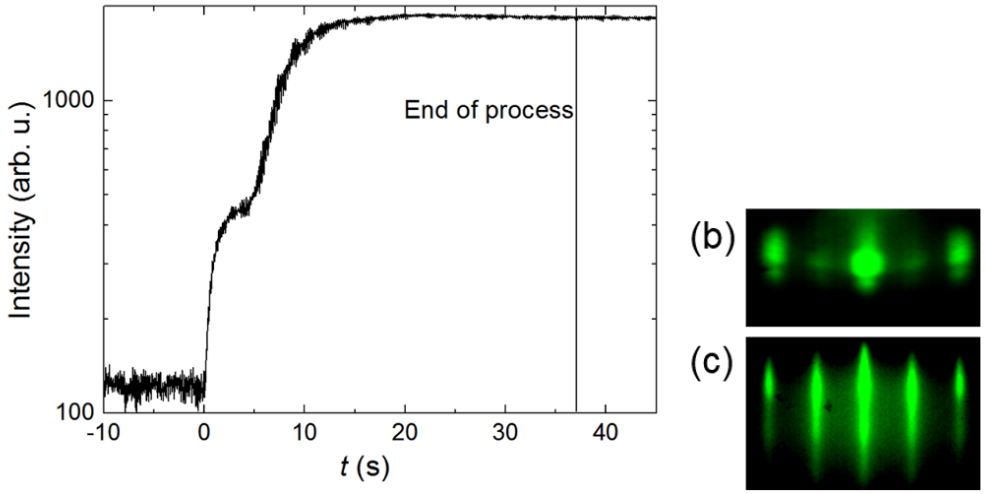

Fig. 5.2: (a) RHEED intensity as a function of laser pulses and (b) RHEED-diffraction pattern of a bare $DyScO_3$ substrate and (c) of a 15 nm thick $NaNbO_3$ film deposited thereon.

Strain state and film orientation

In Fig. 5.3(a), the HRXRD pattern of a $NaNbO_3$ film on a $DyScO_3$ substrate in the 2θ range between 15° and 55° is shown. Apart from the $(001)_c$ and $(002)_c$ Bragg reflections no peaks related to $NaNbO_3$ can be seen revealing that the film is phase pure. Similar results were obtained for $NaNbO_3$ films on $TbScO_3$, $SrTiO_3$ and $NdGaO_3$ substrates. The thickness oscillations visible at higher magnification (Fig. 5.3(b)) demonstrate the smooth interface and surface as well as good structural quality of the film. From the angular spacing of the minima of these thickness oscillations, the film thickness was determined to be 15 nm (see chapter 2.5 (XRD)). The full width of half-maximum (FWHM) of the rocking curve (ω-scan) of the films is 0.02°, proving that the vertical net planes are highly ordered. Comparable values have been reported for heteroepitaxially grown $BaTiO_3$ films (0.08°) [142] and $BiFeO_3$ films (0.008°) [143] on $SrTiO_3$ substrates. The out-of-plane lattice parameter of the film was derived from the film peak position relative to the substrate peak position. In Fig. 5.3(b) it is clearly shown that the out-of-plane lattice parameter of $NaNbO_3$ thin films is strongly determined by the substrate. The evaluation of the position of the film peak with respect to substrate peak allows the

determination of the out-of-plane lattice parameter (see Table 5.2). The film peak position on $DyScO_3$ closely matches the bulk position of a_c-oriented stoichiometric $NaNbO_3$. The in-plane lattice parameters of the films were investigated by reciprocal space maps (RSM) in vicinity of a variety of asymmetric Bragg reflections of the respective substrates. The RSM around the $DyScO_3$ $(444)_o$ and $(260)_o$ Bragg reflections are exemplarily shown in Fig. 5.4. The film has the same in-plane lattice parameter as the substrate, i.e. the film is coherently grown on the substrate. $NaNbO_3$ films with a thickness of 15 nm were also grown under full in plane lattice strain on $TbScO_3$, $SrTiO_3$ and $NdGaO_3$ substrates. Tensilely (compressively) strained films exhibit smaller (larger) out-of-plane lattice parameters. Since the films presented in Fig. 5.3(b) are all fully strained, the film orientation and strain state of $NaNbO_3$ films on the various substrates can be deduced from comparing their respective out-of-plane lattice parameter with the bulk lattice parameters of the respective orientations. Tensilely strained $NaNbO_3$ films on $TbScO_3$ and $DyScO_3$ substrates are a_c-oriented, whereas compressively strained $NaNbO_3$ films on $NdGaO_3$ are c_c-oriented. Furthermore, $NaNbO_3$ films on $SrTiO_3$ substrates deposited at 0.05 mbar oxygen pressure are c_c-oriented and compressively strained.

Off-stoichiometry in the films

The out-of-plane lattice parameter of the $NaNbO_3$ film on $SrTiO_3$ is significantly larger than expected. As the average lattice mismatch between film and substrate is small the film peak position in Fig. 5.3(b) is expected to be very close to the c_c or a_c position of bulk $NaNbO_3$ indicated by the vertical lines.

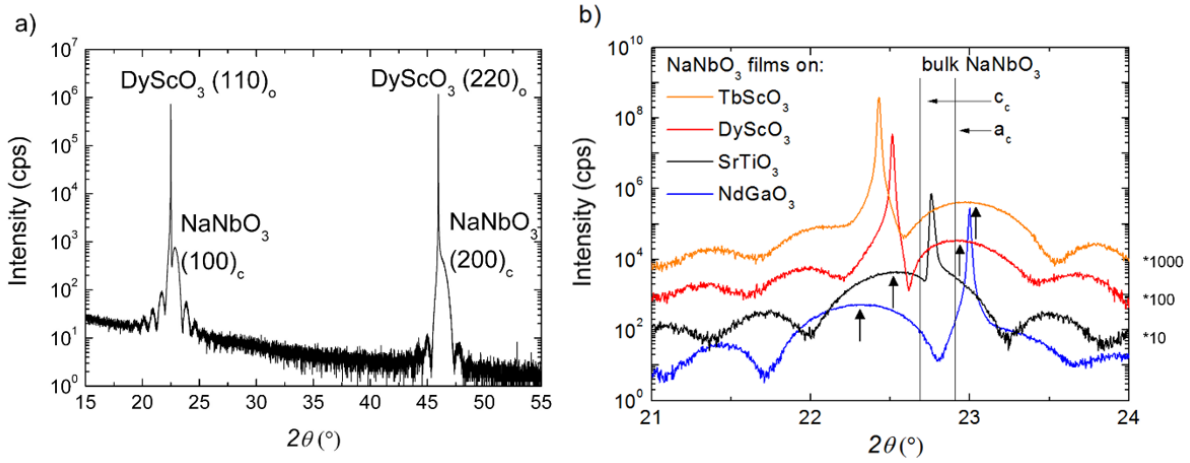

Fig. 5.3: (a) Long range HRXRD *θ-2θ* scan of a 15 nm $NaNbO_3$ thin film deposited at 600 °C and 0.05 mbar O_2 on a $DyScO_3$ substrate. (b) HRXRD *θ-2θ* scans of 15 nm thick $NaNbO_3$ films (indicated by arrows) on $TbScO_3$, $DyScO_3$, $SrTiO_3$ and $NdGaO_3$ substrates in the range of the $(110)_o$ respective $(001)_c$ Bragg peaks. The nominal $(100)_c$ Bragg peak positions of unstrained stoichiometric $NaNbO_3$ with a_c- and c_c-orientation are sketched as vertical lines.

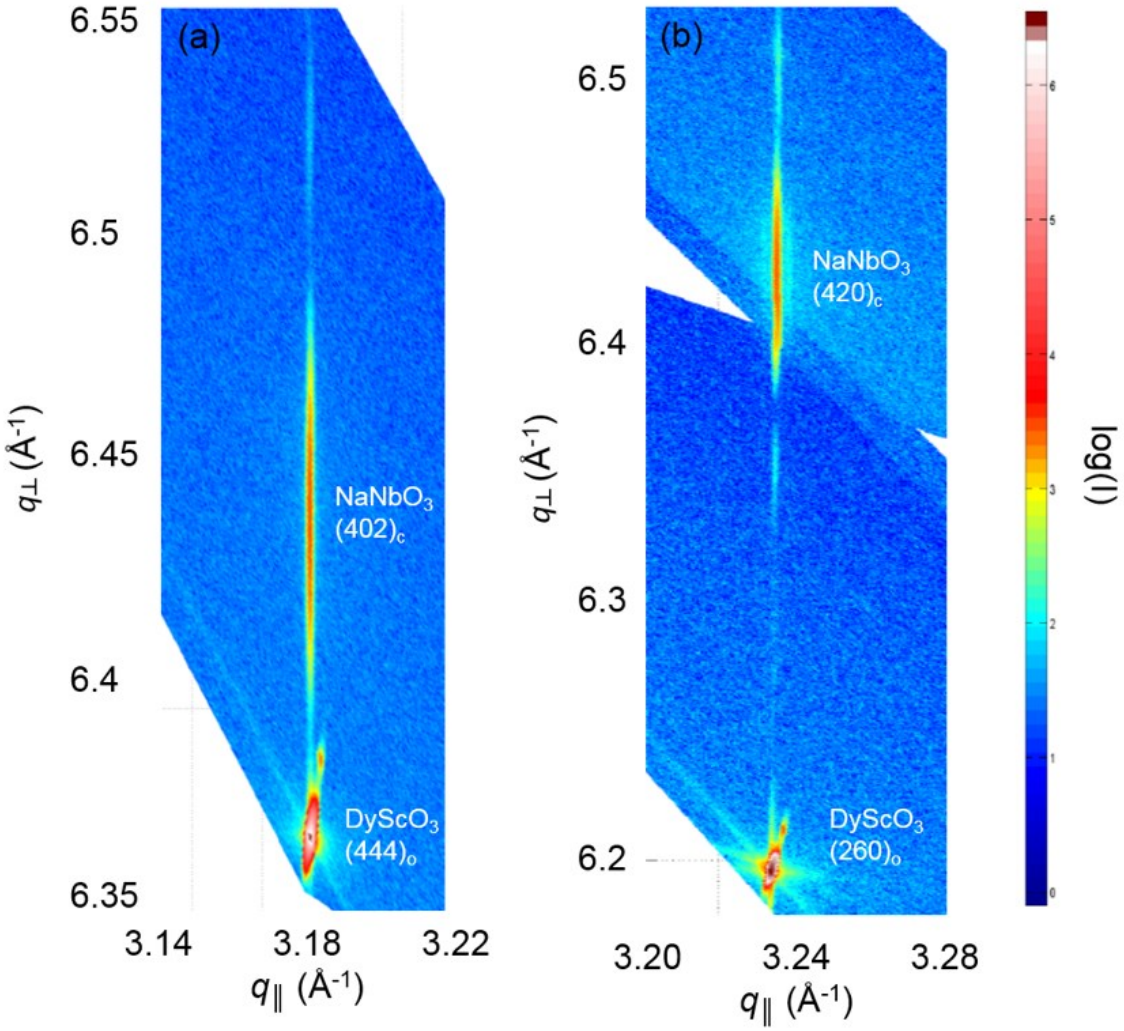

Fig. 5.4: HRXRD reciprocal space map of a $NaNbO_3$ film in vicinity of the asymmetric, orthorhombic (a) $(444)_o$ and (b) $(260)_o$ Bragg reflections of $DyScO_3$. The in-plane lattice parameter of film and substrate are identical, indicating coherent film growth.

The pseudocubic unit-cell volume of $NaNbO_3$ was calculated by multiplying the in- and out-of-plane lattice parameters. A complete set of these values is given in Table 5.2.

At first, I will concentrate on $NaNbO_3$ films on $SrTiO_3$ substrates since the average biaxial lattice strain is very small in this case. The approximate relative change of the unit-cell volume of a lattice under anisotropic biaxial strain compared to the unstrained lattice is described in chapter 1.4 (Biaxial strain).

The unit-cell volumes of bulk $NaNbO_3$ and the $NaNbO_3$ film on $SrTiO_3$ substrates are 59.48 and 60.20 Å³, respectively. These values result in a relative change $\Delta V/V$ = 1.2 %. From equation (1.12) with $(\Delta a/a)$ = -0.26 % and ν = 0.3 a value of $\Delta V/V$ = 0.3 % is calculated. The expected value for V is significantly lower than the experimental one. For comparison, $NaNbO_3$

Table 5.2: Pseudocubic lattice parameter and the corresponding unit-cell volume of $NaNbO_3$ thin films grown on the different substrates at 0.05 mbar. The experimental error interval for the out-of-plane lattice parameter and the unit-cell volume was estimated with ±0.002 Å and ±0.03 Å^3, respectively. Bulk unit-cell volume of $NaNbO_3$: 59.48 Å^3. Expected unit-cell volume for $v = 0.3$.

Substrate	**In-plane lattice parameter (Å)**		**Out-of-plane lattice parameter (Å)**	**Unit-cell volume (Å³)**	**Expected unit-cell volume (Å³)**
$NdGaO_3$	3.854	3.863	3.977	59.24	~ 58.54
$SrTiO_3$	3.905	3.905	3.948	60.20	~ 59.60
$DyScO_3$	3.952	3.947	3.879	60.40	~ 60.08
$TbScO_3$	3.959	3.960	3.856	60.45	~ 60.25

thin films grown on $SrTiO_3$ substrates by MOCVD at the significantly higher oxygen pressure of 15 mbar [128] exhibit tensile lattice strain, which can also be expected from Table 3.3, and a unit-cell volume matching almost the value for unstrained $NaNbO_3$.

The unit-cell volumes of $NaNbO_3$ films on $TbScO_3$, $DyScO_3$ and $NdGaO_3$ films were similarly compared with predicted values. The unit-cell volume of tensilely strained films on $TbScO_3$ and $DyScO_3$ substrates are increased compared to the volume of the unit cell of relaxed $NaNbO_3$, while it is reduced for films on $NdGaO_3$ substrates grown under compressive lattice strain. This behavior is in accordance with equation (1.13) as long as $\nu < ½$. However, all films exhibit unit-cell volumes, which are larger than expected from equation (1.12).

Oxygen vacancies - which are often observed for films grown by PLD [144] - are known to lead to a lattice expansion in perovskites [145, 146]. Therefore, it is assumed that the increased out-of-plane lattice parameters and unit-cell volumes of films grown by PLD under the deposition conditions described above are significantly determined by an oxygen deficiency in the films. Such off-stoichiometry could also explain why the Bragg reflection of the $NaNbO_3$ film on $DyScO_3$ substrate has not been substantially shifted to higher 2θ values as expected for fully tensilely strained films (Fig. 5.3(b)).

5.1.2 Improved film stoichiometry by increased oxygen background pressure

In order to verify the assumption that the expanded unit-cell volume is caused by oxygen vacancies, $NaNbO_3$ films with thicknesses up to 15 nm on $TbScO_3$, $DyScO_3$, $SrTiO_3$ and $NdGaO_3$ substrates were deposited at oxygen background pressures above 0.05 mbar at otherwise unchanged deposition parameters (the results presented in this chapter have been published in [141]). Since the results are very similar on all substrates, they will be discussed

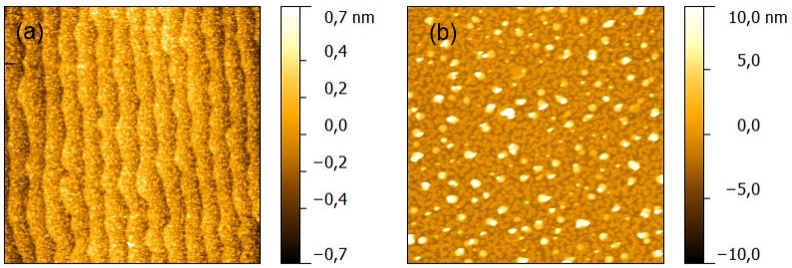

Fig. 5.5: Surface morphologies (AFM) of $NaNbO_3$ films deposited on $DyScO_3$ substrates at (a) 0.7 mbar and (b) at 2 mbar oxygen pressure. The substrate temperature was 600 °C.

exemplarily for $NaNbO_3$ films on $DyScO_3$. Increasing the oxygen pressure to 0.7 mbar yielded the deposition of films with surface morphologies similar to that of films grown at 0.05 mbar (Fig. 5.5(a)). RHEED measurements could only be performed to a maximum background pressure of 0.3 mbar (see chapter 2.2 (RHEED)). Therefore, it could not be concluded whether the film was deposited in step-flow or 2d-layer-by-layer growth mode. A further increase of the oxygen pressure to 2 mbar resulted in island growth if the substrate temperature was held constant at 600 °C (Fig. 5.5(b)).

Increased background pressure leads to a reduction of the mean free path length of the kinetic energies of the ablated species arriving at the substrate (see chapter 2.1 (PLD)); subsequently a reduced number of adatoms is able to overcome the diffusion barrier on the film surface [55]. In turn, enhanced surface diffusion can be reached by a higher thermal energy of the adatoms, provided by elevated substrate temperatures. Smooth and well-ordered films grown in step-flow or layer-by-layer growth mode could also be obtained at 2 mbar, when the substrate temperature was increased from 600 °C to 900°C (Fig. 5.6(a)). However, it has to be remarked that in the case of $NdGaO_3$ substrates, the use of a higher substrate temperature (900 °C) has a deteriorating effect on the surface morphology, clearly shown in Fig. 5.6(b). This could be caused by the high mobility of Ga leading to a diffusion of Ga atoms into the film during growth [147], presumably inducing growth of 3D islands. Hence, films on $NdGaO_3$ substrates, which were grown at 2 mbar and 900 °C, have not been further investigated. For the other substrates, the deposition at 900 °C and 2 mbar leads to smooth, stepped surfaces. However, a roughening of the step edges is observed, which is assumed to be caused by desorption due to high temperature.

The effect of increased O_2 partial pressure during the growth process on the lattice parameter of the $NaNbO_3$ films is summarized in Table 5.3. The out-of-plane lattice parameter and unit-cell volumes of $NaNbO_3$ films successively decrease with increasing oxygen partial pressure, independent of the strain state, indicating a reduced number of vacancies.

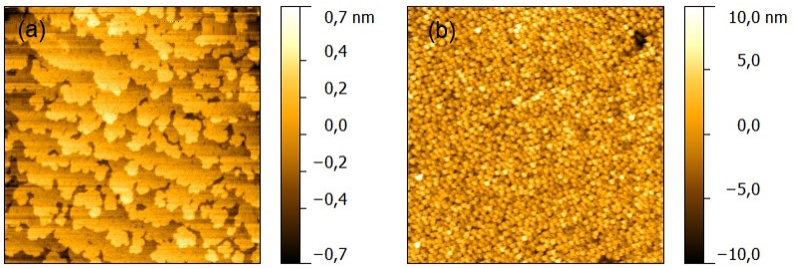

Fig. 5.6: Surface morphology (AFM) of $NaNbO_3$ films deposited at 900 °C and 2 mbar O_2 background pressure on $DyScO_3$ (a) and $NdGaO_3$ (b) substrates.

Like for PbO in $PbZr_xTi_{1-x}O_3$ thin films [148], it is supposed that a higher oxygen background pressure counteracts the high volatility of Na_2O, causing a reduced number of Na- and O-vacancies in the films. Also, the thermalization of the vaporized material by collisions is assumed to result in an approach to stoichiometry similar to the case of lead-based compounds [148]. This conclusion is also supported by EDX measurements of $NaNbO_3$ films on $TbScO_3$ substrates, where an increase of the Na/Nb ratio with increasing oxygen partial pressure during growth was detected (Fig. 5.7). Additionally to the thermalization of the plasma at high background pressures, the formation of a shock wave is expected (see chapter 2.1 (PLD)). The shock wave is predicted to exhibit an almost congruent stoichiometry with regard to the target.

A more detailed analysis of the data presented in Table 5.3 reveals that an increased oxygen partial pressure has a more pronounced impact on films grown under compressive lattice stress than on films under tensile stress. For example, the out-of-plane lattice parameter of $NaNbO_3$ films on $SrTiO_3$ changed by 0.8 % and 1.3 % when increasing the oxygen partial

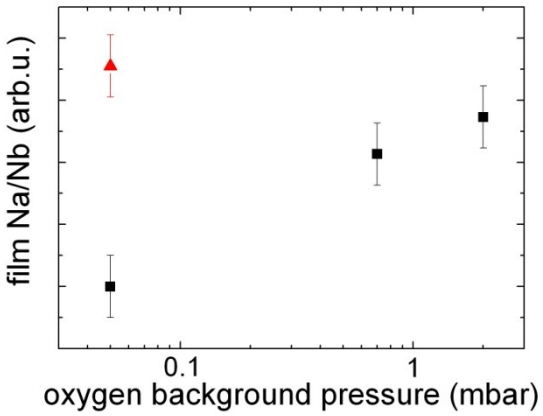

Fig. 5.7: Relative development of the Na/Nb ratio from EDX measurements of $NaNbO_3$ films on $TbScO_3$ in dependence of the oxygen background pressure during deposition using a stoichiometric target (black squares) and for comparison a target with Na/Nb ratio of 1.17 (red triangle).

Table 5.3: Out-of-plane lattice parameter $d_\perp$ of 15 nm $NaNbO_3$ films grown on the different substrates under increasing oxygen partial pressures and the corresponding unit-cell volume (V_{uc}). The experimental error intervals for the out-of-plane lattice parameter and the unit-cell volume were estimated with ±0.002 Å and ±0.03 Å^3, respectively. Bulk unit-cell volume of $NaNbO_3$: 59.48 Å^3. The right column shows the relative decrease of the out-of-plane lattice parameters of films grown at 0.7 mbar and 2 mbar compared to the value measured for films grown at 0.05 mbar.

	0.05 mbar, 600 °C		0.7 mbar, 600 °C		2 mbar, 900 °C		
Substrate	$d_\perp$ (Å)	V_{uc} (Å^3)	$d_\perp$ (Å)	V_{uc} (Å^3)	$d_\perp$ (Å)	V_{uc} (Å^3)	relative decrease of $d_\perp$
$NdGaO_3$	3.977	59.24	3.956	58.93	—	—	0.5 %/—
$SrTiO_3$	3.948	60.20	3.915	59.70	3.896	59.41	0.8 %/1.3%
$DyScO_3$	3.879	60.40	3.873	60.30	3.866	60.20	0.2 %/0.3%
$TbScO_3$	3.856	60.45	3.851	60.37	3.843	60.25	0.1 %/0.3%

pressure to 0.7 mbar and 2 mbar, respectively, while they decreased by only 0.2 % and 0.3 % for films on $DyScO_3$. Since oxygen vacancies lead to an expansion of the unit cell, a self-adapting variation of the chemical composition at the film-substrate interface is related to a reduction of the lattice stress in case of tensile lattice strain [149]. Thus, formation of vacancies is presumably beneficial for tensile film growth or, conversely, compressively strained films are expected to incorporate oxygen to a greater extent in order to minimize the lattice mismatch.

5.1.3 Improved film stoichiometry by increased Na(O)/Nb ratio in the targets

Increase of the background pressure to more than 0.7 mbar during PLD growth process leads to a transformation of the step-flow growth mode to a 3D-island growth due to the thermalization of the plasma particles. This can indeed be compensated by the use of a significantly higher temperature (900°C), which is, however, not applicable for all substrates (e.g. $NdGaO_3$). Therefore, in the following it was intended to compensate Na- and O-losses during the growth process by the use of Na (O) -excess non-stoichiometric $NaNbO_3$ targets (the results presented in this chapter have been published in [141]).

Sodium enriched targets with a Na/Nb ratio up to 1.37 were applied for the deposition. Although Na enriched targets contain Na_3NbO_4 as foreign phase, in HRXRD patterns of the deposited films, no Na_3NbO_4 contribution has been observed. However, since the incorporation of small Na_3NbO_4 precipitates cannot be excluded (a = 11.126 Å, b = 12.988 Å, c = 5.746 Å [136]), which are suggested to lead to an expansion of the lattice, the determination of the unit-cell

volume of the films is not an adequate indicator for the presence of vacancies in this particular case. For example, no significant difference of the out-of-plane lattice parameters of films on $DyScO_3$ deposited from a stoichiometric target and a target with 1.17 Na/Nb ratio was found (Fig. 5.8). In order to evaluate the effect of the Na/Nb ratio of the used target on the film composition, I have performed EDX measurements. Since it has been shown that for compressively strained films on $SrTiO_3$ substrates the effect of the oxygen pressure has turned out to be more pronounced than for tensilely strained films, the impact of Na (O) -rich targets on the Na/Nb ratio of the $NaNbO_3$ films grown on these substrates has been investigated. Figure 5.9 represents the relative evolution of the Na/Nb ratio in the films derived from EDX measurements in dependence of the Na/Nb ratio in the used target. It is striking that the increase of the Na/Nb ratio in the films is correlated to an incremental Na-excess in the target. Comparison with data from the oxygen partial pressure series, presented in Fig. 5.7, yields that the influence of the target composition on the Na/Nb film ratio is more significant compared to the role of oxygen background pressure. This can be observed from the red triangle in Fig. 5.7, which represents the value for a $NaNbO_3$ thin film grown on $TbScO_3$ at 0.05 mbar from a Na-excess target with a Na/Nb ratio of 1.17.

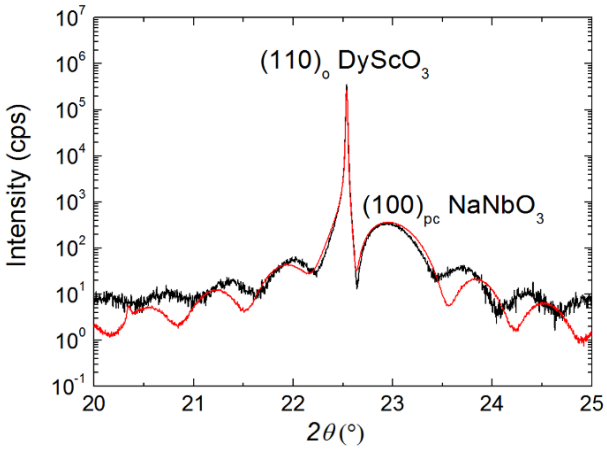

Fig. 5.8: HRXRD *θ-2θ* scan of a $NaNbO_3$ thin films deposited at 600 °C and 0.05 mbar O_2 on $DyScO_3$ substrates using a stoichiometric target (black curve) and a target with 1.17 Na/Nb ratio (red curve).

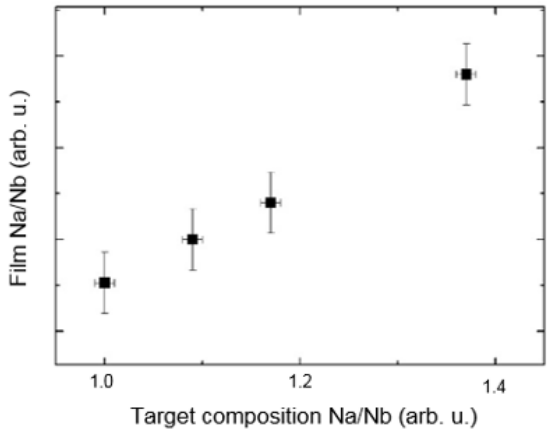

Fig. 5.9: Relative development of the Na/Nb ratio from EDX measurements of $NaNbO_3$ films on $SrTiO_3$ in dependence of Na/Nb ratio in the target.

This effect is attributed to the increased amount of the incorporated extra Na_3NbO_4 phase in the Na-rich targets (see Fig. 4.1 in chapter 4 (Target preparation)). Apparently, Na-deficiency in the films is more effectively reduced by a higher supply of Na_2O at the film surface than by increasing the oxygen background pressure. In this way, the compositional disordering is diminished as long as the Na_3NbO_4 fraction in the target is not too high. For instance, for a target composition with Na/Nb = 1.37, considerable roughening of the film surface was observed (3D-island growth). This is attributed to a significant incorporation of Na_3NbO_4, which is not commensurate with the $NaNbO_3$ host lattice leading to a reduced structural ordering.

5.1.4 Impact of oxygen partial pressure and target composition on the local crystal ordering visualized by HR-TEM and HAADF-HRSTEM measurements

In order to gain more insight into the impact of growth conditions on the structural properties of $NaNbO_3$ films on a microscopic scale, some samples were investigated by HR-TEM and HAADF-HRSTEM. All samples were tensilely strained. Sample A was deposited by the use of a stoichiometric target at low pressure of 0.05 mbar and temperature of 600 °C. The growth conditions of sample B were stoichiometric target, 2 mbar background pressure and 900 °C substrate temperature. Sample C and D were again deposited at low pressure of 0.05 mbar and temperature of 600 °C, but by the use of a Na-excess target with a Na/Nb ratio of 1.17. Sample A and C were grown on $DyScO_3$, sample B on $TbScO_3$ and sample D on $SrTiO_3$ substrates. The different growth conditions including film thickness are summarized in Table 5.4.

In a dark-field image (Fig. 5.10(a)) of sample A, the interface between film and substrate can be seen (white band). In the interface-near region of the film, no defects are visible; however, beyond several nm thickness many dislocations are present. Higher magnification of (a) shows

Table 5.4: Growth conditions and film thickness of the individual samples prepared for TEM investigation.

Sample	Na/Nb target ratio	O_2 pressure (mbar)	Substrate temperature (°C)	Substrate	Film thickness (nm)
A	1	0.05	600	$DyScO_3$	15
B	1	2	900	$TbScO_3$	10
C	1.17	0.05	600	$DyScO_3$	12
D	1.17	0.05	600	$SrTiO_3$	12

that up to a film thickness of 7 nm the sample exhibits a well ordered film structure (Fig. 5.10(b)).

Beyond this thickness, many precipitates with a lateral extent of 1 – 2 nm are clearly visible (marked by a red circle in Fig. 5.10(b)). HRSTEM measurements lead to the conclusion that within the precipitates, Nb atoms are placed in Na columns of the surrounding perovskite material (an example is tagged by the red circle in (c)). Taking into account that at low oxygen pressure during deposition Na and O vacancies are formed (see chapter 5.1.2), it is supposed that these precipitates are formed by a Nb-oxide phase. An incorporation of such a phase into the film would reduce both the Na/Nb and the O/Nb ratio in the film compared to stoichiometric $NaNbO_3$. From Fig. 5.10(a) it is indicated that the interface is not abrupt; a detailed STEM image reveals that rather an intermixing layer is observed (marked by the blue arrows in Fig. 5.10(d)). In this double layer, medium bright contributions are visible in the transition region between bright Dy (Nb) to dark Na (Sc) columns. This observation is explained by a mixed occupation of these positions by heavy Dy (Nb) and light Sc (Na), which is most obvious in the case of Dy on Na positions as Na is too light to be identified in these images at all. This interface intermixing is likely caused by a charge adaptation of mixed NaO^-/DyO^+ and ScO_2^-/NbO_2^+ planes. Thus, the repulsive force between the $(ScO_2)^{1-}$ terminated substrate surface (BO_2) [112] and the initial NaO^{1-} film layer (AO) [150] is reduced. The same observation was made for MOCVD-grown films on $DyScO_3$ as well as $TbScO_3$ substrates (private communication, S. Bin Anooz), which are structurally and chemically very similar to $DyScO_3$, revealing that the interface intermixing does not depend on the deposition technique.

A well-ordered film structure without visible defects in dark-field images (Fig. 5.11(a)) has been observed for sample *B*, a $NaNbO_3$ film grown on $TbScO_3$ substrates at the highest oxygen partial pressure (2 mbar) and 900 °C substrate temperature. On a local scale (Fig. 5.11(b)), no precipitates have been observed. An intermixing layer similar to the one described above was found (Fig. 5.11(c)).

Also, no defects or precipitates were found in HRTEM-measurements at several locations of sample C, $NaNbO_3$ films grown on $DyScO_3$ substrates at low oxygen partial pressure (0.05

mbar) and 600 °C substrate temperature but by the use of a Na (O) -excess target with a Na/Nb ratio of 1.17. One investigated location is exemplarily presented in Fig. 5.12(a) and (b). However, due to the local scale (~15nm), it cannot be excluded that precipitates or other defects are present in the film. A similar high density of precipitates as found in sample A is very unlikely, though. Again, an intermixing layer is clearly visible (Fig. 5.12(b)).

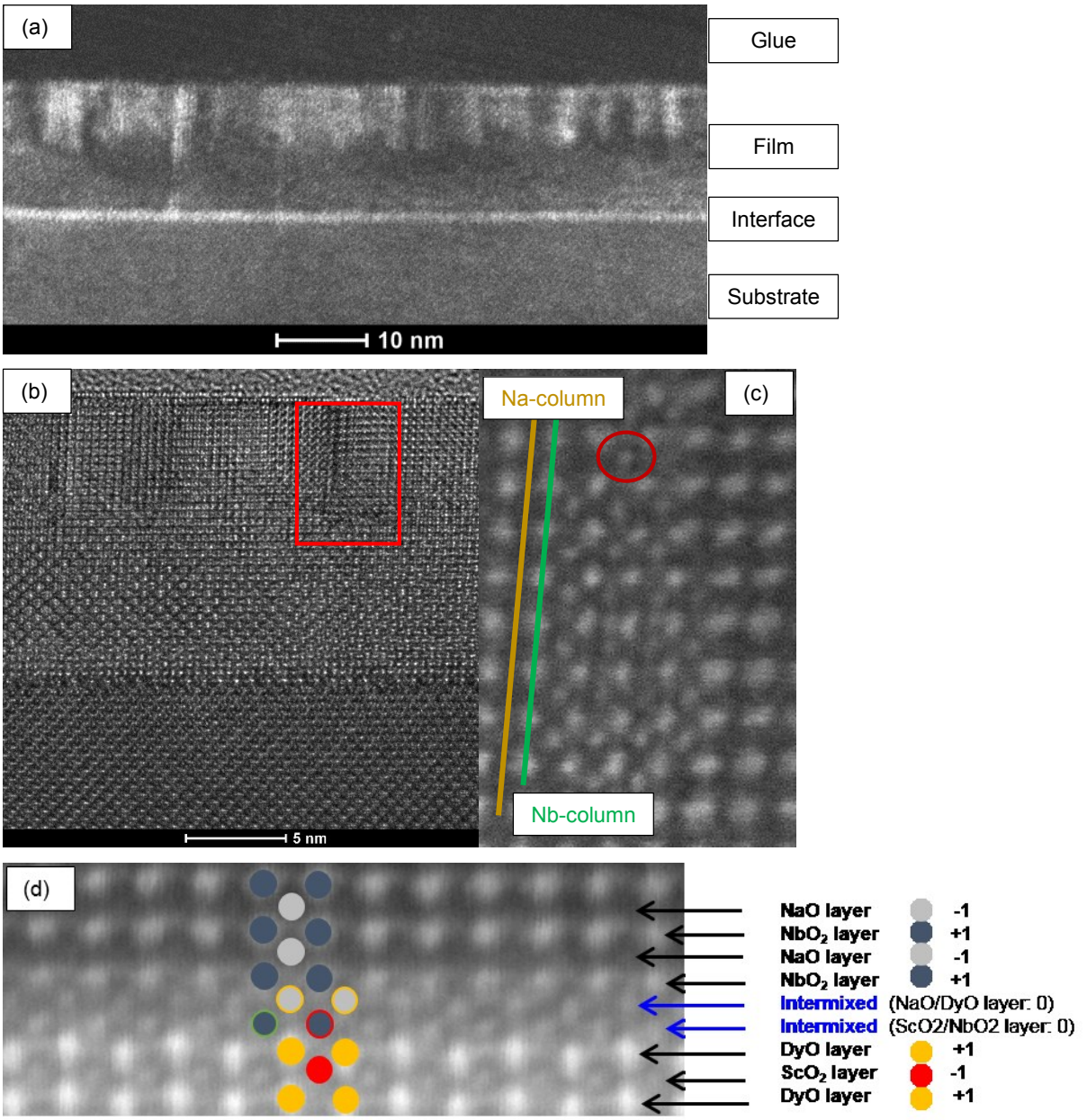

Fig. 5.10: (a) Dark-field TEM image, (b) HRTEM and (c) HAADF-STEM images of sample A. An inclusion of heavier atoms (Nb) in the Na-column can be seen in (c) marked by the red circle. (d) HAADF-STEM of the interface: The positions of the AO and BO_2 planes are marked by arrows.

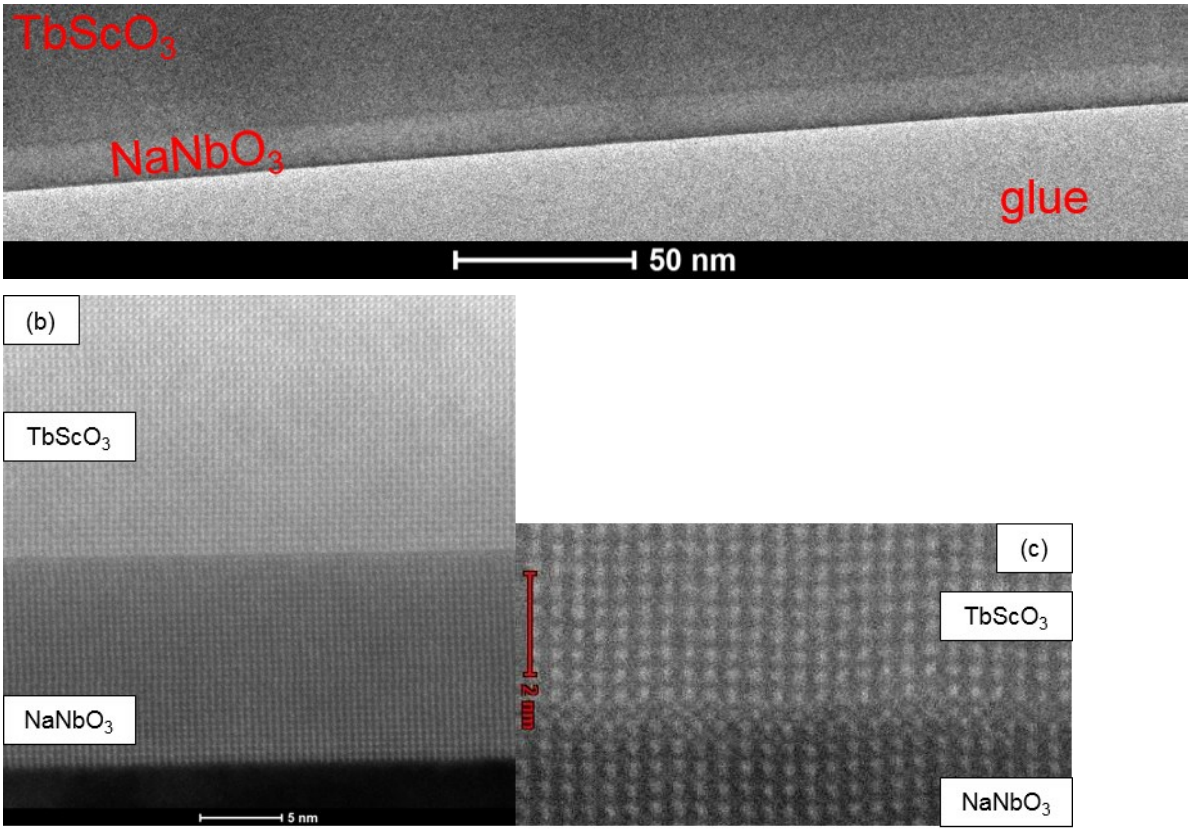

Fig. 5.11: (a) Dark-field TEM and (b) HAADF-STEM image of sample B ($NaNbO_3$ film on $TbScO_3$). No inclusion of heavier atoms (Nb) in the Na-column is visible. No defects were found. (c) HAADF-STEM of the interface: At the interface an intermixing layer is visible similar to Fig. 5.10(c).

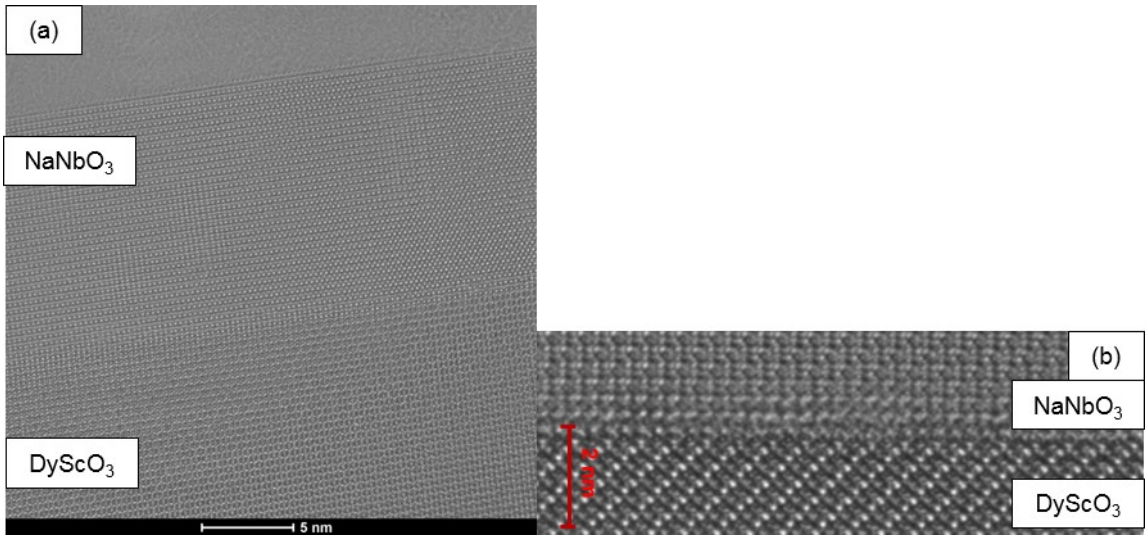

Fig. 5.12: (a) HRTEM image of sample C ($NaNbO_3$ film on $DyScO_3$). No defects were found. (b) HRTEM image of the interface: at the interface, an intermixing layer of ScO and NaO is visible.

For films under tensile strain, it was shown that the use of a Na excess target has a beneficial effect on the structural ordering. The question arises if this is also relevant for compressively strained films. Therefore, HR-TEM and HAADF-STEM measurements have been made on an effectively compressively strained $NaNbO_3$ film on $SrTiO_3$. For this film (sample D), it was attempted to improve the film stoichiometry by the application of a Na(O)-rich target (Na/Nb ratio 1.17) similar to the sample on $DyScO_3$ described above. It was found from HRXRD 2θ-scans that the film lattice is remarkably expanded by ($d_{\perp}$ = 3.95 Å), which cannot be explained only by coherent compressive strained film growth.

In the dark-field TEM image shown in Fig. 5.13(a), it can be seen that columnar defects are present in the film. In contrast to the film described in Fig. 5.10, the columnar defects start to evolve directly at the interface. Zooming in on such a columnar defect in a HAADF-STEM measurement (Fig. 5.13(b)), revealed that again Nb interstitials are present. The observed interstice positioning can be explained by the incorporation of edge-shared NbO_6-octahedra (see Fig. 5.14), which are not present in perovskites. Precursor materials to $NaNbO_3$ that incorporate such edge-shared NbO_6 octahedra include Nb-oxides and Na_3NbO_4, among others [136]. In contrast to the situation on a tensilely strained film, where the Nb-interstices were located at the Na-columns, here the Nb-interstices are located at the O-columns. Thus, the precipitates observed in the compressively strained $NaNbO_3$ film grown under richer Na-conditions are different from the ones in tensilely strained $NaNbO_3$ grown under poorer Na-conditions. Thus, it is proposed that in the former case, more Na is incorporated in vicinity of the precipitates compared to the latter case.

The distance between two Nb ions in edge-shared NbO_6 octahedra is shorter than in the corner-shared ones of $NaNbO_3$. Thus, the incorporation of this type of defect is believed to provide stress relief in compressively strained films, which explains its presence in compressively strained films, opposed to tensilely strained films grown under otherwise identical deposition conditions. It is concluded that in order to achieve near-stoichiometric growth, the deposition conditions of $NaNbO_3$ have to be optimized individually for different employed substrates. For $NaNbO_3$ films on $SrTiO_3$ substrates, optimization of the film stoichiometry is proposed to be more effective when the films are grown under high oxygen background pressure (2 mbar) than by the use of Na-rich targets.

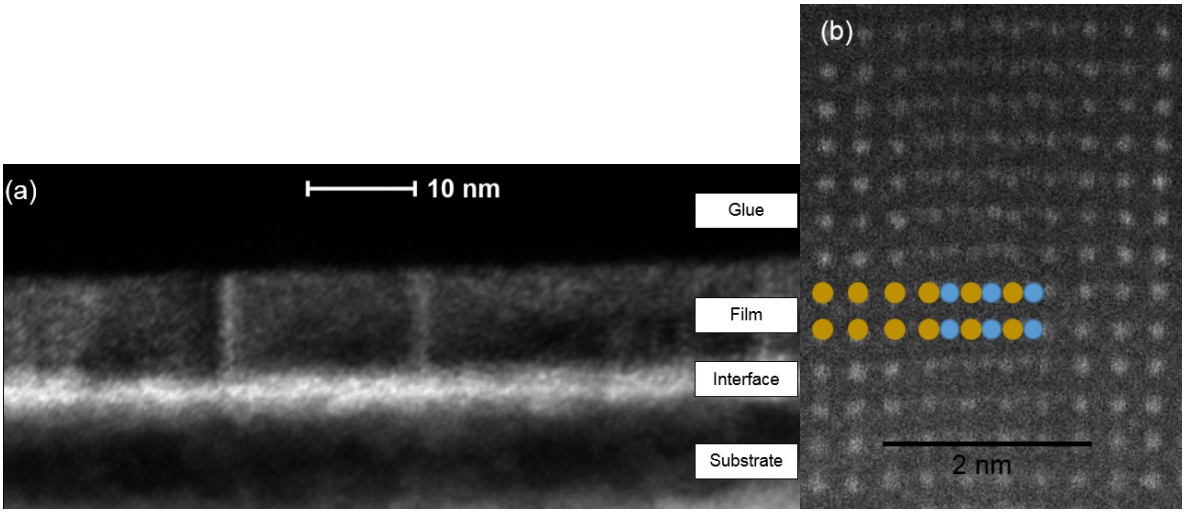

Fig. 5.13: (a) Dark-field TEM image and (b) HAADF-STEM image of sample D. An inclusion of heavier atoms (Nb) in the O-columns can be seen in (b) marked by the blue dots. The gold dots mark the Nb-positions in the perovskite structure.

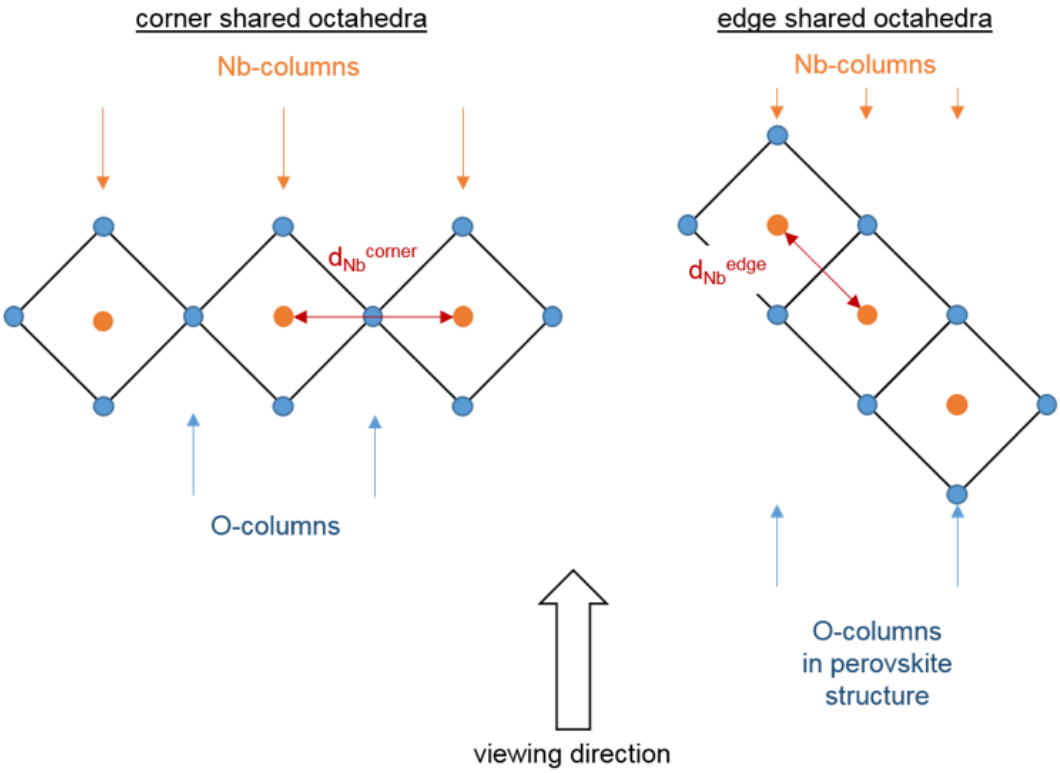

Fig. 5.14: Visualization of the corner shared NbO_6-octahedra in the perovskite structure and the edge shared ones.

5.1.5 Ferroelectric domains of tensilely strained $NaNbO_3$ films on $DyScO_3$ substrates in dependence of deposition conditions

Structural and compositional disordering is suggested to cause the formation of small nanometer-sized domains and domain-wall pinning and may result in degraded ferroelectric properties [139]. A. Duk has shown in his PhD thesis [38] that compressively strained $NaNbO_3$ thin films grown by MOCVD did not exhibit well-ordered domain structures, opposed to tensilely strained ones. Therefore, both piezoelectric amplitude and phase of tensilely strained $NaNbO_3$ films on $DyScO_3$ substrates have been measured by PFM in order to investigate the dependence of ferroelectric domain formation on PLD growth conditions (the results presented in this chapter have been published in [141]). In Fig. 5.15, lateral piezoresponse images of films grown at increasing oxygen partial pressure (a-c) and increased Na/Nb target ratio (d) are shown. LPFM-amplitude measurements revealed that all films exhibit lateral piezoelectric behavior and therefore have at least one polar axis with in-plane components. It is striking, however, that they show significant differences in domain size and arrangement. On films deposited with the use of a stoichiometric target and an oxygen pressure of 0.05 mbar O_2, no distinct domain structure could be detected (Fig. 5.15(a)). The onset of a regular ferroelectric domain formation is visible for films grown at a higher oxygen pressure of 0.7 mbar (Fig. 5.15(b)) and 2 mbar (900 °C) (Fig. 5.15(c)). Significantly more regularly arranged domains were found in the films when a Na (O) -enriched target with Na/Nb = 1.17 was used during deposition (Fig. 5.15(d)). The 1-D stripe domain pattern observed in the latter case is comparable to those observed in similar $NaNbO_3$ films grown by MOCVD [38]. This increase of domain ordering correlates with the increasing Na/Nb ratio in the films from Fig. 5.15(a) to (d) indicated by EDX measurements (Fig. 5.7) as well as the decreasing out-of-plane lattice parameter measured by HRXRD *θ-2θ* scans of the films from Fig. 5.15(a) to (c). However, the

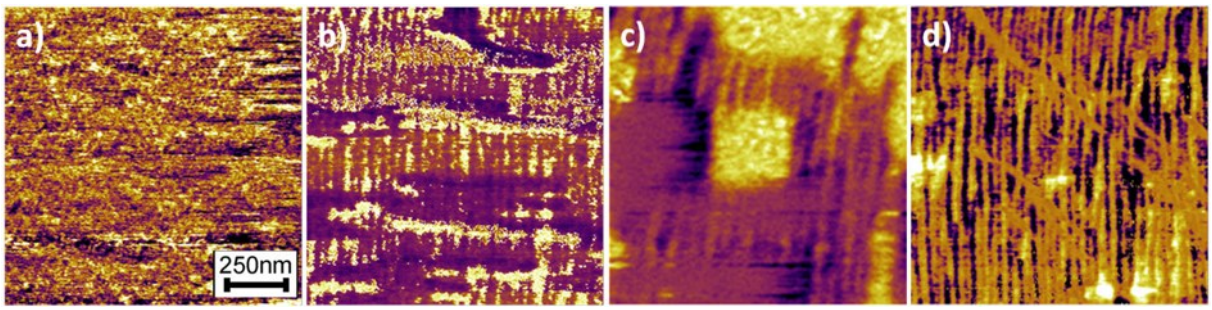

Fig. 5.15: 1 µm² lateral PFM piezoresponse images of ~7 nm $NaNbO_3$ films on $DyScO_3$ substrates. (a) and (b) show films using a stoichiometric target at 600 °C, 0.05 mbar O_2 and 0.7 mbar O_2, respectively, while (c) depicts the piezoresponse image of a $NaNbO_3$ film grown at 900 °C and 2 mbar O_2. The film presented in (d) is grown by the use of a target with Na/Nb ratio of 1.17 at 600 °C and 0.05 mbar O_2.

out-of-plane lattice parameters of the films from Fig. 5.15(a) and (d) are not significantly different. Here, a counteracting effect on the lattice parameter by reduced Na- and O-vacancies, on the one hand, and the marginal incorporation of small Na_3NbO_4 precipitates on the other hand, is assumed. It is concluded that the reduction of Na (O) -vacancies in the films is connected with a decreased number of point defects [26] and enables the formation of regularly arranged ferroelectric domains as a dominant mechanism for reduction of lattice strain and depolarization fields in the ferroelectric $NaNbO_3$ films.

5.2 Dependence of ferroelectric domain formation on the growth rate

The impact of different laser pulse frequencies on structural and ferroelectric properties of $NaNbO_3$ films on $DyScO_3$ was investigated applying the same number of laser shots. The films were deposited at 600 °C substrate temperature, 0.05 mbar oxygen pressure and the use of a target with a Na/Nb ratio of 1.17, which provides films with reduced off-stoichiometry.

Laser pulse frequencies in the range between 1 Hz and 10 Hz have been applied. No influence of the pulse-repetition rate on the surface morphology (Fig. 5.16) or the out-of-plane lattice parameter of the films was found up to a pulse repetition rate of 7 Hz. As the thickness derived from HRXRD measurements (12 nm) was not affected, the deposition rate per time (growth rate) was linearly changed. An increase of the frequency to 10 Hz resulted in the observation of splashes on the surface (Fig. 5.16(d)). This behavior is tentatively explained by the limited size of the target. At high laser-pulse frequencies, rotation and toggling of the target is not sufficient to provide enough time for the molten target surface spots to solidify prior to the next shot, resulting in a different absorption behavior of the target (see chapter 2.1 (PLD)).

The impact of growth rate on the formation of ferroelectric domains is presented for films deposited with 1 Hz, 5 Hz, 7 Hz and 10 Hz pulse-repetition frequencies. The corresponding lateral PFM-phase images of the 2D-grown films scanned along $[001]_o$ are shown in Fig. 5.17. At the low-end side of the pulse repetition scale (1 Hz), a stripe-domain pattern is observed (Fig. 5.17a). Increasing the pulse frequency to 5 Hz yields 1D-stripe domains with significantly improved ordering (Fig. 5.17b). However, upon further increasing the pulse repetition to 7 Hz (Fig. 5.17c) and 10 Hz (Fig. 5.17d), regularly arranged periodic stripe domains in $[001]_o$ direction are no longer formed. A dependence of the domain formation on the growth rate was also recently found for tensilely strained $PbTiO_3$ films on $DyScO_3$ substrates. O. Nesterov et al. [151] have shown that a higher growth rate results in better ordered domains. They concluded that working out of equilibrium conditions (i.e. fast growth rate) is responsible for the higher ordering compared to growth closer to the thermodynamic equilibrium. It has to be remarked, though, that they were investigating a/c domains with horizontally diagonal domain walls. The alternation of these domains requires an alternation of film orientations, opposed to the case of the lateral domain configuration observed in $NaNbO_3$. They proposed that at growth

conditions close to thermodynamic equilibrium, the domain-wall nucleation is dominated by the anisotropic surface cell of the substrate. In contrast, deposition far from equilibrium allowed the domains to minimize the free energy of the system more freely, resulting in more regularly arranged a/c domains. In contrast, MOCVD-grown $NaNbO_3$ films on $DyScO_3$ substrates, deposited significantly closer to the thermodynamic equilibrium compared to PLD-growth, exhibit excellent ordering of the ferroelectric domains [38]. Here, it is assumed that the impact of the 2D substrate-surface symmetry is strong enough to force domain formation into a 1D-stripe pattern (see also chapter 5.5 for more details). In the case of PLD-grown $NaNbO_3$ films, the occurrence of point defects is proposed to have a significant impact on domain formation (see chapter 5.1.5). Deposition at higher growth rates is assumed to result in the incorporation of point defects during growth, due to the higher effective supersaturation. In contrast, in films with highly volatile constituents like Na_2O, extended growth time at high temperatures and low oxygen background-gas is proposed to result in a (slight) increase of point defects (Na and/or O vacancies). The growth rate, which yields the best-ordered domain arrangement thus is assumed to depend crucially on other deposition parameters like substrate temperature and background pressure as well as the surface symmetry of the substrate and the type of domains. In the case of $NaNbO_3$ films on $DyScO_3$ deposited by PLD, the best ordered stripe domains were obtained at a laser-pulse repetition rate of 5 Hz. For that reason, this rate has been used for all films discussed in this work from here on.

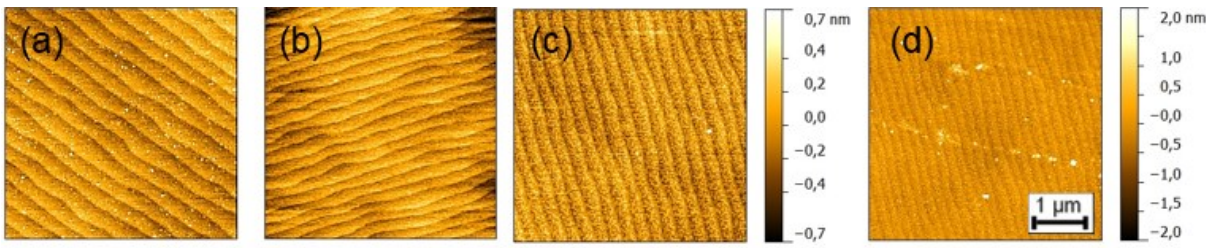

Fig. 5.16: Surface morphology (AFM) of $NaNbO_3$ films deposited at 600 °C and 0.05 mbar O_2 background pressure on $DyScO_3$ substrates with a laser pulse repetition rate of (a) 1 Hz, (b) 5Hz, 7 Hz and (c) 10 Hz. Lateral scale is always 4 µm.

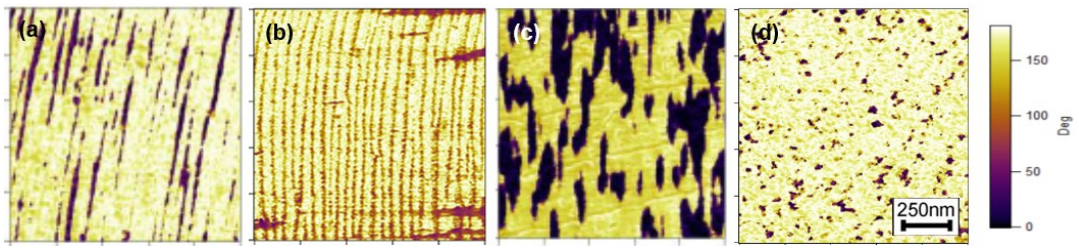

Fig. 5.17: PFM-phase images of 12 nm $NaNbO_3$ films on $DyScO_3$ deposited with a Laser pulse repetition rate of (a) 1 Hz, (b) 5 Hz, (c) 7 Hz and 10 Hz. Lateral scale is always 1 µm.

5.3 Critical thickness in dependence of lattice mismatch

Below the critical thickness, films are coherently grown on the substrate, which means that the in-plane lattice parameters are equal. Above the critical thickness, plastic relaxation leads to changes of the in-plane lattice parameters of the film, which are increasingly different from those of the substrate. In order to illustrate the in-plane parameter dependence on the film thickness, RSM of $NaNbO_3$ films on $NdGaO_3$, $SrTiO_3$, $DyScO_3$ and $TbScO_3$ substrates with film thickness between 3.5 nm and 75 nm have been measured. Since no substantial difference of the film Bragg peaks in vicinity of the $(444)_o$ and $(260)_o$ reflections of the substrates have been observed, only the measurements in vicinity of $(444)_o$ are shown. Films grown on $SrTiO_3$ have been investigated in vicinity of the $(240)_c$ Bragg reflection of the substrate. The growth conditions were chosen with regard to optimized film stoichiometry and the functional aspects such as ferroelectric domain formation and local hysteresis on the different substrates. Films on $NdGaO_3$ ($DyScO_3$) were deposited from targets with a Na/Nb ratio of 1.09 (1.17) at an oxygen background pressure of 0.7 mbar (0.05 mbar). On $SrTiO_3$ and $TbScO_3$, the films were deposited from a stoichiometric target at 2 mbar oxygen background pressure. On all substrates other than $NdGaO_3$, 2D growth was achieved for all films presented here even to film thicknesses well beyond the critical thickness for the onset of plastic relaxation. In the case of $NdGaO_3$, up to 25 nm thick films retained 2D growth, while for 30 nm thick films a transition to 3D-island growth took place.

Compressively strained $NaNbO_3$ films on $NdGaO_3$ substrates with thicknesses of 15 nm show no sign of relaxation (Fig. 5.18(a)). The map of the 20 nm film (Fig. 5.18(b)) shows asymmetric diffuse scattering in the direction of bulk $NaNbO_3$, caused by the onset of plastic relaxation. The 30 nm thick film (Fig. 5.18(c)) experiences increased plastic lattice relaxation resulting in the shift of the film peak to the bulk $(402)_c$ reflection of c_c-oriented pseudocubic $NaNbO_3$. Thus, the critical thickness for plastic lattice relaxation of $NaNbO_3$ thin films on $NdGaO_3$ substrates is estimated to be about 20 nm.

Anisotropically strained $NaNbO_3$ films with a small average lattice mismatch on $SrTiO_3$ were found to grow fully strained to a thickness of at least 42 nm.

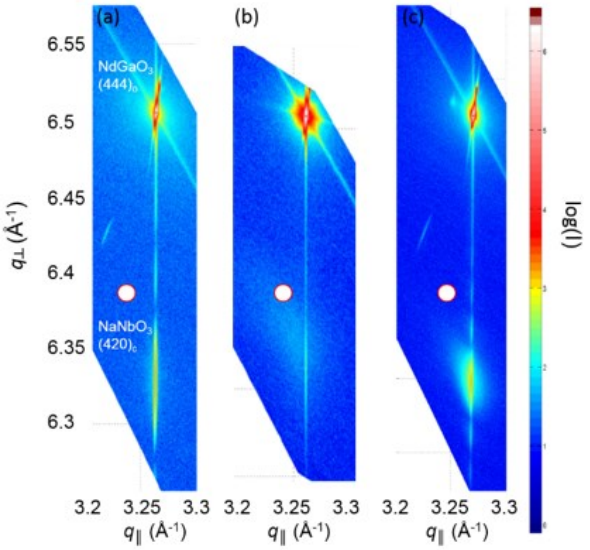

Fig. 5.18: X-ray reciprocal space maps of $NaNbO_3$ with film thicknesses of (a) 15 nm, (b) 20 nm and (c) 28 nm in vicinity of the $(444)_o$ Bragg reflection of the $NdGaO_3$ substrate. The $(420)_c$ Bragg reflection of bulk $NaNbO_3$ is marked as open circle.

For tensilely strained $NaNbO_3$ films on $DyScO_3$, the critical thickness for the onset of plastic relaxation is about 27 nm. In Fig. 5.19, RSMs of the $(402)_c$ $NaNbO_3$ and $(444)_o$ $DyScO_3$ Bragg reflections are exemplarily shown for films with thicknesses of 3.5 nm (a), 27.3 nm (b) and 49.0 nm (c), respectively. The film with a thickness of 49.0 nm is clearly partially relaxed, illustrated by the strong asymmetric broadening of the film peak in the direction of bulk a_c- oriented $NaNbO_3$ indicated by the white circle in Fig. 5.19(c).

For MOCVD-grown $NaNbO_3$ films on $TbScO_3$ [23], a critical thickness of about 20 nm was identified. Reciprocal space maps of the $(402)_c$ $NaNbO_3$ and $(444)_o$ $DyScO_3$ Bragg reflections of PLD-grown films with thicknesses of (a) 10 nm, (b) 35 nm and (c) 58 nm are shown in Fig. 5.20. While for films with thickness below 20 nm (a) no signs of relaxation are visible, the asymmetric broadening of the film peak in the direction of the bulk value for films with thicknesses above 20 nm (b and c) clearly indicates plastic lattice relaxation. Since the results from PLD-grown and MOCVD-grown films agree well with each other, I assume that the critical thickness of 20 nm observed for the latter deposition method is also reasonably applicable for PLD.

The critical thickness of $NaNbO_3$ films in dependence of lattice mismatch is presented in Fig. 5.21. The general trend is in good agreement with the phenomenological equation (1.8) for the critical thickness as discussed in chapter 1.3 (Epitaxy), resulting in a value of 0.02(1±2) for the empirical factor A^*. This is in good qualitative agreement with $BaTiO_3$ films on $SrTiO_3$ substrates published by T. Suzuki et al. [152], where the critical thickness was found to be about 5 nm. With an average lattice mismatch of 2.8% between $BaTiO_3$ and $SrTiO_3$, this results in A^* = 0.023.

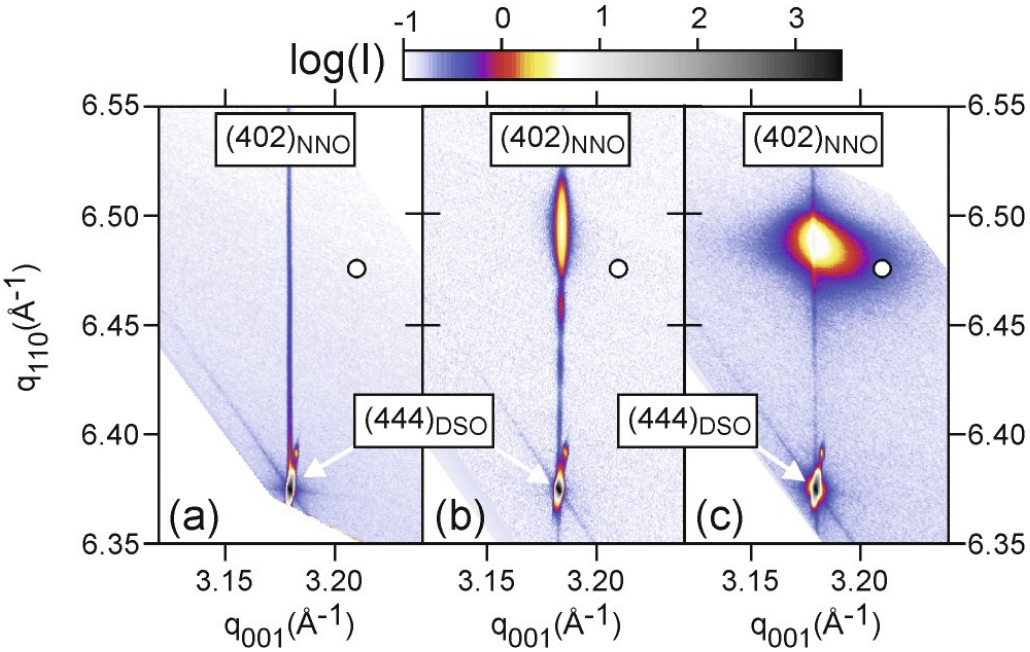

Fig. 5.19: X-ray reciprocal space maps of $NaNbO_3$ with film thicknesses of (a) 3.5 nm, (b) 27.3 nm and (c) 49.0 nm in vicinity of the $(444)_o$ Bragg reflection of the $DyScO_3$ substrate. The $(402)_c$ Bragg reflection of bulk $NaNbO_3$ is marked as open circle. Adapted from [43].

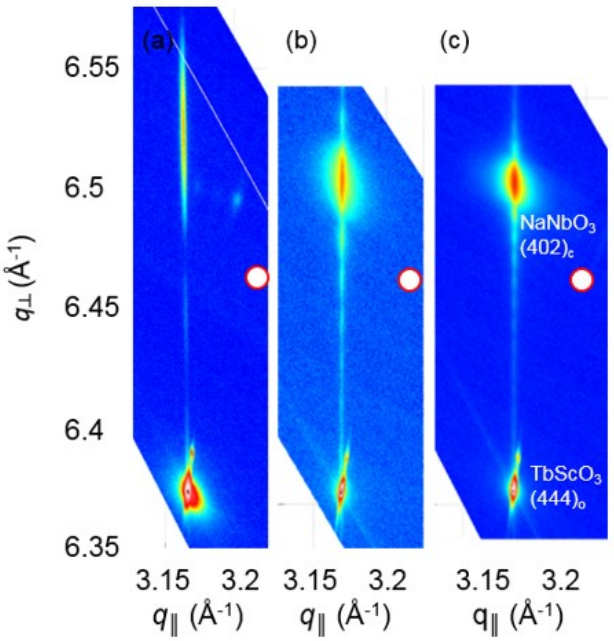

Fig. 5.20: X-ray reciprocal space maps of $NaNbO_3$ with film thicknesses of (a) a 10 nm, (b) a 36 nm and (c) a 59 nm in vicinity of the $(444)_o$ Bragg reflection of the $TbScO_3$ substrate. The $(402)_c$ Bragg reflection of bulk $NaNbO_3$ is marked as open circle.

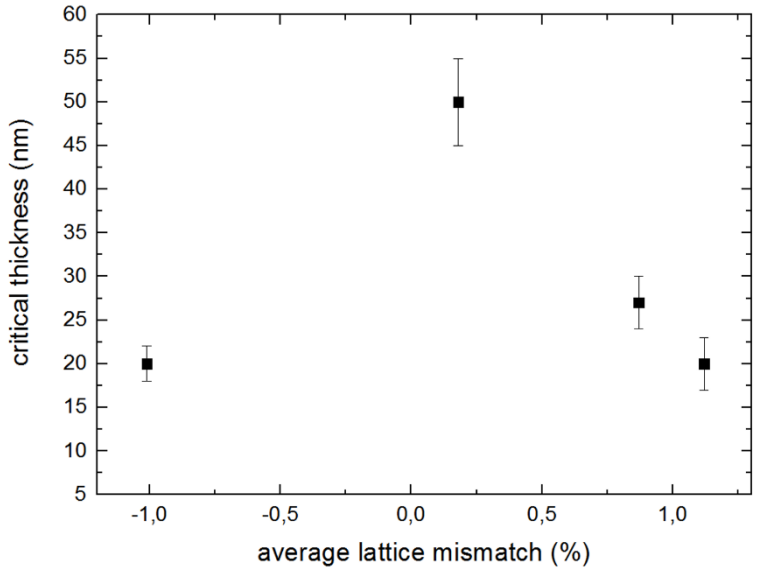

Fig. 5.21: Critical thickness for the onset of plastic relaxation of $NaNbO_3$ films in dependence of average lattice mismatch with the substrate.

5.4 Dependence of the out-of-plane lattice parameter on film thickness below the critical thickness

For fully strained films, no dependence of the vertical lattice parameters on the film thickness is expected. In contrast, experimentally, such a dependence was found for tensilely and compressively strained $NaNbO_3$ films with thicknesses below the critical thickness for the onset of plastic lattice relaxation (t_{crit}). For a more detailed investigation, $NaNbO_3$ thin films with film thicknesses between 3 nm and 75 nm were grown on $NdGaO_3$ and $DyScO_3$. For $NaNbO_3$ films on $NdGaO_3$ ($DyScO_3$) substrates, the lattice parameters as measured by HRXRD decreased (increased) with increasing film thickness. Figure 5.22 illustrates the respective trends. As for $t < t_{crit}$, the in-plane parameters of fully strained films on the same substrate are identical, this results in significant differences of the unit-cell volume.

It was investigated, whether it is possible to explain the observed behavior by surface or interface effects, which would have a more pronounced effect on the vertical lattice parameters in thin film compared to thicker ones. Simulations (RCRefSimW, Peter Zaumweil) of the expected XRD pattern of two different samples with identical total film thickness are presented in Fig. 5.23(a) in comparison with an experimental curve. One sample consists of one single film, while the other is made up of a very thin film at the interface to the substrate and a thicker “bulk” layer (Fig. 5.23(b)). The ratio between the thicknesses of the thin layer and the “bulk” layer is 0.2. The average vertical lattice parameter of the two-component sample is

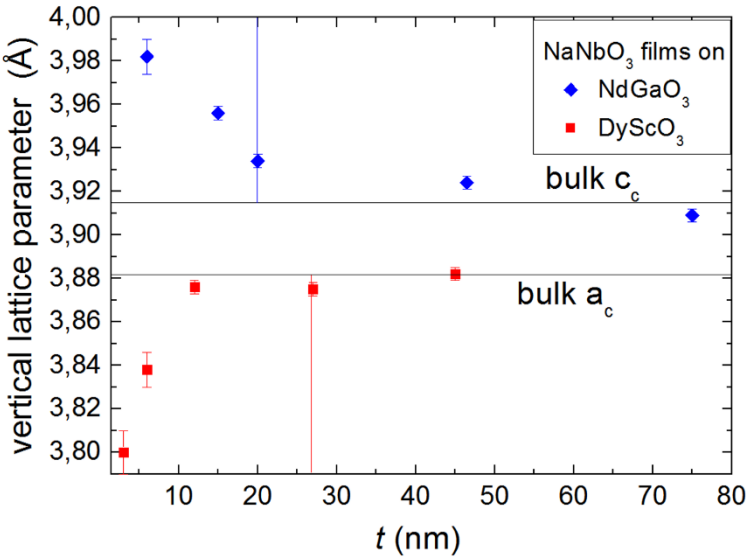

Fig. 5.22: Vertical lattice parameter of $NaNbO_3$ films in dependence of the film thickness on $DyScO_3$ (red circles) and $NdGaO_3$ (blue circles) substrates. The onset of plastic relaxation on the different substrates is indicated by the vertical lines.

equal to the vertical lattice parameter of the single film. From Fig. 5.23(a) it can be seen that it is not possible to distinguish between the film-peak positions of the two, both agreeing very well with the experimental one. Thus, if both the average vertical lattice parameter and the total thickness of the two samples are the same, equal simulated curves are obtained regardless of the precise composition of the samples. The example shown here (on $DyScO_3$), has an overall film thickness of 27 nm and serves as an illustration of the described behavior. In contrast to experimental data, simulations of smaller films resulted in film-peak and thickness-oscillation intensities, which were too low to analyze.

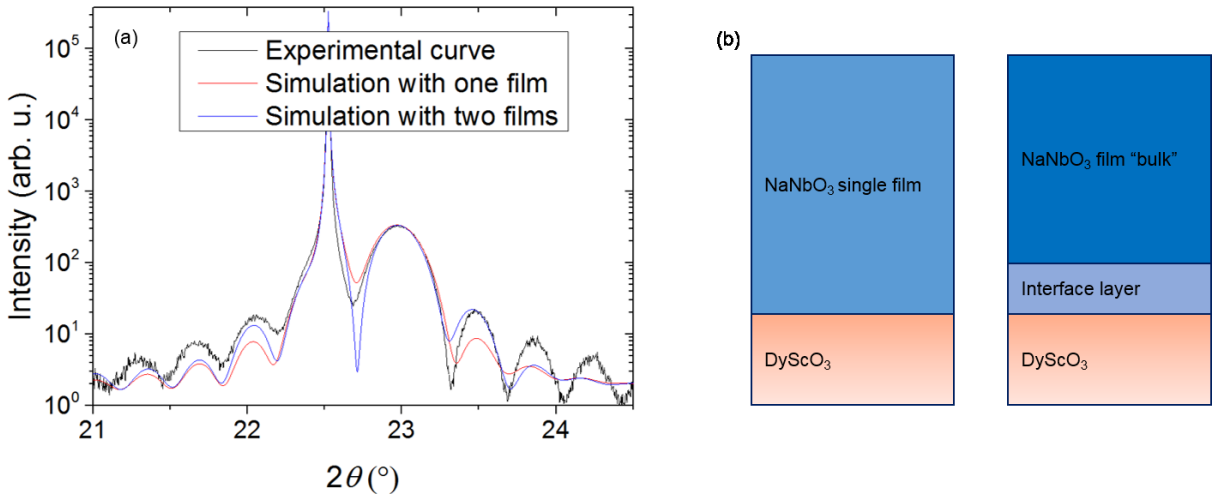

Fig. 5.23: (a) Comparison of an experimental curve of $NaNbO_3$ on $DyScO_3$ and two simulated curves using one or two differently strained layers. The different makeup of the systems is visualized in (b).

The thinnest films deposited on both $NdGaO_3$ and $DyScO_3$ substrates have a thickness of about 6 nm (~ 16 monolayer (ML)). The film "bulk" layer (interface layer) consisting of 13 ML (3 ML) have the same ratio as the one used for the simulation described in Fig. 5.23(a). The vertical lattice parameters of films with different film thicknesses on the same substrates have thus been calculated, taking the weighted average of the 3 ML-interface layer and the remaining (film thickness – 3ML) film. For the "bulk film", vertical lattice parameters equal to the experimentally derived ones close to the critical thickness have been used (3.88 Å on $DyScO_3$, 3.93 Å on $NdGaO_3$). Good agreement between the calculated and experimentally derived $d_\perp$ values was obtained for films on $DyScO_3$, if a vertical lattice parameter of 3.73 Å was used for the 3 ML-interface film.

It was shown that an intermixing layer is present in $NaNbO_3$ films on $DyScO_3$ substrates. Under certain circumstances, the intermixing layer can exhibit reduced lattice parameters compared to $NaNbO_3$. These circumstances are (i) the intermixing of Dy^{4+} instead of Dy^{3+} with Na^+ and (ii) the intermixing of Nb^{4+} instead of Nb^{5+} with Sc^{3+}. Condition (i) is expected to result in smaller lattice parameters since the ionic radius of Dy^{4+} is significantly smaller than that of Na^+ and Dy^{3+}. Condition (ii) retains charge neutrality at the interface, while their respective ionic radii are almost the same. Both the transformation of Dy^{3+} to Dy^{4+} and of Nb^{5+} to Nb^{4+} is possible in $DyScO_3$ and $NaNbO_3$, when O-vacancies are present in the materials. In $DyScO_3$ substrates, that is the case [114]. In addition, $NaNbO_3$ films deposited at an oxygen background pressure of 0.05 mbar are also expected to exhibit O-vacancies. In order to clarify this assumption it would be necessary to perform TEM-EDX or TEM-XPS (X-ray photoelectron spectroscopy) measurements, which were not available.

No such behavior was found for $NaNbO_3$ films on $NdGaO_3$ substrates [38], which agrees with the finding that no good agreement between the calculated and experimentally derived $d_\perp$ values was obtained for films on $NdGaO_3$. Furthermore, even an intermixing of Ga^+ (which has a significantly larger ionic radius than Ga^{3+}) with Na^+ is not expected to result in increased lattice parameters compared to $NaNbO_3$. At this time, it can only be speculated that a repulsive force due to the similarly charged sublayers at the interface (NbO_2^+/GaO^+) results in increased lattice parameters close to the interface. In contrast, such a repulsive force is not expected in the case of the intermixed interface of $NaNbO_3/DyScO_3$ (see chapter 5.1.4).

5.5 Thickness dependence of the monoclinic in-plane distortion and ferroelectric domains of $NaNbO_3$ films on $DyScO_3$

Tensilely strained $NaNbO_3$ films, grown under optimized conditions regarding the film stoichiometry, exhibit well-ordered ferroelectric domain configurations not reported on other materials. They are therefore well suited for the investigation of the ferroelectric domain structure in dependence of film thickness and the related variation of the strain state. In contrast, compressively strained films grown by MOCVD were found to exhibit no domain structure visible by PFM [38].

5.5.1 Monoclinic domains and distortion angle

This section will concentrate on the dependence of the structural properties of $NaNbO_3$ on the film thickness when deposited on $DyScO_3$ substrates (the results presented in this chapter have in part been published in [43]). Bulk $NaNbO_3$ exhibits a monoclinic distortion angle $\beta_c = \alpha_c - 90° = 0.67°$ between the b_c- and c_c-directions (Fig. 5.24). In the case of a_c-oriented $NaNbO_3$ films on $DyScO_3$, this relates to an in-plane angle. For the verification of how a monoclinically distorted film unit cell matches the almost quadratic unit cell of the $DyScO_3$ substrate, a series of films with thickness between 1.5 – 49 nm was deposited by PLD. The growth parameters were 0.05 mbar oxygen pressure, 600 °C substrate temperature and Na/Nb target ratio of 1.17. An additional film with 130 nm thickness deposited by MOCVD was investigated since no sample of this thickness was available at the allotted beam time for GIXD measurements at BESSY. As stated in chapter 2.5 (XRD), X-ray sources with high beam intensities such as synchrotron radiation are necessary for these measurements in order to achieve a satisfactory signal-to-noise ratio. The in-plane lattice parameters and monoclinic angles of $NaNbO_3$ films on $DyScO_3$ substrates were determined by XRD reciprocal space maps and grazing incidence XRD, respectively.

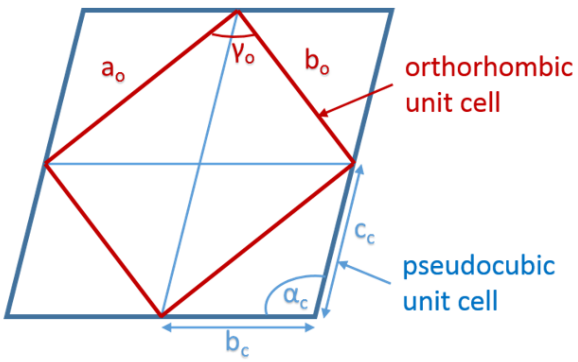

Fig. 5.24: Schematic illustration of the monoclinic nature of the pseudocubic unit cell. Adapted from [111].

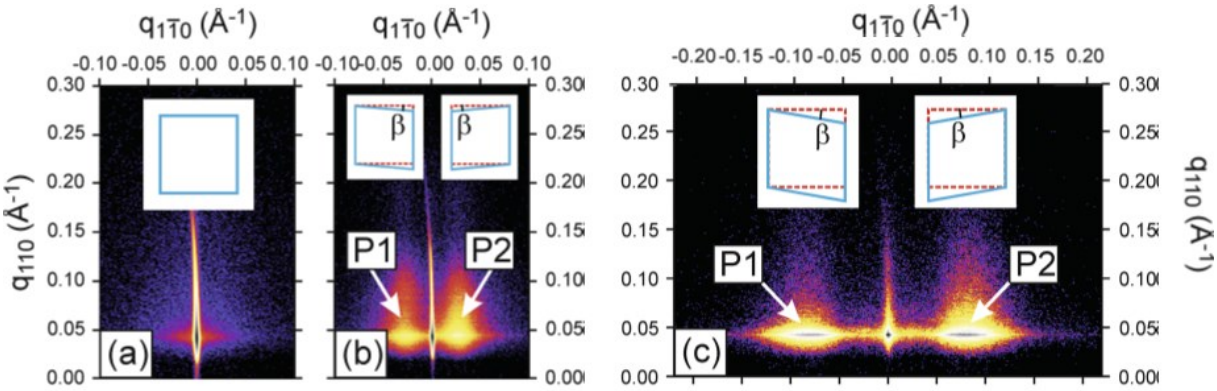

Fig. 5.25: GIXD intensity distributions of (a) 1.5 nm, (b) 6.0 nm, and (c) 27.3 nm $NaNbO_3$ films in the vicinity of the $(008)_o$ $DyScO_3$ reciprocal lattice point. *P1* and *P2* mark two satellite peaks arising from adjacent $NaNbO_3$ domains. The insets illustrate the in-plane unit cells of $NaNbO_3$ domains (blue solid line) and $DyScO_3$ (red dashed line). Taken from [43].

In the following, two-dimensional sections of the intensity distributions of GIXD scans in vicinity of the in-plane $(008)_o$ $DyScO_3$ reciprocal lattice point will be discussed. For films with a thickness of 1.5 nm, only a sharp crystal truncation rod at $q_{1\text{-}10} = 0$ caused by the smooth sample surface and film/substrate interface can be seen (Fig. 5.25(a)). Films with a thickness of at least 6.0 nm (Fig. 5.25(b)) exhibit two satellite peaks (P_1 and P_2) next to the crystal truncation rod. A careful analysis on different in-plane Bragg reflections reveals that P_1 and P_2 are caused by an alternating in-plane tilting of the lattice planes of adjacent domains with respect to the $DyScO_3$ $[1\text{-}10]_o$ substrate direction, while the $NaNbO_3$ crystal remains coherent at the domain walls (Fig. 5.26). The angular spacing of the satellites of the film with a thickness of 27.3 nm is increased, compared to the one with 6.0 nm film thickness.

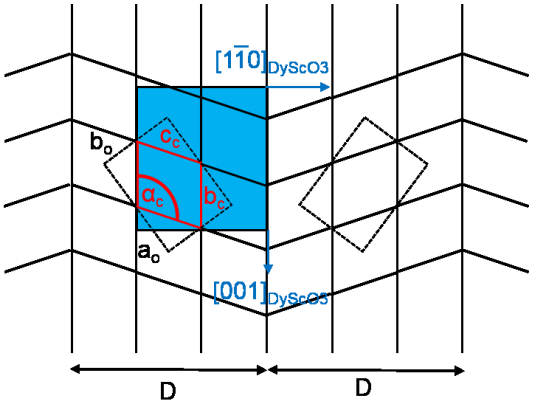

Fig. 5.26: Schematic view of the in-plane monoclinic domain structure. The red rhombus represents the monoclinic unit cell of $NaNbO_3$ with the monoclinic distortion angle α_c. The dotted rectangles depict the in-plane lattice of orthorhombic $NaNbO_3$. The blue area displays the nearly squared in-plane lattice of the (110) $DyScO_3$ substrate. The lateral adjacent domains with size *D* shown differ by a 90° in-plane rotation. Adapted from [23].

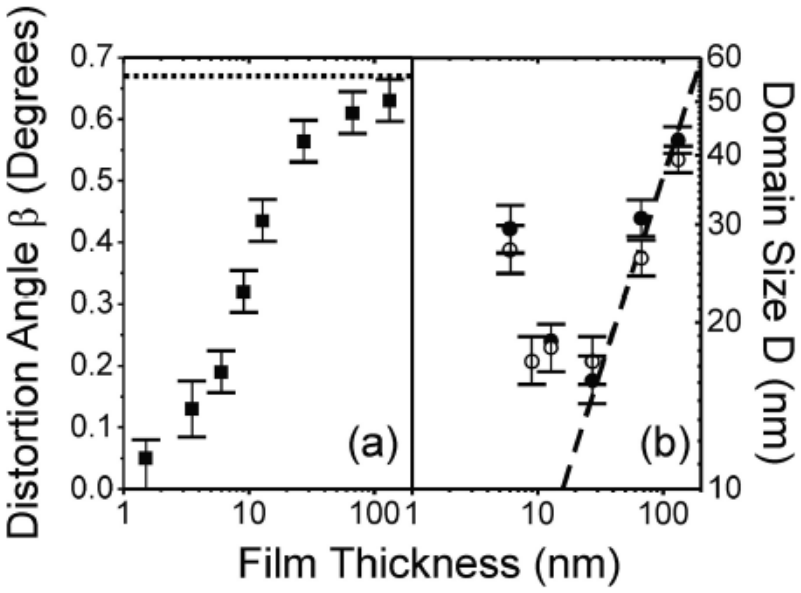

Fig. 5.27: (a) Monoclinic distortion angle β and (b) lateral domain size *D* deduced from GIXD as a function of film thickness. The horizontal dotted line represents the bulk $NaNbO_3$ monoclinic distortion angle β = 0.67° [116]. The dashed line describes the square-root dependence of the domain size on film thickness predicted by Pertsev et al. [46]. Taken from [43].

From the angular spacing, the monoclinic angle *β* can be determined within an error range of ±0.05°.

Furthermore, the domain width *D* can be calculated from the in-plane full widths at half-maximum *δq* of the satellites peaks:

$$D = \frac{2\pi K}{\delta q}. \quad (5.1)$$

In the case of rectangular domains with vertical domain walls, K = 0.885. Monoclinic angle and domain size in dependence of film thickness are shown in Fig. 5.27(a) and (b), respectively.

The unit cell of very small films fits to that of the substrate with a nearly squared in-plane lattice (β < 0.05°). With increasing thickness, a monoclinic distortion occurs (Fig. 5.27(a)), which increases with increasing thickness. This elastic relaxation starts at film thicknesses below the critical thickness for plastic relaxation (~27 nm, see chapter 5.3) and approaches the bulk value of 0.67° only at a film thickness of 130 nm. Together with the relaxation of the in-plane lattice parameter with increasing film thickness, an overlapping of the two relaxation processes is observed for films with thicknesses above the critical thickness. For $NaNbO_3$ films on $TbScO_3$ substrates grown by MOCVD, a two-step relaxation process was found [23], where the two contributions take place successively rather than simultaneously. The different behavior is tentatively explained by the higher lattice mismatch of the $NaNbO_3$ films and $TbScO_3$ compared to $DyScO_3$ substrates.

An evaluation of the domain size in relation to the film thickness (Fig. 5.27 (b)) reveals that the square-root dependence of the Kittel law [48] is fulfilled only for films with a minimum thickness of about 27 nm. A minimum of the domain size of about 16 nm was identified between 10 nm and 30 nm film thickness. The domain size significantly increases when decreasing the film thickness to 6 nm. No domains could be identified for even thinner films. Pompe et al. [153] as well as Pertsev and Zembilgotov [46] have predicted that elastic interactions between domains and substrate can lead to an increase of domain size for very thin films where the elastic interactions take place over distances exceeding the film thickness.

For films with thicknesses up to about 13 nm no satellite peaks were observed in vicinity of $(2\text{-}20)_o$, which means that the domain walls run exclusively along the $[001]_{DSO}$ direction. This behavior is not necessarily expected, since the nearly squared in-plane lattice of $DyScO_3$ is almost isotropic regarding the lattice parameters. Thus, no preferential lattice domain orientation should be induced by the substrate. A closer look at the atomic positions at the $(110)_o$ surface of $DyScO_3$ reveals that the Dy atoms are differently aligned along $[1\text{-}10]_o$ and $[001]_o$. While in the former case the Dy atoms are lined up in straight rows, a zig-zag formation is found for the latter (Fig. 5.28). Thus, the symmetry of the surface unit cell is 2-fold rather than 4-fold, inducing a preferential direction for the domains, similar to the $TbScO_3$ $(110)_o$ surface described in detail by A. Duk [38].

The domain width of $NaNbO_3$ films on $TbScO_3$ substrates grown by MOCVD was also found to depend on the film thickness [23], although in this case no minimum domain width was observed. However, the smallest film thickness was 7 nm in this case. It is conceivable that the minimum of the domain size is shifted to smaller film thickness, as the lattice mismatch between $NaNbO_3$ and $TbScO_3$ is larger (see chapter 3 (Materials)).

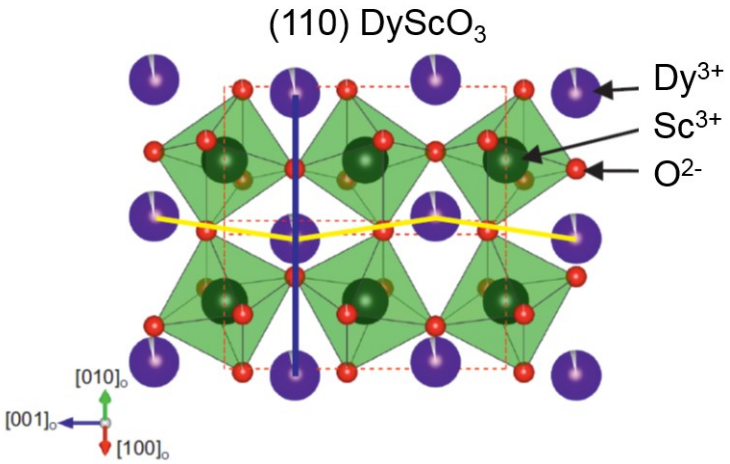

Fig. 5.28: (110) surface of $DyScO_3$. The red dashed line marks the orthorhombic unit cell boundaries. Adapted from [38].

5.5.2 Ferroelectric domains

All films have been investigated regarding their lateral and vertical polarization direction. In the case of lateral-PFM (LPFM) measurements, two scan directions were nominally chosen, along the $[001]_o$ and $[1\text{-}10]_o$ directions of the $DyScO_3$ substrates, rotated by 90° with respect to each other (the results presented in this chapter have in part been published in [43]).

PFM phase images of the films are shown in Fig. 5.29 up to a maximum thickness of 27.5 nm. On all films, a piezoelectric response in both lateral and the vertical direction was measured. However, the VPFM amplitude of up to 12 nm thick films and the LPFM amplitude of the film with 1.5 nm thickness is below 30 pm, which is attributed to noise. For this reason, we assume that no actual vertical polarization direction is present in the films. This is distinctly different in the case of thicker films ($t \geq 27.3$ nm) where a significant out-of-plane piezoelectric signal was detected. Furthermore, in this case vertical stripe domains are visible (Fig. 5.29(e)).

Very thin films ($t \leq 3$ nm) exhibit no visible domain pattern. Furthermore, they do not exhibit piezoelectric response apart from noise. The nearly squared surface cell is assumed to suppress the formation of a polar in-plane axis. In the case of slightly thicker films (6 to 13 nm), periodic 1-D lateral stripe domains were found, if the scan direction was along $[1\text{-}10]_o$, whereas no domain pattern was visible while scanning along $[001]_o$. This means that the 1D-stripe domains are aligned along the $[001]_o$ direction, perpendicular to the scan direction. From this behavior, a periodic stripe pattern of the type $a_1/a_2/a_1/a_2$ is deduced [43].

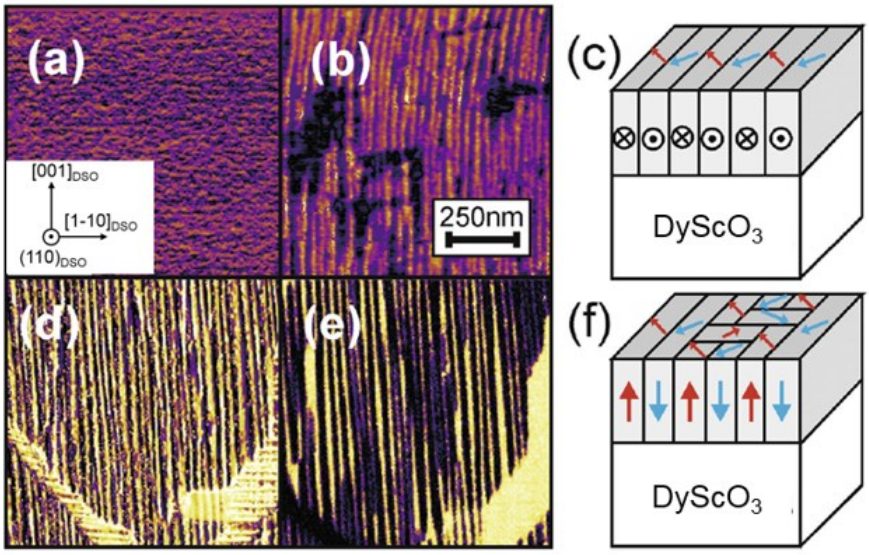

Fig. 5.29: Lateral (LPFM) and vertical (VPFM) PFM-phase images of $NaNbO_3$ films with thicknesses of (a) 1.5 nm (LPFM), (b) 6.0 nm (LPFM) and (d), (e) 27.3 nm (LPFM, VPFM) grown on $(110)_o$ $DyScO_3$ substrates along with schemes of the ferroelectric domain structure (c), (f) [43].

Increasing the thickness further to 27.3 nm yields the formation of a 2D-stripe pattern with contributions along the $[1\text{-}10]_o$ direction as well. This behavior is attributed to a diminished effect from the substrate/film interface. Furthermore, the onset of plastic lattice relaxation results in a slightly diminished tensile strain leading to the evolution of a significant vertical polarization component. The resulting domain formation of this film is tentatively explained by the coexistence of a_1, a_2 and c domains. This is in qualitative agreement with a theoretical study for $PbTiO_3$ films grown under reduced tensile strain [45].

PFM domain-sizes fit to the GIXD results indicating that inhomogeneous peak broadening caused by structural defects or a non-uniform domain size can be neglected.

5.6 Domain formation of partially relaxed $NaNbO_3$ films on $TbScO_3$ substrates

Several samples with reduced in-plane strain have been grown in order to examine the ferroelectric domain formation of partially relaxed films. A variation in the effective in-plan lattice strain (e.g. reduced strain due to the incorporation of misfit dislocations) is predicted to have a marked impact on the orientation of the polarization direction. This behavior is well investigated for bulk tetragonal materials [154] but only limited experiments have been made in that regard for bulk orthorhombic materials like $NaNbO_3$ [155].

Films with thicknesses in the range of 35 - 65 nm (above the critical thickness for the onset of partial lattice relaxation (~20 nm)) exhibit almost identical vertical lattice parameters ($d_\perp$ = 3.85(3±1) Å) regardless of the film thickness. The observation of constant $d_\perp$ indicates that after an initial relaxation via the incorporation of misfit dislocations, films in the thickness range between 35-65 nm do not exhibit increased relaxation with increased film thickness. A possible explanation is that ferroelastic 90° domains provide the necessary strain relief [46]. In all cases, the value of $d_\perp$ is significantly below the value for a_c-oriented bulk $NaNbO_3$, indicating tensile strain.

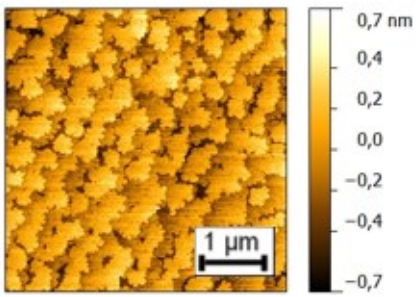

Fig. 5.30: Surface morphology (AFM) of a 65 nm thick $NaNbO_3$ film deposited on a $TbScO_3$ substrate.

Thin $NaNbO_3$ films on $TbScO_3$ deposited at 900°C substrate temperature and 2 mbar oxygen pressure were found to exhibit very well ordered crystal structures even at the nanoscale (see chapter 5.1.2 and 5.1.4). All films were grown in 2D-growth mode. An AFM image of a 65 nm thick film is shown in Fig. 5.30.

In order to gain additional information about the in-plane structure of the films, GIXD measurements were performed. Exemplarily, the film with a thickness of 59 nm was investigated by GIXD. For that purpose, angular scans of symmetric Bragg reflections in two azimuthal positions were recorded, whereby the incidence beam is directed either along the $[1\text{-}10]_o$ or the $[001]_o$ direction of the substrate. The results are shown in Fig. 5.31. Corresponding to chapter 5.5.1, the occurrence of two satellite peaks was explained by a monoclinic in-plane distortion. In both azimuthal positions the in-plane monoclinic distortion angle is close to the bulk value of 0.67° both along the $[001]_o$ (β = 0.6(4±3)°) and $[1\text{-}10]_o$ (β = 0.6(0±5)°) directions. This indicates that the film exhibits two types of monoclinic distorted domains rotated by 90°. However, the signal from domains arranged along $[1\text{-}10]_o$ is much weaker, which suggests that only a small fraction of the in-plane domain walls are aligned along this direction. Compared to RT, the $TbScO_3$ substrates exhibit a larger anisotropy of the in-plane lattice parameters ($(a_c+b_c)/a_c$ ~ 0.2 %) at the growth temperature, with a larger lattice mismatch between film and substrate along $[001]_o$. Thus, ferroelastic domain walls along this direction reduce in-plane lattice stress more effectively than along $[01\text{-}1]_o$. Together with the 2-fold symmetry of the substrate surface, a preferential arrangement of the monoclinically distorted domains is therefore expected. This behavior is similar to tetragonal $Pb_{0.9}Zr_{0.1}TiO_3$ under tensile lattice strain on $SmScO_3$ [156], where also a preferential orientation of ferroelastic domains was found along $[001]_o$, the direction with larger lattice mismatch between substrate and film.

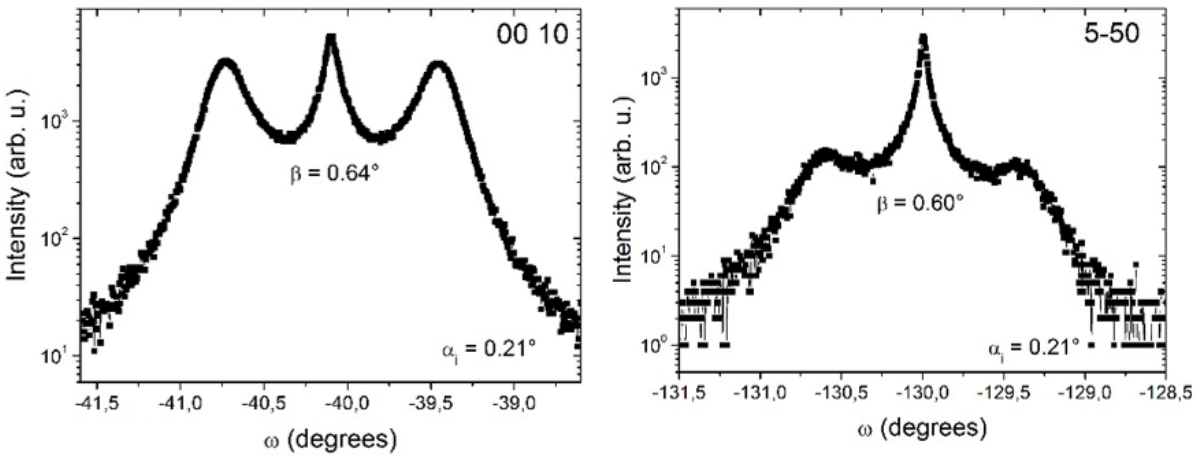

Fig. 5.31: Angular GIXD scans of a 59 nm thick $NaNbO_3$ film on $TbScO_3$.

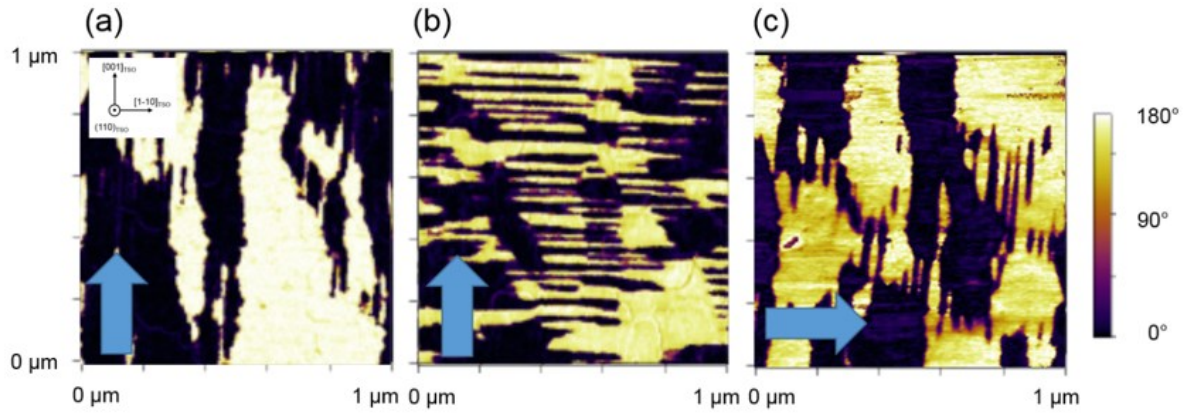

Fig. 5.32: Vertical (a) PFM-phase image of a 65 nm thick $NaNbO_3$ film on a $TbScO_3$ (TSO) substrate. Lateral PFM-phase images measured along the orthogonal orthorhombic substrate directions (b) $[001]_o$ and (c) $[1\text{-}10]_o$, scan directions indicated by blue arrows.

The ferroelectric domains of the films have been investigated by PFM. The observed domain patterns of films in the thickness range between 35 and 65 nm, incorporating similar partial lattice relaxation, do not markedly differ. In Fig. 5.32, VPFM (a) and LPFM (b) phase-images recorded in the same sample area of a partially relaxed film with a thickness of 65 nm are exemplarily shown. In both LPFM and VPFM, a 180° phase shift can be seen. Afterwards, the sample was rotated by 90° for an additional LPFM measurement (Fig. 5.32(c)). The scan directions of the LPFM measurements were aligned along the $[001]_o$ and $[1\text{-}10]_o$ orthorhombic directions of the $TbScO_3$ substrate. Similar but rotated LPFM-phase images are obtained for both scan directions. The observed domain patterns are formed by preferentially arranged stripes. No areas with exclusive in-plane or out-of-plane polarization were visible in PFM amplitude images, which would have been expected for a/c domains (see chapter 1.2.3). This means that in the $NaNbO_3$ films described in this chapter, each domain exhibits both vertical and lateral components of the polarization direction. The observation of monoclinic distortion of the in-plane lattice between the orthorhombic axes indicates that the polarization vectors are aligned along its diagonals, i.e. the pseudocubic axes. In conclusion, the observations from the GIXD measurements and the PFM images can be explained by an a_1c/a_2c configuration

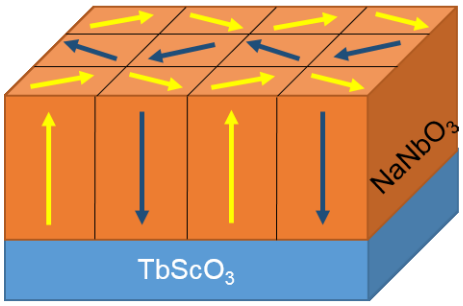

Fig. 5.33: Visualization of a a_1c/a_2c domain pattern of a $NaNbO_3$ film on a $TbScO_3$ substrate.

with vertical domain walls, visualized in Fig. 5.33. To my knowledge, no experimental observation of this type of domain configuration by PFM has been reported in literature, yet. Potential implications of domain walls in ferroelectric materials on technological applications are a subject of recent discussions [49, 157]. In lattice-mismatched thin films, ferroelastic domains such as 90° $a_1/a_2/a_1/a_2$ provide stress relief, allowing the incorporation of lattice strain to higher film thicknesses [46]. Also notable is the recent discovery of domain wall conductivity in La-doped $BiFeO_3$ [158-160], which is interesting for new types of electronic devices. The fundamental understanding of domain formations in thin films is of significant interest although it was not the primary goal of this work.

The observed pattern differs from the published results of 90° a/c domains, found in partially relaxed tetragonal ferroelectric materials under tensile strain such as PZT [156]. There, the individual domains generally exhibit either polarizations in the c- or the a-direction (see chapter 1.2.3). For tetragonal materials on cubic substrates, the expected polarization direction lies exclusively along the long axis (see Fig. 5.34). The a- and c-domains thus result from rotations of the unit cell (a- and c-orientation) as part of the relaxation mechanism. Ferroelectric domain patterns similar to the one observed on $NaNbO_3$ by PFM have for instance been indicated by GIXD measurements of ultrathin (~5 nm) fully strained $PbTiO_3$ on $DyScO_3$ substrates [161]. $NaNbO_3$ is orthorhombic. In the pseudocubic notation, the unit cell is monoclinic with one short and two long axes (see chapter 3.2.1). In the unstrained case, the polarization of ferroelectric orthorhombic materials is expected to be aligned along the diagonal of the surface, spanned by the long axes [162]. The polarization direction was shown to rotate in the monoclinic unit cell under the influence of lattice strain [155].

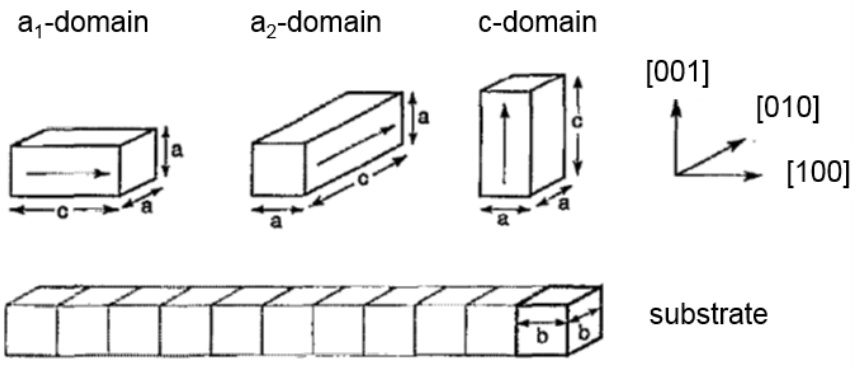

Fig. 5.34: Domain orientations of a tetragonal ferroelectric material on a cubic substrate. The polarization direction is shown for each orientation. Adapted from [163].

Very thin films under sufficient tensile lattice strain (a_c-orientation) were found to exhibit exclusive lateral polarization (e.g. 12 nm $NaNbO_3$ on $DyScO_3$, see chapter 5.5). However, with increasing film thickness, plastic lattice relaxation occurs and the imposed lattice strain is reduced. While the films are still exclusively a_c-oriented (no contribution of c_c-orientation was found in HRXRD 2θ-scans), a vertical component of the polarization evolves.

Notably, the behavior of partially relaxed MOCVD-grown $NaNbO_3$ films on $TbScO_3$ is quite different. Here, exclusive in-plane polarization and striped domain pattern of thin films were retained even to a thickness of 130 nm [23]. The RSMs of MOCVD-grown and PLD-grown films with similar thickness are not markedly different, both films show partial in-plane lattice relaxation. The formation of ferroelectric domains was shown to depend markedly on the deposition conditions (e.g. growth rate, see chapter 5.1.5 and [151]). The growth mechanisms of PLD and MOCVD are fundamentally different. Compared to the chemical processes of MOCVD, the physical deposition of PLD is characterized with higher kinetic energy of the ablated species, high substrate temperature in this particular case (900 °C compared to 700°C) and a high growth rate (3 Å/s compared to 0.1 Å/s). The differences in the domain formation in dependence of the deposition method underline the influence of growth conditions on the ferroelectric properties of strained thin films. Notably, PLD grown films under tensile lattice strain were found to incorporate a vertical polarization component upon the onset of plastic lattice relaxation. Contrary, MOCVD grown films retained exclusive in-plane polarization under similar relaxation conditions.

5.7 Stoichiometry dependence of local hysteresis loops of $NaNbO_3$ films on $SrTiO_3$:Nb substrates

The observation of a *P(E)* hysteresis proves that a material is ferroelectric (see chapter 1.2.4). In order to measure the ferroelectric hysteresis loops of thin films it is necessary to embed them in a capacitor structure consisting of a bottom electrode (conductive substrates or films such as $SrRuO_3$ or $La_xSr_{1-x}MnO_3$) and a top electrode. Thin films, however, often suffer from significant leakage currents. This is especially problematic in films exhibiting off-stoichiometry such as O-vacancies. In this case, it is possible that the highly mobile O-vacancies [164] form conductive channels [165]. A large contribution of leakage current suppresses the formation of hysteresis loops, since the necessary electric field across the ferroelectric material cannot be generated. In order to minimize the negative effect of leakage current on the measurements, and reduce the possibility of electrical shorts that might be present in thin films, it is necessary to use small top contacts (diameter in the 10 µm range). The fabrication of such small contacts requires micro structuring processes (e.g. laser lithography or photolithography process) not available in the Leibniz Institute for crystal Growth where this work was carried out. A

systematic investigation of the required optimization process for the fabrication of micrometer-sized top contacts was not possible at this time and is not a topic of this work.
Alternatively, the conductive tip of the PFM (lateral diameter of a few nanometer) can serve as the top contact. It has to be noted that this approach does not yield quantitative results concerning the coercive field or the remanent polarization of the films. The exact diameter of the tip and thus the area of the top contact is not known. Additionally, the electric field applied by the small tip is not expected to be laterally homogeneous especially when lateral polarization components are present in the film. However, based on the hysteresis curve, it is possible to give a qualitative statement if the material exhibits ferroelectric behavior.

It has been demonstrated in chapter 5.1.5 that film stoichiometry crucially influences the domain formation which is particularly attributed to the formation of point defects in the films. Hence, it is of special interest to study how the film stoichiometry affects the shape of the ferroelectric hysteresis curve. It was investigated how Na- and O-loss on the one hand and Na-excess on the other hand affect the formation of the local ferroelectric hysteresis of $NaNbO_3$ thin films in comparison to a near stoichiometric film. The films were grown on conductive Nb-doped $SrTiO_3$ substrates. The near stoichiometric film was deposited at 2 mbar oxygen background pressure and a substrate temperature of 900°C by the use of a stoichiometric target (see chapter 5.1.2). The increased presence of Na- and O-vacancies in the films was implemented by the decrease of the oxygen background pressure. Films with Na-excess were grown at high oxygen background pressure and the use of Na-rich targets (see chapter 5.1.3). The film thickness of all films was less than the critical thickness for plastic relaxation (see. 5.3) and all films were grown in 2D-growth mode. The growth conditions of the individual samples are summarized in Table 5.5.

Table 5.5: PLD growth conditions, Na/Nb ratio in the target and shape of the hysteresis curve

Growth temperature (°C)	Growth pressure (mbar)	Na/Nb target ratio	Hysteresis
600	0.05	1	closed
600	0.7	1	opening
900	2	1	open
900	2	1.09	closed
900	2	1.17	closed

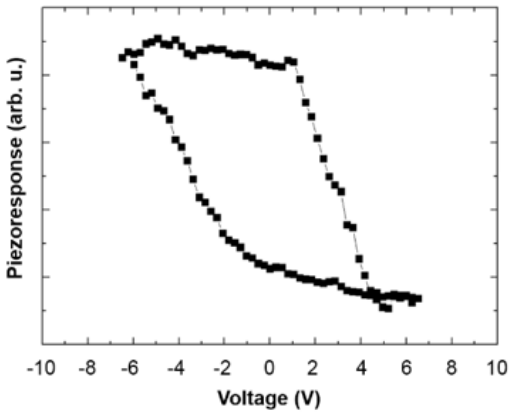

Fig. 5.35: Local hysteresis measurements conducted by the PFM set-up of a near stoichiometric $NaNbO_3$ film on a Nb-doped $SrTiO_3$ substrates.

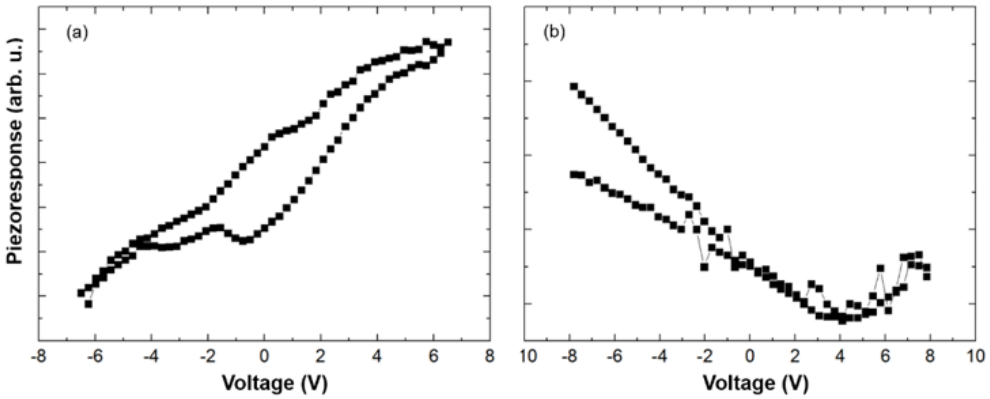

Fig. 5.36: Local hysteresis measurements conducted by the PFM set-up of Na-O deficient $NaNbO_3$ films on Nb-doped $SrTiO_3$ substrates deposited from a stoichiometric target at (a) 0.7 mbar and (b) 0.05 mbar background.

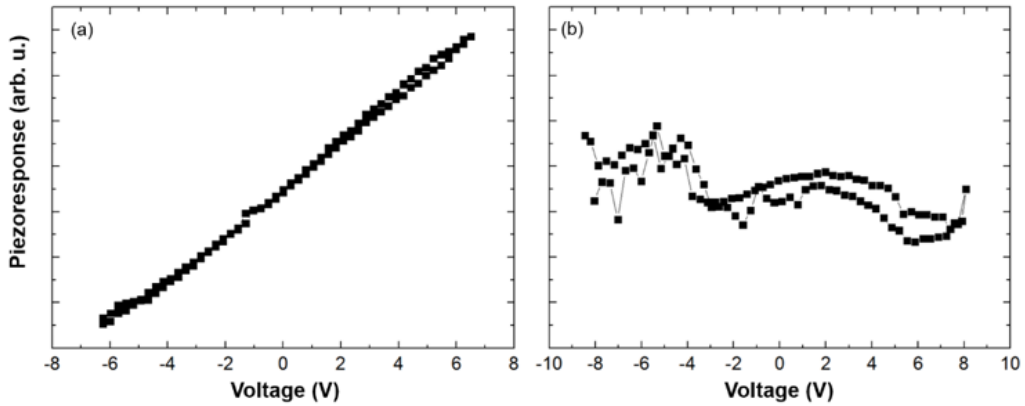

Fig. 5.37: Local hysteresis measurements conducted by the PFM set-up of $NaNbO_3$ films on Nb-doped $SrTiO_3$ substrates at 2 mbar oxygen background pressure using Na excess targets with Na/Nb ratios of (a) 1.09 and (b) 1.17.

The local ferroelectric hysteretic behavior of the films has been measured by the PFM set-up, in the way described above. As the derived values for the piezoresponse amplitude are of a qualitative nature (slightly different effective “top-contact-sizes” on different samples), no numbers are plotted on the y-axes of Figs. 5.35-37. The measurements were performed on several positions on the sample surface in order to test the homogeneity of the films with regard to the hysteretic behavior.

It can be seen that the near stoichiometric film exhibits a pronounced hysteresis curve, typical for a ferroelectric film (Fig. 5.35). Compared to the steep flanks, the area of saturated polarization is very flat. This observation highlights that the near stoichiometric, fully strained $NaNbO_3$ film exhibits promising ferroelectric behavior, opposed to relaxed bulk $NaNbO_3$, which is antiferroelectric at RT.

The local hysteresis loop of a $NaNbO_3$ film with Na and O deficiency (deposited at 0.7 mbar) is significantly less pronounced (Fig. 5.36(a)) with a much smaller gradient of the flanks. In films with even more Na-O deficiencies (deposition at 0.05 mbar), hysteretic behavior is totally lost (Fig. 5.36(b)). The observed trend is in accordance with results published by Palkar et al. [166] and Yun et al. [167], where the hysteresis loops observed for near stoichiometric $BiFeO_3$ thin films was not reproduced in films exhibiting significant oxygen loss. This behavior was mainly attributed to leakage current caused by oxygen vacancies.

Contrary, in $NaNbO_3$ films on $DyScO_3$ substrates deposited at low oxygen pressure the absence of an observable regular domain formation (chapter 5.1.5) is explained by the presence of point defects rather than leakage current.

The $NaNbO_3$ films grown with Na-excess at high background pressure (2 mbar) by the use of targets with Na/Nb ratios of 1.09 and 1.17, respectively, show no local hysteresis as well (Figs. 5.37(a) and 5.37(b), respectively). The effect of A-site off stoichiometry has been discussed by Aggarwal et al. [168] for $Pb_xZr_{1-x}TiO_3$. Here, both lead-vacancies and -excess resulted in degradation of the hysteresis behavior. In the case of lead excess, this was explained by the formation of a secondary PbO phase, resulting in the formation of charged vacancies in the film, compensated by mobile holes. A similar behavior is likely to occur for $NaNbO_3$, where Na excess in the films can be present locally in the form of NaO^{-1} interlayers similar to Ruddlesdon-Popper or Dion-Jacobson phases resulting in a $Na_2NbO_4^{-1}$ phase.

The presented results thus clearly confirm that the film stoichiometry plays a crucial role for the formation of ferroelectric $NaNbO_3$. Consequently, for potential applications it is indispensable to optimize growth conditions in a way to minimize off-stoichiometry. In the case of $NaNbO_3$, near-stoichiometric growth can be achieved either by the deposition in a high oxygen background pressure (e.g. 2 mbar) or the use of Na-O enriched target (e.g. with a Na/Nb ratio of 1.17). This way, strained ferroelectric films exhibiting pronounced hysteresis curves or regularly arranged domain patterns can be grown.

Chapter 6: $K_xNa_{1-x}NbO_3$ films and superlattices

For bulk materials, an enhancement of the ferro-/piezoelectric properties (e.g. piezoelectric response) is observed, when Na in $NaNbO_3$ is partially replaced by K forming the solid solution $K_xNa_{1-x}NbO_3$, with x = 0.5 generally yielding the most promising results [22, 27, 28]. However, the optimal composition with regard to the piezoelectric response can be different from bulk, due to the additional electromechanical boundary conditions relevant to thin films. In this work, thin films with different K content have been deposited from self-made targets. In order to vary the lattice strain in films with a given x, different substrates have been used.

Factsage calculations revealed that at temperatures of 600°C and above, K-oxides are less thermodynamically stable than Na-oxides. Additionally, K has a smaller diffusion coefficient than Na. Thus, the range of the PLD parameters for the 2D growth of stoichiometric films including K is narrower compared to films with only Na at the A position of the perovskite. In effect, within typical PLD parameters for pressure, temperature and laser frequencies it turned out during the course of this work that pure $KNbO_3$ could not be grown with acceptable crystalline quality.

Solid solutions of $(K,Na)NbO_3$ are interesting due to their piezoelectric properties. The aim of the studies presented in this chapter is therefore focused on the impact of the K/Na ratio in fully strained $K_xNa_{1-x}NbO_3$ on the piezoelectric response. Furthermore, the high volatility of K and the related off-stoichiometry make it difficult to reduce leakage current. In contrast to ferroelectric hysteresis measurements, its influence on the piezoelectric response is less interfering.

I therefore concentrated to achieve the deposition of $K_xNa_{1-x}NbO_3$ with different K/Na ratios in a 2D-growth mode, since only atomically smooth surfaces allow a reliable measurement of the piezoelectric coefficient d_{zz}^{eff} by PFM. However, it was found that the thickness up to which $K_xNa_{1-x}NbO_3$ films were deposited in a 2D-growth mode was low compared to $NaNbO_3$ films. As a promising alternative, superlattices with alternating layers under compressive and tensile strain were deposited on $DyScO_3$ substrates. This way, both 2D growth and full in-plane lattice strain of the individual layers was retained for remarkably increased thicknesses compared to single films.

Distinction from other works:

Other groups have grown $K_xNa_{1-x}NbO_3$ films by PLD with thicknesses of the order of several 100 nm. These works concentrated on reducing leakage current by doping the films with Mn [169] or Ti [170]. Additionally, attempts have been made to improve the piezoelectric response and remanent polarization of the films by adding small amounts of Li, Ta and Sb [171], [172]. A. Tian et al. have recently published results on the dependence of the electrical properties of

$K_xNa_{1-x}NbO_3$ films on the deposition temperature [173]. Compared to these works, significantly better crystal ordering and smoother surface morphologies are presented in this thesis, which allows the systematic investigation of dependence of piezoelectric properties on biaxial lattice strain and film composition.

Specht et al. published data about the deposition and characterization of $KTaO_3/KNbO_3$ superlattices on $KTaO_3$ substrates [174]. They showed, that the individual ferroelectric layers are strongly coupled in the superlattice, when the thickness of the paraelectric layers is less than 5 nm [175]. However, the lattice parameter of cubic $KTaO_3$ at RT is a = 3.989 Å, which results in a negligible lattice mismatch of less than -0.1% between $KaTaO_3$ and c_c-oriented $KNbO_3$.

No experimental data about the deposition and characterization of substantially strained $K_xNa_{1-x}NbO_3$ based superlattices with regard to their piezoelectric properties has been published in literature, yet. A theoretical paper by Li et al. predicts high values for the piezoelectric response of $NaNbO_3/KNbO_3$ superlattices [176]. In the work presented here, individual thicknesses of 3 ML or more have been used, since thinner individual films resulted in the growth of solid solutions instead of superlattices.

6.1 $K_xNa_{1-x}NbO_3$ single films

Calculations by the program FactSage (performed by D. Klimm) revealed, that K is not as thermodynamically stable as Na in the temperature range between 750 to 900°C at oxygen background pressures between 0.05 and 2 mbar (plotted in Fig. 6.1). The graphs show the mole fraction of solid K- and Na-oxides on the one hand and gaseous Na and K on the other hand in dependence of temperature at different O_2 pressures. Due to the high laser fluence and the related high temperatures at the PLD target as well as the collisions with the oxygen background-gas molecules, a large fraction of the molecules and ions arriving at the substrate is expected to be of the form Na_2O, K_2O and Nb_2O_5. Although the perovskite structures $(K,Na)NbO_3$ are not implemented in the Factsage program, the calculations for Na_2O, K_2O and Nb_2O_5 provide helpful information about the thermodynamic stability of Na- and K-oxides during PLD-growth of $K_xNa_{1-x}NbO_3$ solid solutions. From Fig. 6.1 it is striking that K_2O is not stable already at low temperatures (< 500°C) and decomposes into the also solid KO_2. The qualitative trends derived from the plots show that the stability region of solid KO_2 is limited by a temperature about 120°C less than in the case of Na_2O. Since the decomposition temperature is just in the range of the used PLD-growth temperatures, this has a crucial effect on film growth. KO_2 decomposes to K and O_2 and evaporates from the film surface at

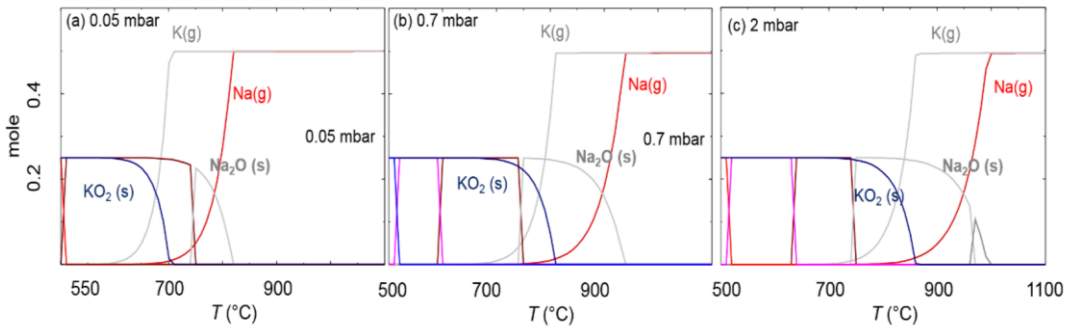

Fig. 6.1: Thermodynamic stability curves of K_2O and Na_2O in dependence of the temperature at background pressures of (a) 0.05 mbar, (b) 0.7 mbar and (c) 2 mbar.

remarkably lower temperatures than Na_2O, which leads to a lower incorporation probability of K in the films. From Fig. 6.2 it is striking, that the decomposition temperatures shift for both materials to lower temperatures when the background pressure is reduced. Thereby, for instance at 0.05 mbar a typical growth temperature of 700°C is above the decomposition temperature of KO_2, but within the stability region of Na_2O. That means, that in order to provide a substantial incorporation of Na and K, the growth temperature has to be lowered or the pressure has to be increased. Nb_2O_5 is not presented in Fig. 6.1, since it is stable for temperatures even above 1100°C for typical PLD background pressures, far away from used substrate temperatures.

However, lowering of the substrate temperature has a negative effect on surface diffusion. One approach to achieve a surface-diffusion length necessary for 2D growth is the deposition at higher temperatures [177]. However, due to the decomposition of solid K-oxides into gaseous K and O_2 at temperatures where Na-oxides are still stable, incorporation of K is reduced. Alternatively, a higher effective surface diffusion length can be achieved by increasing the energy of the adatoms (see chapter 5.1.2), implemented by the deposition at low background pressures like 0.05 mbar. At low background pressures, the decomposition of K-oxides can be avoided if the substrate is heated to a moderate temperature (for instance 600°C). Therefore, the use of 0.05 mbar oxygen background pressure and 600 °C as substrate temperature turned out to be adequate parameters for the growth of $K_xNa_{1-x}NbO_3$ films.

In the following, the K/Na ratio in the films was increased by preparing a corresponding ceramic target.

6.1.1 $K_xNa_{1-x}NbO_3$ films with x = 0.25

Films deposited on $SrTiO_3$, $DyScO_3$ and $NdScO_3$ substrates with a thickness of about 12 nm, employing a $K_{0.25}Na_{0.75}NbO_3$ target, retained the step-and-terrace nature of the substrates (Fig. 6.2). The average lattice mismatch between $K_{0.25}Na_{0.75}NbO_3$ and $DyScO_3$ is small (-0.2%).

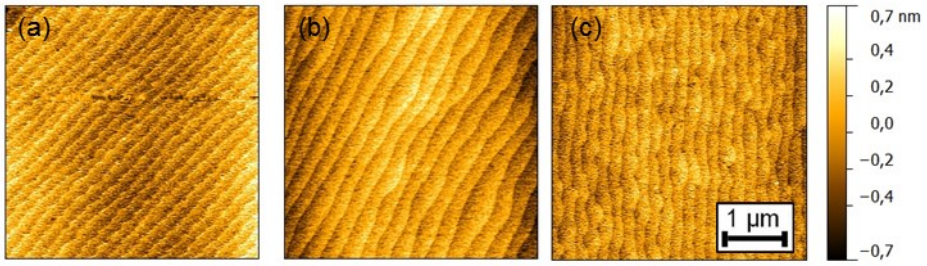

Fig. 6.2: Surface morphology (AFM) of $K_{0.25}Na_{0.75}NbO_3$ films with thickness of 12 nm on (a) $SrTiO_3$, (b) $DyScO_3$ and (c) $NdScO_3$ substrates. Lateral scale is always 4 µm.

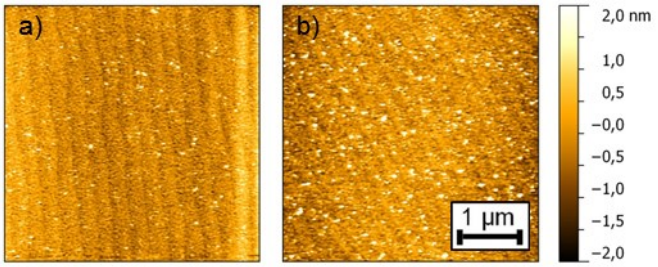

Fig. 6.3: Surface morphology (AFM) of $K_{0.25}Na_{0.75}NbO_3$ films with thickness of (a) 22 nm and (b) 44 nm on $DyScO_3$ substrates. Lateral scale is always 4 µm.

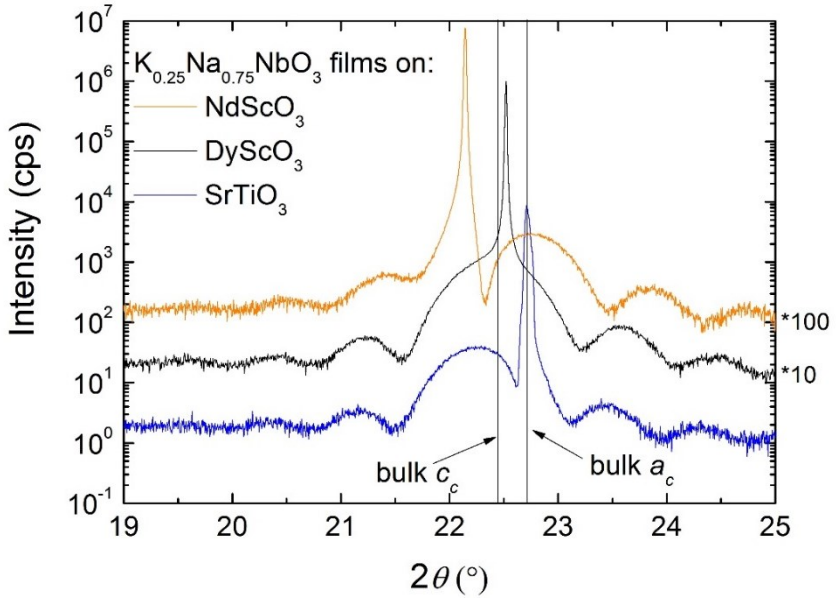

Fig. 6.4: HRXRD *θ-2θ* scans of 12 nm thick $K_{0.25}Na_{0.75}NbO_3$ films on $NdScO_3$, $DyScO_3$ and $SrTiO_3$ substrates in the range of the $(110)_o$ respective $(001)_c$ Bragg peaks. The nominal $(100)_c$ and $(001)_c$ Bragg peak positions of unstrained stoichiometric $K_{0.25}Na_{0.75}NbO_3$ with a_c and c_c orientation are sketched as vertical lines.

Nevertheless, an increase of the film thickness to 22 nm (RMS = 0.5 nm) and further to 44 nm (RMS = 0.7 nm) on $DyScO_3$ substrates (Fig. 6.3) results in the formation of 3D islands on the

steps. It can be clearly seen that the islands are more predominant on the thicker film. This is different to the case of similarly lattice mismatched $NaNbO_3$ on $SrTiO_3$ substrates, where 2D growth was retained up to 60 nm film thickness. The earlier transition to 3D growth in the case of K containing films is tentatively explained by the lower surface-diffusion length of K compared to Na [178, 179]. Opposed to the deposition of $NaNbO_3$, the PLD-growth parameters are not as well suited for the 2D growth of K containing films. First attempts to achieve 2D growth of thicker films by variations of the PLD-growth parameters, like reducing the growth rate, were not successful. For this work, I prioritized on detailed studies of the thin films, where 2D growth was achieved.

HRXRD *θ-2θ* scans of $K_{0.25}Na_{0.75}NbO_3$ films with thicknesses of about 12 nm are shown in Fig. 6.4. The presence of thickness oscillations, similar to the case of $NaNbO_3$ thin films presented in chapter 5.1, reveal the smooth interface and surface as well as good structural quality of the films. The full width of half-maximum (FWHM) of the rocking curve (ω-scan) of the films is the same as for the $NaNbO_3$ thin films (0.02°). According to Table 3.6 in chapter 3, from the bulk-lattice parameters compressive-lattice strain and c_c-surface orientation is expected for epitaxial growth on $SrTiO_3$, while the application of $DyScO_3$ and $NdScO_3$ as substrates is estimated to lead to tensile lattice strain and an a_c-surface orientation. The film-peak positions of the films on $NdScO_3$ and $SrTiO_3$ agree well with the expected film orientations and strain states (Fig. 6.4). This is not the case for the film deposited on $DyScO_3$, where the film Bragg peak is shifted to lower 2θ values referring to the position of bulk $(001)_c$. Here, the experimentally determined out-of-plane lattice parameter of the film corresponds rather to a c_c orientation as opposed to the expected a_c orientation. An explanation is given by an effectively expanded unit cell of $K_{0.25}Na_{0.75}NbO_3$ due to the presence of vacancies similar to $NaNbO_3$ films grown at the same deposition conditions. Oxygen vacancies are most likely present, due to the low oxygen partial pressure during deposition.

Table. 6.1: Lattice parameters and the corresponding unit-cell volume of $K_{0.25}Na_{0.75}NbO_3$ thin films grown on the different substrates. The experimental error interval for the out-of-plane lattice parameter and the unit-cell volume was estimated with ±0.002 Å and ±0.03 Å^3, respectively. Bulk unit-cell volume of $K_{0.25}Na_{0.75}NbO_3$: 61.32 Å^3.

Substrate	**Pseudocubic in-plane lattice parameter (Å)**		**Pseudocubic out-of-plane lattice parameter (Å)**	**Unit-cell volume (Å^3)**
$SrTiO_3$	3.905	3.905	3.980	60.69
$DyScO_3$	3.952	3.947	3.972	61.96
$NdScO_3$	4.002	4.014	3.887	62.44

To check this assumption, the unit-cell volume of the films is determined. RSMs reveal coherent film growth, so that the in-plane lattice parameters of the films are equal to those of

the corresponding substrate (Table 6.1). Since the average lattice mismatch between $K_{0.25}Na_{0.75}NbO_3$ and $DyScO_3$ is only -0.2%, a negligible effect of lattice strain on the out-of-plane lattice parameter and unit-cell volume is expected in this case. In contrast, the increase of the films unit-cell volume with regard to stoichiometric bulk $K_{0.25}Na_{0.75}NbO_3$ is about 1 % (Table 6.1). As in $NaNbO_3$ thin films deposited at 0.05 mbar background pressure (see chapter 5.1.1) this increase is significantly higher than expected from linear elasticity theory. The expansion of the film lattice results in an effective lattice mismatch between film and substrate that yields an expected c_c-orientation, if the same elastic constants are assumed, in accordance with the experimental observation.

Similar to the films on $DyScO_3$, the unit-cell volumes of films on $SrTiO_3$ and $NdScO_3$ are larger than what is expected from linear elasticity theory and is likewise explained by the presence of oxygen vacancies. The observed c_c (a_c) orientation of $K_{0.25}Na_{0.75}NbO_3$ films on $SrTiO_3$ ($NdScO_3$) is in agreement with the expectations described in chapter 3.

In principle, it is possible to reduce the oxygen vacancy density in perovskite-thin films by post-annealing in oxygen atmospheres [180]. However, attempts to this end resulted in the roughening of the surface of $K_xNa_{1-x}NbO_3$ films even at temperatures of 400°C, due to the thermodynamic instability of Na and K in oxygen atmospheres.

6.1.2 $K_xNa_{1-x}NbO_3$ films with x = 0.5 and 0.75

2D growth of $K_xNa_{1-x}NbO_3$ 12 nm thick films with stepped surface morphologies comparable to those presented above were obtained with increased potassium content up to x = 0.5 (Fig. 6.5(a)) at 600 °C substrate temperature and 0.05 mbar oxygen background pressure. A further increase of x to 0.75 or more resulted in 3D growth (Fig. 6.5(b)) at the same deposition conditions, even for 12 nm thick films. Attempts to optimize the PLD growth conditions with regard to the growth mode have been made for film thicknesses below the expected critical thickness for the onset of plastic lattice relaxation. The substrate temperature was increased in order to increase the diffusion length combined with increased background pressure for the thermodynamic stabilization of K. Up to this point; these steps have not yielded 2D growth of $K_{0.75}Na_{0.25}NbO_3$ films. The identification of suitable growth conditions is more difficult to achieve compared to solid solutions with lower x-values, which is attributed to the narrow process-parameter range for the deposition of K containing films (see above). Due to prioritization on the growth of $K_xNa_{1-x}NbO_3$ with $x \leq 0.5$, further experiments for film-growth optimization have not been undertaken.

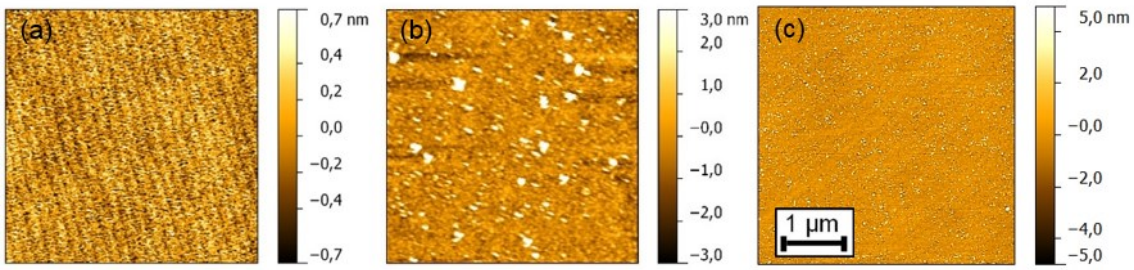

Fig. 6.5: Surface morphology (AFM) of 12 nm $K_xNa_{1-x}NbO_3$ films on $DyScO_3$ substrates with (a) x = 0.5 and (b) x = 0.75. (c) 40 nm $K_{0.5}Na_{0.5}NbO_3$ film on $DyScO_3$. Lateral scale is always 4 µm.

Increasing the film thickness of $K_{0.5}Na_{0.5}NbO_3$ films on $DyScO_3$ substrates to about 40 nm (Fig. 6.5(c), please note the different scale compared to (a)) lead to pronounced 3D-island growth (RMS = 0.9 nm) similar to 40 nm thick $K_{0.25}Na_{0.75}NbO_3$ films.

$K_xNa_{1-x}NbO_3$ films with x = 0.5 and x = 0.75 were only deposited on $DyScO_3$ and $NdScO_3$ substrates to create compressive and tensile lattice strain, respectively, but not on $SrTiO_3$, because lattice mismatch is too large to obtain well-ordered, fully strained films with a reasonable films thickness. From a HRXRD *θ-2θ* scan an out-of-plane lattice parameter of 4.025 Å is derived for a 15 nm thick $K_xNa_{1-x}NbO_3$ film with x = 0.5 on a $DyScO_3$ substrate (Fig. 6.6). Asymmetric RSMs demonstrated fully strained film growth and together with the in-plane lattice parameters, the unit-cell volume was calculated to 62.78 Å³. From a comparison of the out-of-plane lattice parameter of the film with the pseudocubic bulk lattice parameters a_c (3.942 Å) and c_c (4.004 Å) of unstrained $K_{0.5}Na_{0.5}NbO_3$ (both positions are indicated as vertical lines in Fig. 6.6), it is concluded that the film is grown with c_c orientation. The increased value of the out-of-plane lattice parameter compared to the bulk value is attributed to incorporated compressive lattice strain and lattice expansion due to oxygen vacancies. In contrast, a 12 nm thick film on a $NdScO_3$ substrate was found to be a_c oriented, grown under tensile lattice strain (see orange curve in Fig. 6.6). Both results are in accordance with the predictions made in chapter 3 (Materials).

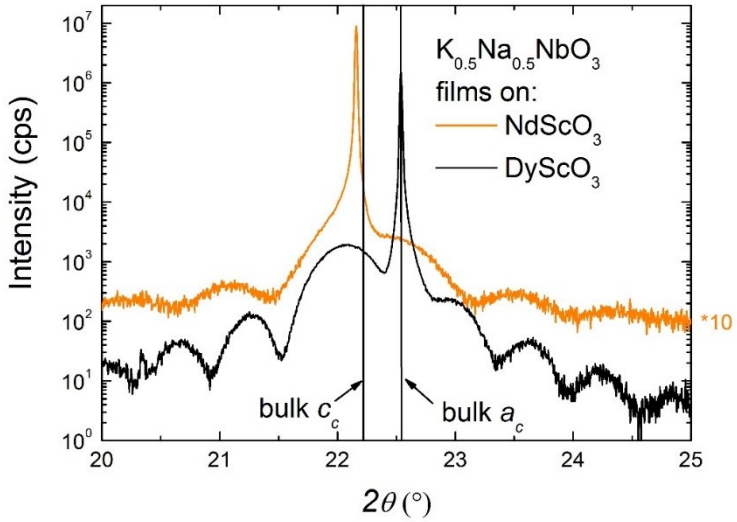

Fig. 6.6: HRXRD θ-2θ scans of $K_{0.5}Na_{0.5}NbO_3$ thin films on $DyScO_3$ (15 nm) and $NdScO_3$ (12 nm) substrates in the range of the $(110)_o$ Bragg peaks.

From the presented results, it can be summarized that only for thin $K_xNa_{1-x}NbO_3$ films (15 nm), fully strained 2D growth was achieved for $x \leq 0.5$. Films with higher K concentration were grown in a 3D-island mode, which is attributed to the lower diffusion coefficient of K compared to Na. Sufficient diffusion lengths were not achieved due to the thermodynamic instability of K-oxides at elevated temperatures.

All films were found to exhibit increased unit-cell volumes attributed to oxygen vacancies, which could not be reduced by increased oxygen background pressure while retaining a 2D growth mode. Thereby, the principle goal of K incorporation into the films was achieved; however, structural quality of the films is not satisfactory with increasing film thickness for reliable piezoresponse measurements.

6.2 $K_{0.5}Na_{0.5}NbO_3$ based superlattices on $DyScO_3$ substrates

The thickness up to which $K_xNa_{1-x}NbO_3$ films were deposited in a 2D-growth mode was found to be limited to values below the expected onset for plastic lattice relaxation. The reliable measurement of the piezoelectric coefficient d_{zz}^{eff} by PFM is not possible on films with rough surfaces. In order to grow $K_xNa_{1-x}NbO_3$ films to higher thickness under full biaxial lattice strain and with atomically smooth surfaces, superlattices with alternating layers under compressive and tensile strain were deposited on $DyScO_3$ substrates. This way, it is possible to reduce stress at the interface between film-stack and substrate. Therefore, the critical thickness for the incorporation of misfit dislocations is expected to increase significantly, compared to a single film. Additionally, the transition from 2D- to 3D-growth mode is reported to be shifted to higher thickness as was shown by L. Goldstein et al. for InAs/GaAs superlattices [181].

In the following, I will concentrate on the material system consisting of $SrTiO_3$ or $NaNbO_3$ and $K_{0.5}Na_{0.5}NbO_3$ films on a $DyScO_3$ substrate. The magnitude of the lattice mismatch of compressively strained $K_{0.5}Na_{0.5}NbO_3$ thin films on $DyScO_3$ substrates is similar to that of tensilely strained $SrTiO_3$ and $NaNbO_3$ thin films on the same substrate. Thus, the average lattice mismatch between the superlattice stack and the substrate is small (~0.2%).
This way, both 2D growth and full in-plane lattice strain of the individual layers was achieved for stacks with thicknesses up to 35 nm.
For the alternation of differently oriented layers that are both ferroelectric, theoretical calculations for tetragonal lead-containing materials predict an enhancement of the piezo/ferroelectric properties of the material [29]. A similar enhancement of piezoelectric coefficients is predicted for $NaNbO_3/KNbO_3$ superlattices [176]. The calculations were based on individual film thicknesses of one monolayer only. Up to now no experimental results for superlattices containing (K,Na)NbO_3 thin films have been published in literature. However, the superlattices presented here were grown with higher individual film thicknesses (> 3 ML), since otherwise a solid solution of $NaNbO_3$ and $K_{0.5}Na_{0.5}NbO_3$ formed.
For comparison, the superlattice $(SrTiO_3)_x/(K_{0.5}Na_{0.5}NbO_3)_y/DyScO_3$ will be considered. $SrTiO_3$ is regarded as an incipient ferroelectric material [182]. That means that, while the material is not ferroelectric under equilibrium conditions even at very low temperatures, it is possible to induce ferroelectric behavior by the application of lattice strain [9]. However, the resulting polarization of strained $SrTiO_3$ films is small. Theoretical calculations have been made on the expected effect of alternating layer stacks of incipient ferroelectric and ferroelectric materials on the net polarization in vertical direction [42]. From these calculations, however, it is not clear whether an improvement or a reduction of the vertical polarization is expected for specific material combinations.

6.2.1 $SrTiO_3/K_{0.5}Na_{0.5}NbO_3$ superlattices

The average in-plane lattice mismatches of $SrTiO_3$ and $K_{0.5}Na_{0.5}NbO_3$ with $DyScO_3$ are 1.1 % and -0.6 %, respectively. The oxygen background pressure was fixed at 0.05 mbar since at higher background pressure no well-ordered films were obtained. Since all films have been deposited at the low oxygen background pressure, lattice expansion due to incorporated oxygen vacancies is expected. Smooth and well-ordered $SrTiO_3$ films were 2D grown at a substrate temperature of 600°C and a pulse frequency of 1 Hz. In contrast to the deposition of $K_xNa_{1-x}NbO_3$ films the target to substrate distance was increased to 60 mm.
Film stacks with a total thickness of about 35 nm consisting of 5 pairs of alternating individual $SrTiO_3$ and $K_{0.5}Na_{0.5}NbO_3$ layers have been deposited on $DyScO_3$ substrates. The thicknesses of the individual layers were adjusted by the pulse ratios shot on the targets to obtain

$SrTiO_3/K_{0.5}Na_{0.5}NbO_3$ thickness ratios of about 1.2 nm / 5.8 nm, 3.5 nm / 3.5 nm and 5.8 nm / 1.2 nm.

The resulting superlattices were found to retain the step-and-terrace surface morphology of the substrates in all cases. In Fig. 6.7(a) the surface morphology of a superlattice made up of individual layers of equal thickness $((SrTiO_3)_{3.5}/(K_{0.5}Na_{0.5}NbO_3)_{3.5})_5$ is exemplarily shown.

HRXRD *θ-2θ* scans of the superlattices of different single layer ratios are presented in Fig. 6.8. The 0-order and the periodically arranged superlattice satellite peaks are clearly visible, confirming the periodic arrangement of the individual layers. As described in chapter 2.5 (XRD), the periodicity of the superlattices can be determined from the angular spacing of the superlattice satellites. This value was found to be about 7 nm in all cases and corresponds well with the thickness of the entire stack as determined from the thickness oscillations (about 35 nm). The 0-order peak of the $((SrTiO_3)_{1.2}/(K_{0.5}Na_{0.5}NbO_3)_{5.8})_5$ is clearly visible at the lower 2θ-angle side of the substrate peak. In contrast, for $((SrTiO_3)_{3.5}/(K_{0.5}Na_{0.5}NbO_3)_{3.5})_5$ and$((SrTiO_3)_{5.8}/(K_{0.5}Na_{0.5}NbO_3)_{1.2})_5$ these peaks are overlapped by the substrate peak and are therefore only visible as shoulders on the low-angle and high-angle side of the $DyScO_3(110)_o$ Bragg peak, respectively. It is striking, that the peak position of the 0-order reflection shifts to higher *2θ* values with an increasing thickness proportion of the individual $SrTiO_3$ layers. The corresponding smaller average out-of-plane parameter of the superlattice is expected, because the lattice parameter of $SrTiO_3$ is significantly smaller than that of $K_{0.5}Na_{0.5}NbO_3$.

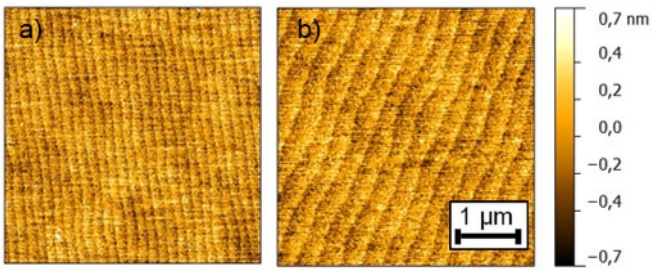

Fig. 6.7: Surface morphology (AFM) of 35 nm thick superlattices with an equal individual layer thickness of about 3.5 nm. (a) $((SrTiO_3)_{3.5}/(K_{0.5}Na_{0.5}NbO_3)_{3.5})_5$ and (b) $((NaNbO_3)_{3.5}/(K_{0.5}Na_{0.5}NbO_3)_{3.5})_5$ on $DyScO_3$. Lateral scale is always 4 µm.

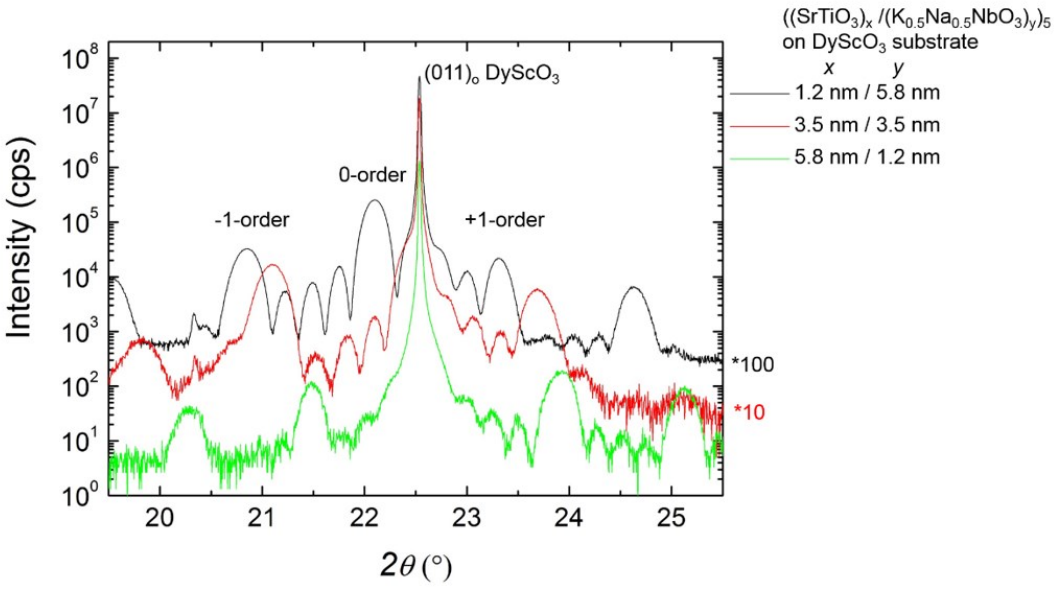

Fig. 6.8: HRXRD *θ-2θ* scans of about 35 nm thick $(SrTiO_3/K_{0.5}Na_{0.5}NbO_3)_5$ superlattices on $DyScO_3$ substrates in the range of the $(110)_o$ Bragg peak. The thickness of the individual layers is given in the legend.

6.2.2 $NaNbO_3/K_{0.5}Na_{0.5}NbO_3$ superlattices

In the case of $NaNbO_3$ and $K_{0.5}Na_{0.5}NbO_3$ the respective average lattice mismatches to $DyScO_3$ are 0.9 % and -0.6 %. The $NaNbO_3$ layers were deposited by the use of a target with a Na/Nb ratio of 1.17 in order to achieve a nearly stoichiometric Na/Nb ratio in the film (see chapter 5.1.3). The $NaNbO_3/K_{0.5}Na_{0.5}NbO_3$ superlattices on $DyScO_3$ substrates have been analyzed with regard to the impact of overall thickness and individual film ratios on the average vertical lattice parameter and the strain state. In all cases, the periodicity (thickness of one $NaNbO_3/K_{0.5}Na_{0.5}NbO_3$ double-layer) was kept constant at 7 nm, as before for the $(SrTiO_3/(K_{0.5}Na_{0.5}NbO_3)_5$ superlattices. All superlattices consist of 5 double-layers. The variation of the individual layer thicknesses for the different superlattices is given in Table 6.2.

Table 6.2: Targeted composition of $NaNbO_3/K_{0.5}Na_{0.5}NbO_3$ superlattices on $DyScO_3$.

Periodicity (nm)	Stack thickness (nm)	Individual $NaNbO_3$ layer thickness (nm)	Individual $K_{0.5}Na_{0.5}NbO_3$ layer thickness (nm)	$d_\perp$ (Å)
7	35	1.2	5.8	4.0
7	35	2.2	4.8	4.002
7	35	3.5	3.5	3.972
7	35	4.8	2.2	3.964
7	35	5.8	1.2	3.886

All superlattices discussed in this section were deposited in a 2D-growth mode (exemplarily shown for $((NaNbO_3)_{3.5}/(K_{0.5}Na_{0.5}NbO_3)_{3.5})_5$ in Fig. 6.7(b)) similar to $((SrTiO_3)_{3.5}/(K_{0.5}Na_{0.5}NbO_3)_{3.5})_5$.

HRXRD *θ-2θ* scans were performed on all superlattices listed in Table 6.2. The obtained double-layer and resulting stack thicknesses amount to 7 nm and 35 nm, respectively. The average out-of-plane lattice parameters of the various superlattices derived from the 0-order peak positions are shown in Fig. 6.9 as a function of the thickness ratio of the individual layers. A strong impact of the thickness ratio of the individual $NaNbO_3/K_{0.5}Na_{0.5}NbO_3$ layers is visible. Beside the superlattice with the smallest $NaNbO_3$ thickness, the value of $d_\perp$ continuously decreases with an increasing fraction of $NaNbO_3$ in the superlattice stack. This behavior is attributed to the smaller lattice parameter of $NaNbO_3$ compared to that of $K_{0.5}Na_{0.5}NbO_3$. Although the largest out-of-plane lattice parameter has been expected for the superlattice with the thickest $K_{0.5}Na_{0.5}NbO_3$ films, $d_\perp$ has slightly been reduced. This observation is explained by partial plastic lattice relaxation in the $((NaNbO_3)_{1.2}/(K_{0.5}Na_{0.5}NbO_3)_{5.8})_5$ superlattice (see Fig. 6.10(a)). This is attributed to the large $K_{0.5}Na_{0.5}NbO_3$ portion, which is less compensated by the very thin $NaNbO_3$ films. All other superlattices are grown fully strained on the DyScO3 substrate, exemplarily shown in Fig. 6.10(b) and (c) for $((NaNbO_3)_{4.8}/(K_{0.5}Na_{0.5}NbO_3)_{2.2})_5$ and $((NaNbO_3)_{5.8}/(K_{0.5}Na_{0.5}NbO_3)_{1.2})_5$, respectively.

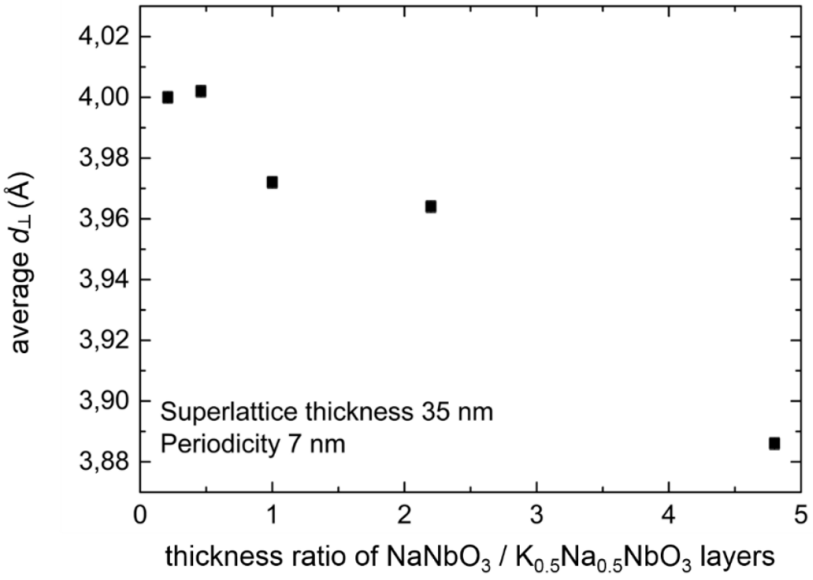

Fig. 6.9: Average vertical lattice parameter $d_\perp$ of $NaNbO_3/K_{0.5}Na_{0.5}NbO_3$ superlattices on $DyScO_3$ substrates with increasing $NaNbO_3/K_{0.5}Na_{0.5}NbO_3$ thickness ratio.

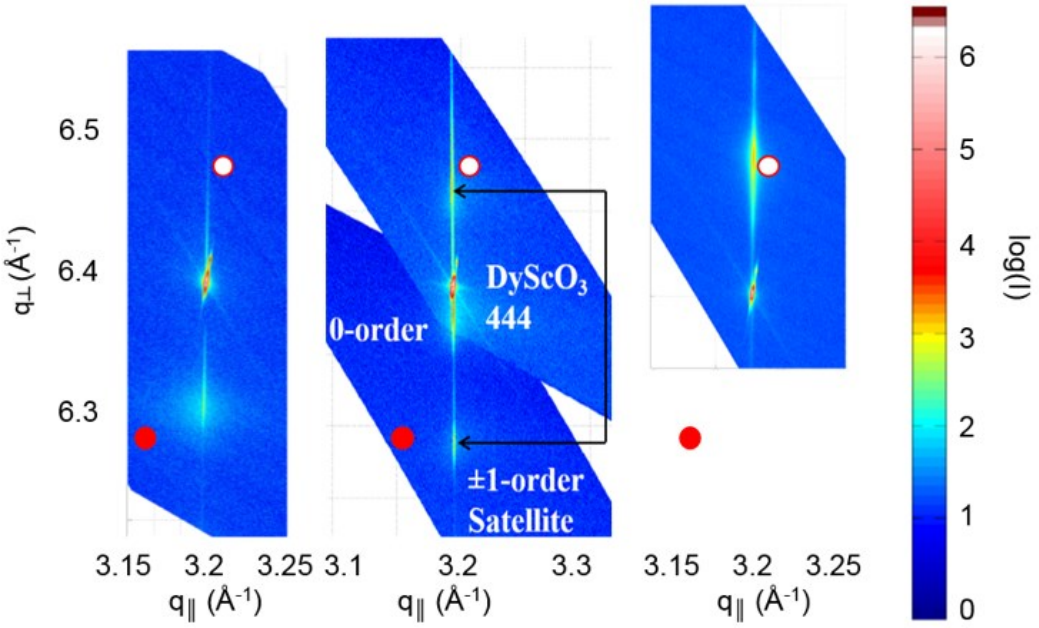

Fig. 6.10: RSMs in the vicinity of the DyScO3(444)$_o$ Bragg reflection of (a) $((NaNbO_3)_{1.2}/(K_{0.5}Na_{0.5}NbO_3)_{5.8})_5$, (b) $((NaNbO_3)_{4.8}/(K_{0.5}Na_{0.5}NbO_3)_{2.2})_5$ and (c) $((NaNbO_3)_{5.8}/(K_{0.5}Na_{0.5}NbO_3)_{1.2})_5$. The bulk positions of $(420)_c$ a_c-oriented $NaNbO_3$ and c_c-oriented $K_{0.5}Na_{0.5}NbO_3$ are indicated by open and closed circles, respectively.

6.2.3 STEM investigation of superlattices

HAADF-STEM measurements have been performed of a $((SrTiO_3)_{3.5}/(K_{0.5}Na_{0.5}NbO_3)_{3.5})_5$ and a $((NaNbO_3)_{3.5}/(K_{0.5}Na_{0.5}NbO_3)_{3.5})_5$ superlattice on $DyScO_3$ substrates in order to investigate the interface between the individual layers and the presence and nature of extended defects in the films. In the case of the $((SrTiO_3)_{3.5}/(K_{0.5}Na_{0.5}NbO_3)_{3.5})_5$ superlattice, the alternation of the stacked layers is clearly visible, due to the high (low) z-contrast of Sr- ((Na,K)-) columns on the A–site of $SrTiO_3$ ($K_{0.5}Na_{0.5}NbO_3$). The interface roughness between the individual layers is about one monolayer, which is attributed to the stepped surface of substrate and films (Fig. 6.11).

In contrast, the visualization of the $NaNbO_3$ to $K_{0.5}Na_{0.5}NbO_3$ interfaces is not possible in STEM. Nb ions with a high atomic number, which generate a high z-contrast, occupy the B-sites in both cases. Thus, the two layers only differ in the A site ions, occupied by Na (in the $NaNbO_3$ films) and by a mixture of Na and K (in the $K_{0.5}Na_{0.5}NbO_3$ films). Both the atomic numbers of Na (z = 11) and the average of Na+K (z = 15) are small. Because of this, the z-contrast between $NaNbO_3$ and $K_{0.5}Na_{0.5}NbO_3$ films is very small making an investigation of the interfaces between and of the thicknesses of the individual layers by STEM impossible.

As the Laue conditions for constructive diffraction in the individual layers are different (different vertical net-plane spacing), a visualization of the individual layers in the superlattice stack was achieved by bright-field TEM measurements (Fig. 6.12(a)). In the bright-field image, no defects

are visible in the initial $NaNbO_3$ layer, similar to the single $NaNbO_3$ layer on $DyScO_3$ discussed in chapter 5.1.4, since the $NaNbO_3$ films were deposited from a Na excess target. Starting with the first $K_{0.5}Na_{0.5}NbO_3$ layer, columnar defects evolve; continuing through the whole superlattice stack.

HAADF-STEM images of the area where such columnar defects were observed revealed that Nb-interstices are located in O-columns (Fig. 6.12(b)). The interstice positioning observed is similar to that found in compressively strained $NaNbO_3$ films on $SrTiO_3$ (see chapter 5.1.4). Thus, this type of columnar defect is again explained by the incorporation of edge-shared NbO_6-octahedra, in contrast to the exclusive corner-sharing BO_6-octahedra in perovskites. The incorporation of this type of defect is believed to provide stress relief in compressively strained films.

Besides the columnar arranged foreign phases, no extended defects such as dislocations were identified, which is in agreement with the matched in-plane lattice parameters of the film to the ones of the substrate determined by RSM.

In single films, the growth rate per pulse of $NaNbO_3$ and $K_{0.5}Na_{0.5}NbO_3$ was identical (0.65 Å/pulse) and the same number of pulses was shot at the two corresponding targets for the deposition of this superlattice. Thus, the thicknesses of the individual layers are expected to be equal. In addition, other superlattices with high and low individual layer thicknesses of the $K_{0.5}Na_{0.5}NbO_3$ films exhibit equal stack thicknesses (see chapter 6.2.2). In contrast, the bright-field image (Fig. 6.12(b)) reveals that the thickness of the $NaNbO_3$ layers is remarkably larger than that of the $K_{0.5}Na_{0.5}NbO_3$ layers. This observation is explained by the following model: Due to phase segregation K is enriched in the (K,Na)NbO_3 stack, so that the K/Na ratio is more than 1. Consequently, due to this segregation effect and the increased K content in the (K,Na)NbO_3 film, the vertical extensions of the K containing stacks have been reduced and the thicknesses of the $NaNbO_3$ films have been increased compared to the nominal stack thicknesses. Chowdury et al. have reported the occurrence of a phase segregation between Na-rich and K-rich phases in epitaxially grown $K_{0.5}Na_{0.5}NbO_3$ films before [183]. In addition, it was shown in chapter 4 (Target preparation) that in $K_{0.25}Na_{0.75}NbO_3$ ceramics [137], a phase segregation is expected up to high sintering temperatures. Since the average composition of the superlattice in Fig. 6.12 is $K_{0.25}Na_{0.75}NbO_3$, which is just in the miscibility gap, the $NaNbO_3$ layers are proposed to act as seed crystals for the phase segregation of $K_{0.5}Na_{0.5}NbO_3$ into $K_xNa_{1-x}NbO_3$ phases with increased (in the limiting case: $KNbO_3$) and reduced values of x (in the limiting case: $NaNbO_3$). From the phase diagram of bulk $K_xNa_{1-x}NbO_3$ (see chapter 3.2.3), for $K_{0.25}Na_{0.75}NbO_3$ such a segregation in an almost pure $KNbO_3$ and $NaNbO_3$ films seems to be thermodynamically favorable. Also, it is considered that the compressive biaxial lattice strain induced in the K containing stack is increased by the increase of the K content. This might be compensated by the remarkably reduced layer thickness.

Evaluation of XRD measurements results in a periodicity of the superlattice of 7 nm. From the bright-field TEM image, individual layer thicknesses of 4.5 nm and 2.5 nm are estimated for the $NaNbO_3$ and K-containing films, respectively. On the basis of these thickness values and under the assumption that the average K/Na ratio in the whole superlattice stack is kept constant (x = 0.25 or K/Na = x/(1-x) = 1/3), an approximate value of x = 0.9 for the K-containing film is determined. The average lattice mismatch between $K_{0.9}Na_{0.1}NbO_3$ and $DyScO_3$ is 2.4%. The expected vertical lattice parameter of fully strained $K_{0.9}Na_{0.1}NbO_3$ on $DyScO_3$ expected from linear elasticity theory is about 4.08 Å. Lattice expansion of fully compressively strained films due to oxygen vacancies was often found to be in the order of 1 % (see chapter 5.1.1). This would result in an effective $d_{\perp}$ of ca. 4.12 Å. Together with the out-of-plane lattice parameter of 3.879 Å for $NaNbO_3$/$DyScO_3$ single films, determined in chapter 5.1.1, an average vertical lattice parameter of the superlattice of 3.97 Å is calculated. This value is in good agreement with the average vertical lattice parameter of the superlattice determined by HRXRD 2θ-scans (3.972 Å). It has to be noted, that these calculations are intended to only serve as an indication that the segregation model is in accordance with XRD measurements. In order to verify the model, EDX-TEM measurements would be necessary, which are – however – not available.

In principle, the large average vertical lattice parameter of the superlattice could also be explained by a lattice-expansion effect of the defects. However, no such significant expansions have been recognized for $NaNbO_3$ films on $DyScO_3$ (chapter 5.1.3), which exhibit a similar defect density.

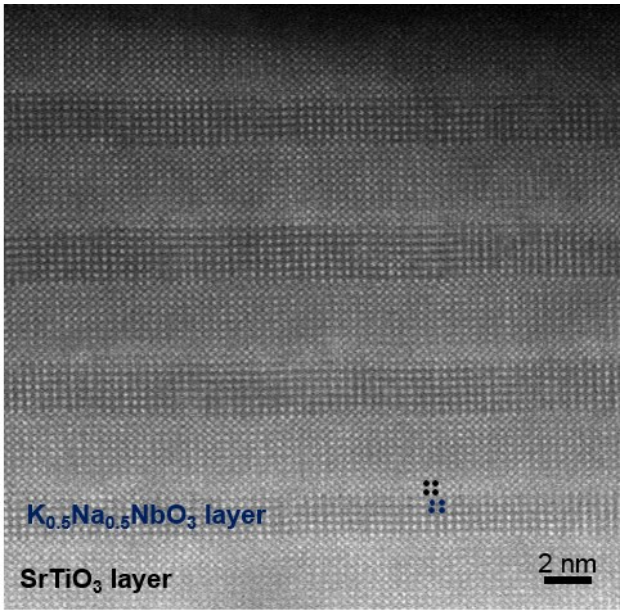

Fig. 6.11: HAADF-STEM image of a 35 nm thick 5x$SrTiO_3$/$K_{0.5}Na_{0.5}NbO_3$ superlattice on $DyScO_3$. The individual layers are clearly visible due to the different z-contrast of Sr (high) / K (low) on the A-site and Ti (low) / Nb (high) on the B-site.

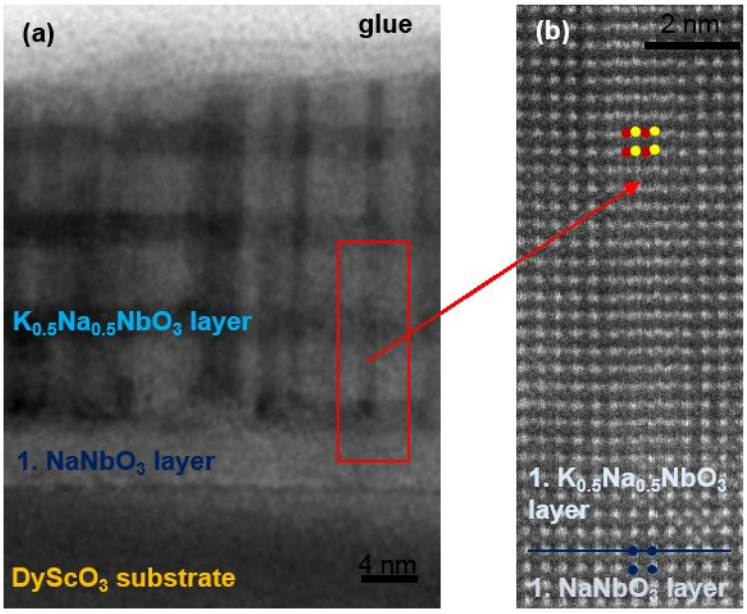

Fig. 6.12: (a) Bright-field TEM image of a 35 nm thick $((NaNbO_3)_{3.5}/(K_{0.5}Na_{0.5}NbO_3)_{3.5})_5$ superlattice on $DyScO_3$. The individual layers are clearly visible. (b) HAADF-STEM image of an area with columnar defects. Nb interstices on O columns are marked by yellow, regular Nb positions in the $K_xNa_{1-x}NbO_3$ host lattice by red dots and additionally by blue dots in the first $NaNbO_3$ layer.

6.3 Domain structure and vertical piezoelectric response of $K_xNa_{1-x}NbO_3$ films and superlattices

For the piezoelectric characterization of $K_xNa_{1-x}NbO_3$ films and superlattices, LPFM and VPFM measurements were performed, in order to identify the vertical and lateral components of the polarization and obtain local values of the piezoelectric component d_{zz}^{eff}. For thin compressively strained $K_{0.5}N_{0.5}NbO_3$ films on $DyScO_3$, no phase contrast was visible in VPFM measurements (Fig. 6.13(a)), but a high piezoresponse amplitude was detected. This observation can be tentatively explained either by polarization directions pointing in the same vertical direction or by 180° phase changes between areas which are too small to be resolved by PFM (lateral size less than 10 nm). In LPFM measurements, small lateral irregularly arranged domains are visible (Fig. 6.13(b)).

Tensilely strained $SrTiO_3$ single thin films on $DyScO_3$ substrates, deposited in the way described above could not be tuned by PFM. Thus, the films are not ferroelectric.

Very thin $NaNbO_3$ films (< 3 nm) on $DyScO_3$ substrates were also found to be non-ferroelectric (see chapter 5.5). This finding was attributed to the nearly squared in-plane lattice of the film imposed by the substrate, since no monoclinic distortion was identified by GIXD. In the

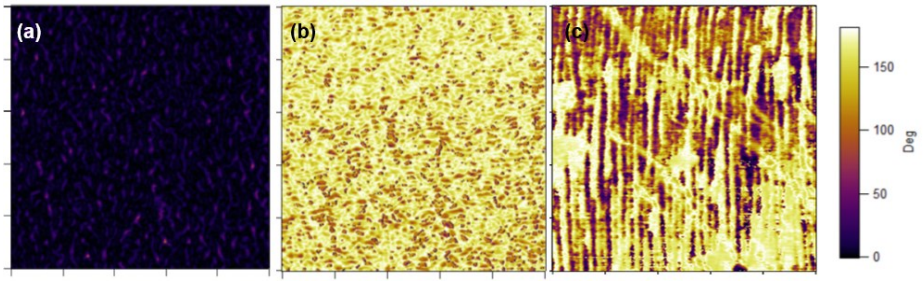

Fig. 6.13: (a) VPFM- and (b) LPFM-phase image of a compressively strained $K_{0.5}Na_{0.5}NbO_3$ thin film on a $DyScO_3$ substrate. (c) LPFM-phase image of a tensilely strained $NaNbO_3$ thin film with exclusive lateral polarization on a $DyScO_3$ substrate. Lateral scale is always 1 µm.

superlattices, $NaNbO_3$ films have been grown more than 6 nm away from the substrate surface. Thus, it is assumed that very thin $NaNbO_3$ films incorporated into the superlattice stack exhibit a monoclinic in-plane distortion and therefore exhibit ferroelectric behavior. The LPFM phase image of a 6 nm thick $NaNbO_3$ film from chapter 5.5.1 is shown again in Fig. 6.13(c).

A VPFM-phase image of a $((SrTiO_3)_{3.5}/(K_{0.5}Na_{0.5}NbO_3)_{3.5})_5$ superlattice on $DyScO_3$ is shown in Fig. 6.14(a), a significant amplitude signal was simultaneously measured. Here, no tuning of the LPFM was possible, revealing that the polarization direction is purely vertical. Similar results have been obtained for the $((SrTiO_3)_{1.2}/(K_{0.5}Na_{0.5}NbO_3)_{5.8})_5$ superlattice. In contrast, it was not possible to tune the $((SrTiO_3)_{5.8}/(K_{0.5}Na_{0.5}NbO_3)_{1.2})_5$ superlattice with a low $K_{0.5}Na_{0.5}NbO_3/SrTiO_3$ ratio both in LPFM and VPFM. It is therefore concluded that this structure is not piezo/ferroelectric.

All $NaNbO_3/K_{0.5}Na_{0.5}NbO_3$ superlattices on $DyScO_3$ were found to exhibit lateral and vertical piezoelectric response. As for $K_{0.5}Na_{0.5}NbO_3$ single films on $DyScO_3$, the VPFM-phase images of these superlattices show no phase shift (exemplarily shown in Fig. 6.14(b) for $((NaNbO_3)_{3.5}/(K_{0.5}Na_{0.5}NbO_3)_{3.5})_5$. They exhibit a strong VPFM-amplitude signal. The LPFM-

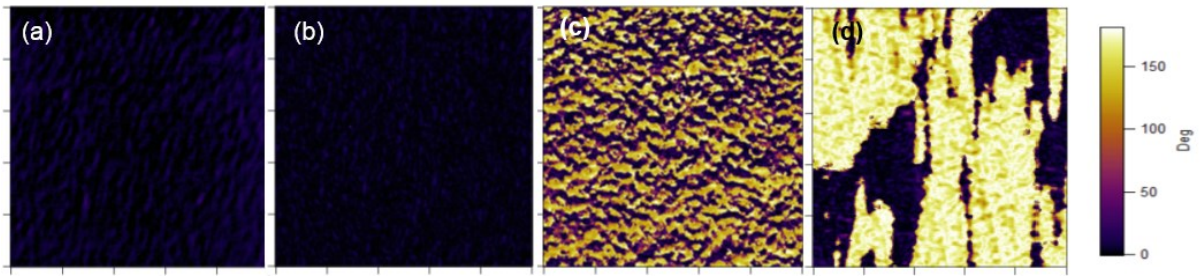

Fig. 6.14: VPFM-phase images of net compressively strained (a) $((SrTiO_3)_{3.5}/(K_{0.5}Na_{0.5}NbO_3)_{3.5})_5$ and (b) $((NaNbO_3)_{3.5}/(K_{0.5}Na_{0.5}NbO_3)_{3.5})_5$ superlattice. LPFM-phase images of (c) a net compressively strained $((NaNbO_3)_{3.5}/(K_{0.5}Na_{0.5}NbO_3)_{3.5})_5$ and (d) a net tensilely strained $((NaNbO_3)_{5.8}/(K_{0.5}Na_{0.5}NbO_3)_{1.2})_5$ superlattice. In all cases, $DyScO_3$ was used as a substrate. Lateral scale is 1 µm.

phase images of most of these superlattices are very similar to that found for $K_{0.5}Na_{0.5}NbO_3$ single films on $DyScO_3$ (Fig. 6.13(b)), exemplarily shown for $((NaNbO_3)_{3.5}/(K_{0.5}Na_{0.5}NbO_3)_{3.5})_5$ in Fig. 6.14(c). A notable exception is the $((NaNbO_3)_{5.8}/(K_{0.5}Na_{0.5}NbO_3)_{1.2})_5$ superlattice, where a complex lateral domain pattern was observed (Fig. 6.14(d)). Due to the high proportion of $NaNbO_3$, this superlattice is net tensilely strained. This domain configuration can be tentatively described as a sequence of a_1c/a_2c domains, in which the vertical component of the polarization is pointing in a single direction over a large area (at least 1x1 µm²).

Based on the PFM measurements of single $NaNbO_3$ (see chapter 5.5) and $K_{0.5}Na_{0.5}NbO_3$ thin films, a model for the polarization components in the superlattices is suggested. A schematic visualization for $((SrTiO_3)_x/(K_{0.5}Na_{0.5}NbO_3)_y)_5$ and $((NaNbO_3)_x/(K_{0.5}Na_{0.5}NbO_3)_y)_5$ superlattices is shown in Fig. 6.15. The $SrTiO_3$ layers are not polarized and the lateral polarization component of $K_{0.5}Na_{0.5}NbO_3$ layers is suppressed in the $((SrTiO_3)_x/(K_{0.5}Na_{0.5}NbO_3)_y)_5$ superlattice (Fig. 6.15(a)). Very thin $K_{0.5}Na_{0.5}NbO_3$ layers (~ 1.2 nm) embedded between paraelectric layers are not polarized (Fig. 6.15(b)). For ferroelectric films, a critical minimal thickness for the evolution of a polarized state has been identified. For example, such a critical thickness is reported to be about 1.2 nm for $PbTiO_3$ [184] thin films at RT. In addition, **f**or a paraelectric/ferroelectric superlattice, a reduced vertical polarization is predicted by theoretical calculations [42]. Ghosez and Junquera carried out that the vertical polarization of the ferroelectric material is expected to point in the same direction in all layers, if the distance between these layers (i.e. the thickness of the paraelectric layer) is only a few nm. A paraelectric layer embedded between two ferroelectric ones is not able to compensate the accumulation of e.g. positive (negative) charges in the ferroelectric material close to the lower (upper) interface (see Fig. 6.16). As a result, a depolarization field (indicated by the dashed arrow) is generated across the insulating layer, directed opposite to the polarization of the ferroelectric layer. Thus, the vertical polarization is reduced. In the case of the $((SrTiO_3)_{5.8}/(K_{0.5}Na_{0.5}NbO_3)_{1.2})_5$ superlattice, it is assumed that the depolarization field across the relatively thick $SrTiO_3$ layers effectively screen the polarization in the $K_{0.5}Na_{0.5}NbO_3$ films. Additionally, the depolarization field across the paraelectric layer couples the domains in the neighboring ferroelectric ones [185] and is proposed to suppress the lateral polarization components in the $K_{0.5}Na_{0.5}NbO_3$ layers.

In ferroelectric/ferroelectric superlattices such as $NaNbO_3/K_{0.5}Na_{0.5}NbO_3$, the lateral polarization direction of the individual layers is not expected to be affected by neighboring ferroelectric films [42]. In contrast, the vertical polarizations of adjacent layers are expected to be coupled [29], which means that locally, the vertical component of the polarization points in the same direction in all layers. Furthermore, very thin $NaNbO_3$ films ($t \leq 3$ nm) were found to exhibit the nearly squared in-plane lattice of $DyScO_3$ (see chapter 5.5), which effectively

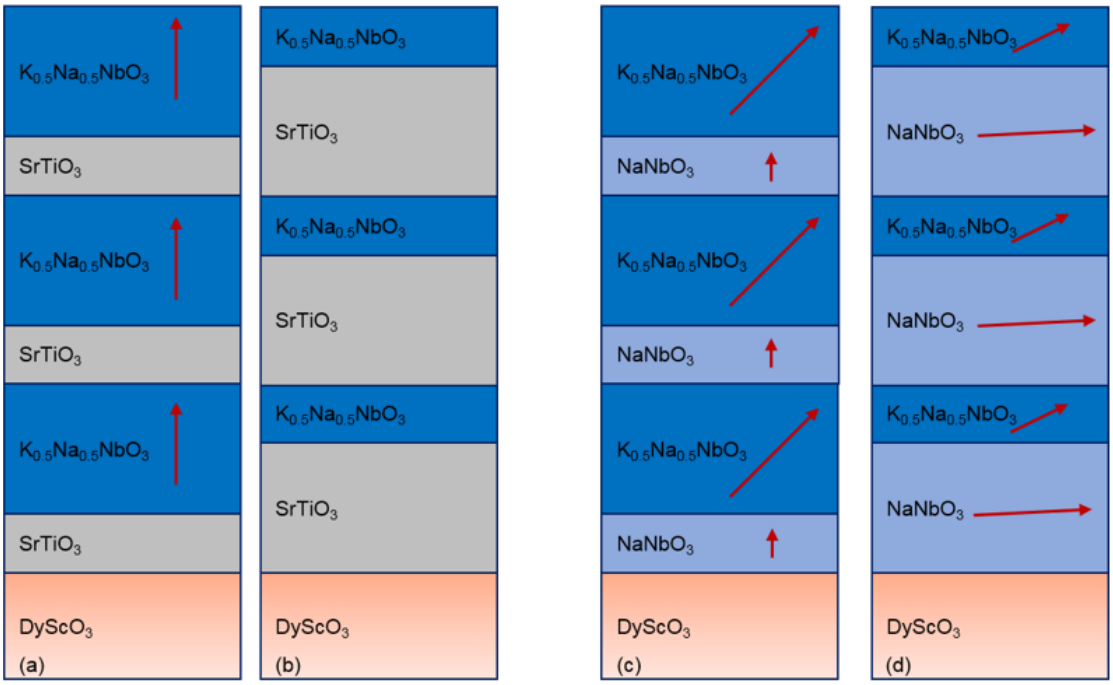

Fig. 6.15: Schematic visualization of the polarization components present in the individual layers of (a) $((SrTiO_3)_{1.2}/(K_{0.5}Na_{0.5}NbO_3)_{5.8})_5$ and (b) $((SrTiO_3)_{5.8}/(K_{0.5}Na_{0.5}NbO_3)_{1.2})_5$ (c) $((NaNbO_3)_{1.2}/(K_{0.5}Na_{0.5}NbO_3)_{5.8})_5$ and (d) $((NaNbO_3)_{5.8}/(K_{0.5}Na_{0.5}NbO_3)_{1.2})_5$ superlattices on $DyScO_3$ substrates.

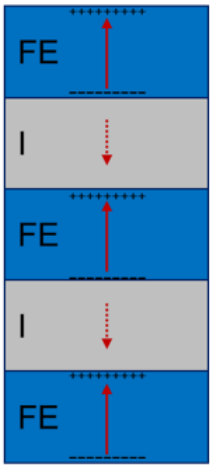

Fig. 6.16: Schematic view of the charges accumulated in the ferroelectric layers (FE) and the resulting depolarization field in the insulating material (I).

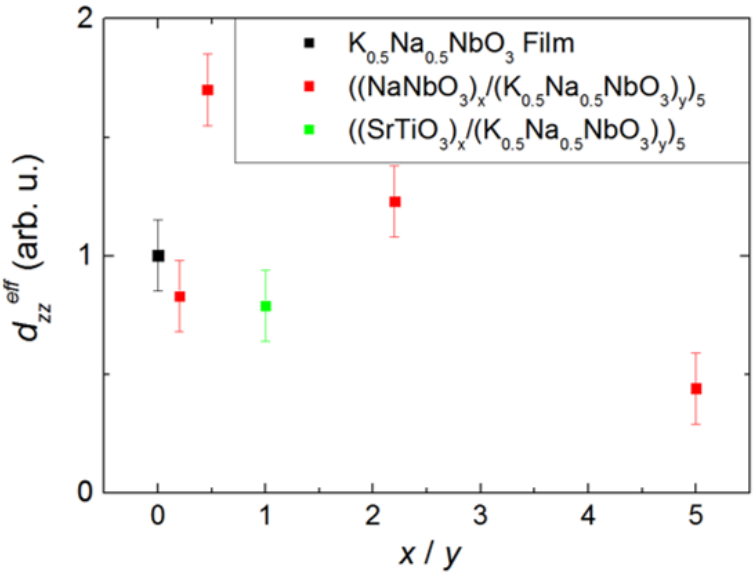

Fig. 6.17: Qualitative trend of d_{zz}^{eff} values of $K_{0.5}Na_{0.5}NbO_3$ based films and superlattices on $DyScO_3$. Black square: $K_{0.5}Na_{0.5}NbO_3$ single film, red squares: $((NaNbO_3)_x/(K_{0.5}Na_{0.5}NbO_3)_y)_5$ superlattices, green square: $((SrTiO_3)_{3.5}/(K_{0.5}Na_{0.5}NbO_3)_{3.5})_5$ superlattice. Normed to the value of the $K_{0.5}Na_{0.5}NbO_3$ single film.

suppressed lateral polarization in a-oriented films. In addition, a nearly squared in-plane lattice is expected for c-oriented $K_{0.5}Na_{0.5}NbO_3$ layers. Thus, exclusive vertical polarization is proposed for the individual $NaNbO_3$ layers with thickness of less than 3 nm (Fig. 6.15(c)). In contrast to the situation of the $((SrTiO_3)_{5.8}/(K_{0.5}Na_{0.5}NbO_3)_{1.2})_5$ superlattice, a vertical polarization was detected even in a superlattice with a very small individual $K_{0.5}Na_{0.5}NbO_3$ layer thickness (Fig. 6.15(d)). It is proposed that no vertical depolarization field is formed across the ferroelectric $NaNbO_3$ layers and thus, the vertical polarization of the very thin $K_{0.5}Na_{0.5}NbO_3$ layers is not screened.

In contrast to pure $NaNbO_3$ thin films, the compressively strained $K_{0.5}Na_{0.5}NbO_3$ based samples on $DyScO_3$ exhibit strong piezoelectric amplitudes measured by PFM. For a rough estimation of the influence of K content in the films, the vertical amplitude signals of superlattices with different *x* and *y* have been evaluated. This method does not allow an absolute determination of d_{zz}^{eff}. However, all films were measured under the same conditions, which allows a relative comparison of d_{zz}^{eff}. In Fig. 6.17 the results of $((NaNbO_3)_x/(K_{0.5}Na_{0.5}NbO_3)_y)_5$ superlattices (red squares) with increasing *x*/*y* ratio (*x* + *y* = 7nm in all cases), a $((SrTiO_3)_{3.5}/(K_{0.5}Na_{0.5}NbO_3)_{3.5})_5$ superlattice (green square) and a $K_{0.5}Na_{0.5}NbO_3$ single film (*x*/*y*= 0, black square) are shown. Only the superlattice with *x*/*y* = 0.21 $((NaNbO_3)_{1.2}/(K_{0.5}Na_{0.5}NbO_3)_{5.8})_5$) was found to exhibit partial lattice relaxation, all other samples are grown fully strained on the $DyScO_3$ substrate.

The $((SrTiO_3)_{3.5}/(K_{0.5}Na_{0.5}NbO_3)_{3.5})_5$ superlattice exhibits a significantly smaller d_{zz}^{eff} value than the fully strained ferroelectric/ferroelectric $((NaNbO_3)_x/(K_{0.5}Na_{0.5}NbO_3)_y)_5$ superlattices with *x*/*y*

ratios of 0.5 and 2.2. This is understandable, since the depolarization fields generated across the insulating layers are directed opposite to the polarization of the ferroelectric layer (see above), and hence the vertical polarization and subsequently the d_{zz}^{eff} value of the stack is reduced.

For strained ferroelectric/ferroelectric superlattices, only few experimental reports have been made. They include $PbTiO_3/PbZrO_3$ on (100)Pt-coated MgO substrates [186] and $PbZr_{0.4}Ti_{0.6}O_3/PbZrO_3$ on (100)$SrTiO_3$ substrates [187]. In both cases, the individual films were a-oriented, opposed to for instance typically c-oriented PZT on $SrTiO_3$. Furthermore, the superlattices were not grown fully strained on the substrates. Accordingly, reduced polarization and d_{zz}^{eff} values compared to single films were obtained. No experimental reports on similar superlattices with c-oriented films have been found. In contrast, recent theoretical calculations predict significantly enhanced polarization and d_{zz}^{eff} values in strained $PbTiO_3/BaTiO_3$ superlattices [29].

The general trend found for the $((NaNbO_3)_x/(K_{0.5}Na_{0.5}NbO_3)_y)_5$ superlattices is, that an increased thickness proportion of the $K_{0.5}Na_{0.5}NbO_3$ layers up to y = 4.8 resulted in increasing d_{zz}^{eff} values. However, if the thickness of the $K_{0.5}Na_{0.5}NbO_3$ layers is increased to 5.8 nm, the superlattice partially relaxes and d_{zz}^{eff} significantly decreases.

Thus, increasing the $K_{0.5}Na_{0.5}NbO_3$ ratio in the superlattices has two impacts: (i) higher compressive strain, which is known to improve piezoelectric properties in out-of-plane direction [8], and (ii) more incorporated (average) K in the superlattice. For bulk $K_xNa_{1-x}NbO_3$ an increase of the piezoresponse is expected for increasing K up to $x \approx 0.5$ at the morphotropic phase boundary, which can also explain the increase of d_{zz}^{eff} in Fig. 6.19 from x/y = 5 to x/y = 0.5. In this regard, ideally a composition of x = 0.5 (in average) is assumed to result in highest d_{zz}^{eff} values. This can only be achieved for $K_{0.5}Na_{0.5}NbO_3$ single layers, which – however – start to partially relax at very low film thickness. Only 15 nm thick layers were grown fully strained on $DyScO_3$ substrates, which thus yield significantly lower d_{zz}^{eff} values (see black circle in Fig. 6.17). At this time, it is not possible to conclude whether the superlattices exhibit enhanced d_{zz}^{eff} values compared to single $K_{0.5}Na_{0.5}NbO_3$ films.

Consequently, in terms of optimization, the growth of thick films with a K/Na ratio of about 0.5 under compressive lattice strain would be favorable. Since this was not possible, the deposition of superlattice is an adequate alternative way to obtain enhanced properties as it is has been shown above.

Conclusion and Outlook

$NaNbO_3$

In this work, the coherent 2D growth of thin $NaNbO_3$ single films with nearly stoichiometric composition by pulsed laser deposition was achieved by systematic optimizations of the growth process. Compressive (tensile) lattice strain has been incorporated in films deposited on $NdGaO_3$ ($DyScO_3$ and $TbScO_3$) substrates. Large anisotropic strain has been incorporated in films grown on $SrTiO_3$ substrates, while the average lattice mismatch between substrate and film is small.

The amount of sodium and oxygen vacancies in the films was found to be critically affected by the oxygen background pressure and Na/Nb ratio in the applied targets. By increasing the oxygen pressure to 2 mbar or the Na/Nb ratio in the targets up to 1.17, sodium and oxygen vacancies have been significantly decreased. HAADF-STEM investigations of thin $NaNbO_3$ films under full tensile strain have revealed columnar defects in Na- and O deficient films, deposited at low oxygen-background pressure (0.05 mbar) by the use of a stoichiometric target. The precipitates exhibit a lateral size of about 2 nm and extend nearly across the whole vertical film thickness. No such extended defects have been found in films, deposited either by using a Na(O)-excess target with a Na/Nb ratio of 1.17, or by maintaining a higher oxygen-background pressure of 2 mbar and the use of a stoichiometric target. In contrast, when inducing compressive strain by growing on $SrTiO_3$ substrates, columnar defects recurred in films deposited using a Na(O)-excess target with a Na/Nb ratio of 1.17 and at 0.05 mbar oxygen background pressure. Here, the Nb-interstice positioning can be explained by the incorporation of edge-shared NbO_6-octahedra, which are not present in perovskites. This provides for an efficient mechanism to relax the lattice stress in films under compressive strain. Thus, biaxial strain affects off-stoichiometry and the presence and type of precipitates in the films. It is proposed that deposition under higher oxygen-background pressure (2 mbar) and by the use of a stoichiometric target yields near-stoichiometric $NaNbO_3$ film growth on $SrTiO_3$ substrates. In conclusion, the deposition conditions allowing for near-stoichiometric film growth also depend on the used substrate.

In tensilely strained $NaNbO_3$, regular ferroelectric domains have only been found in near-stoichiometric films. The domain ordering has been found to depend on the growth rate. Higher growth rates result in higher effective supersaturation, while volatile components in the films have more time to desorb at lower growth rates. In both cases, such behavior is assumed to result in the incorporation of point defects during growth. The best ordered domain arrangement has been achieved at a laser pulse frequency of 5 Hz.

Fully strained thin films on $DyScO_3$ exhibit 1D lateral stripe domain patterns (a1/a2), with an arrangement similar to those grown by metal-organic chemical vapor deposition (MOCVD).

In partially relaxed films on $TbScO_3$ substrates, ferroelectric a_1c/a_2c domain structures have been identified. In contrast, partially relaxed MOCVD-grown films with similar thickness were reported to retain the exclusive lateral polarization of fully strained films [38]. Accordingly, as the film thickness increases, there are differences in the evolution of ferroelectric domains during PLD and MOCVD mediated film growth. This is attributed to the different growth kinetics of the deposition methods. Opposed to $NaNbO_3$, typically $a_1/c/a_2/c$ domains have been observed in ferroelectric films with tetragonal symmetry under tensile strain [156]. The occurrence of different domain configurations in $NaNbO_3$ films is tentatively attributed to monoclinic film structure and anisotropic lattice strain [23, 43].

In strained $NaNbO_3$ on (001) $SrTiO_3$, distinct local ferroelectric hysteresis loops have been observed in near-stoichiometric films. Thus, it was confirmed that a ferroelectric room temperature phase can be induced by incorporating biaxial compressive lattice strain in $NaNbO_3$, which exhibits antiferroelectric properties in the unstrained state. However, no hysteresis behavior has been observed in films incorporating either a significant Na- or O-vacancy density or a significant Na-excess. This is attributed to the formation of nm sized columnar precipitates.

The present work will significantly contribute to a targeted adjustment of film properties by choosing appropriate deposition parameters and substrate materials and to come to a better comprehension of the growth of alkali-niobate thin films. For the first time, such detailed investigations have been made of promising piezo/ferroelectric $NaNbO_3$ films.

$K_xNa_{1-x}NbO_3$ films and superlattices

Experiments in this work show that fully strained $K_xNa_{1-x}NbO_3$ films with $x \leq 0.5$ can be grown in 2D-growth mode on various substrates. However, due to thermodynamic reasons, well-ordered $K_xNa_{1-x}NbO_3$ film growth could only be realized at low substrate temperature (600°C) and oxygen-background pressure (0.05 mbar). Such deposition conditions lead - however - to an oxygen off-stoichiometry, correlated with a high density of point defects similar to epitaxial $NaNbO_3$ films deposited under the same growth conditions. Hence, the deposition of $K_{0.25}Na_{0.25}NbO_3$ films on $DyScO_3$ substrates has been found to exhibit a transition from 2D- to 3D-growth mode at very low film thicknesses, resulting in films with deteriorated surface morphology already at thicknesses of about 20 nm. This is well below the estimated critical thickness for the onset of plastic lattice relaxation, which is attributed to the lower surface diffusion of K compared to Na.

A possibility to improve film morphology was shown to be realized by the deposition of superlattices. In this way, in comparison to single $K_{0.5}Na_{0.5}NbO_3$ films, the critical thickness for the onset of plastic lattice relaxation has been significantly increased by depositing $((NaNbO_3)_x/(K_{0.5}Na_{0.5}NbO_3)_y$ superlattices on $DyScO_3$ substrates. In this stack sequence, the

strain alternates between tensile in $NaNbO_3$ and compressive in $K_{0.5}Na_{0.5}NbO_3$ layers. 2D growth of such net compressively strained superlattices has been achieved for stack thicknesses of at least 35 nm. XRD measurements exhibit well-ordered superlattice structures, which has not been previously reported for this system. Due to existing O and Na/K deficiencies in the $K_{0.5}Na_{0.5}NbO_3$ films, the presence of columnar defects similar to those in $NaNbO_3$ films under compressive strain has been observed in HAADF-STEM measurements. Furthermore, phase segregation has been detected between the $NaNbO_3$ and $K_{0.5}Na_{0.5}NbO_3$ layers. Thereby, the individual $NaNbO_3$ layer thickness and the K/Na ratio in the $K_xNa_xNbO_3$ layers increases, while the thickness of the latter decreases. This clearly demonstrates the influence of kinetic and thermodynamic constraints in the form of diffusion and stability on structural and ferroelectric film properties.

The ferroelectric domain structure of $((NaNbO_3)_x/(K_{0.5}Na_{0.5}NbO_3)_y)_5$ superlattices under net compressive strain consists of very small irregularly arranged lateral ferroelectric domains. As typical for incorporated compressive film strain, these superlattices exhibit a strong VPFM-amplitude signal. Lateral domains extending over a larger area have been obtained in a $((NaNbO_3)_{5.8}/(K_{0.5}Na_{0.5}NbO_3)_{1.2})_5)$ superlattice under net tensile strain, being tentatively described as a_1c/a_2c, which is similar to the case of partially relaxed $NaNbO_3$ under tensile lattice strain.

Strong local piezoelectric amplitudes in the vertical direction, correlated with the effective piezoelectric coefficient d_{zz}^{eff}, have been detected in compressively strained $K_{0.5}Na_{0.5}NbO_3$ thin films on $DyScO_3$ substrates. Further improved values of the local effective piezoelectric coefficient d_{zz}^{eff} have been obtained by growing ferroelectric/ferroelectric $((NaNbO_3)_x/(K_{0.5}Na_{0.5}NbO_3)_y)_5$ superlattices under net compressive strain, whereby the full in-plane lattice strain has to be maintained. The highest local effective piezoelectric coefficient has been achieved for a fully strained $((NaNbO_3)_{2.2}/(K_{0.5}Na_{0.5}NbO_3)_{4.8})_5$ superlattice on $DyScO_3$. Inducing full strain in 2D grown $K_xNa_{1-x}NbO_3$ films of appropriately high thickness is challenging, due to the low thermodynamic stability in combination with the low diffusion coefficient of K-oxides. This problem has been successfully addressed by the growth of ferroelectric/ferroelectric $NaNbO_3/K_{0.5}Na_{0.5}NbO_3$ superlattices on $DyScO_3$ substrates, incorporating tensile and compressive lattice strain in the alternating layers. Additionally, by the growth of such superlattices, the high piezoelectric coefficients of compressively strained $K_{0.5}Na_{0.5}NbO_3$ thin films have been further enhanced. Thus, it has been shown that growth of lead-free $((NaNbO_3)_x/(K_{0.5}Na_{0.5}NbO_3)_y)_5$ superlattices under net compressive strain yields structures with promising piezoelectric coefficients.

Outlook

The present work shows that ferro-/piezoelectric properties of alkaline niobate films and superlattices can be tuned by lattice strain, film composition and stack sequence. However, for potential applications of these films, the piezo/ferroelectric properties of strained $NaNbO_3$ and $K_xNa_{1-x}NbO_3$ thin films and superlattices have to be quantitatively determined. In order to allow for such investigations, it will be necessary to embed the superlattices in a capacitor structure, with suitable bottom and top electrode contacts. This will allow the quantification of the remanent polarization, coercive field, leakage current and piezoelectric coefficient d_{zz}^{eff} in near-stoichiometric $NaNbO_3$ films and $((NaNbO_3)_x/(K_{0.5}Na_{0.5}NbO_3)_y$ superlattices. In addition, it would be worthwhile to systematically investigate the influence of superlattice periodicity or stack thickness and incorporated lattice strain on the piezoelectric coefficient d_{zz}^{eff}. Among others, segregation effects, interface diffusion and prevention of off-stoichiometry have to be studied in detail, in order to optimize the proposed vertical test structures. However, alkali niobates in thin film form are largely unknown. Due to the high reactivity of alkali metals, several top and bottom contact materials have to be tested in order to establish a suitable capacitor structure. Finally, it would be desirable to have a better understanding of the domains in strained films and the contribution of domain walls, in particular for enhancing the piezoelectric material properties.

Bibliography

[1] A. I. Kingon, J.-P. Maria, and S. K. Streiffer, "Alternative dielectrics to silicon dioxide for memory and logic devices", *Nature*, vol. 406, pp. 1032-1038, 2000.

[2] G. H. Haertling, “Ferroelectric ceramics: History and technology,” *Journal of the American Ceramic Society*, vol. 82, pp. 797-818, 1999.

[3] J.-H. Park, E. Vescovo, H-J. Kim, C. Kwon, R. Ramesh, and T. Venkatesan, "Magnetic properties at surface boundary of a half-metallic ferromagnet La 0.7 Sr 0.3 MnO 3", *Physical review letters*, vol. 81, p. 1953, 1998.

[4] A. S. Bhalla, R. Guo, and R. Roy, "The perovskite structure–a review of its role in ceramic science and technology", *Material Research Innovations*, vol. 4, pp. 3-26, 2000.

[5] Y. Uematsu, "Nonlinear optical properties of KNbO3 single crystal in the orthorhombic phase", *Japanese Journal of Applied Physics*, vol. 13, p. 1362, 1974.

[6] R. Ramesh and N. A. Spaldin, "Multiferroics: progress and prospects in thin films", *Nature materials*, vol. 6, pp. 21-29, 2007.

[7] A. Ohtomo and H. Y. Hwang, "A high-mobility electron gas at the LaAlO3/SrTiO3 heterointerface", *Nature*, vol. 427, pp. 423-426, 2004.

[8] D. G. Schlom, L. Q. Chen, C. B. Eom, K. M. Rabe, S. K. Streiffer, and J. M. Triscone, “Strain tuning of ferroelectric thin films,” *Annual Review of Materials Research*, vol. 37, pp. 589–626, 2007.

[9] J. H. Haeni et al., "Room-temperature ferroelectricity in strained SrTiO3", *Nature*, vol. 430, pp. 758-761, 2004.

[10] H. Qin, J. Zhu, Z. Jin, and Y. Wang, "Oriented growth in PZT thin films", *Integrated Ferroelectrics*, vol. 30, pp. 175-182, 2000.

[11] S.-B. Jung and S.-W. Kim, "Improvement of scanning accuracy of PZT piezoelectric actuators by feed-forward model-reference control", *Precision Engineering*, vol. 16, pp. 49-55, 1994.

[12] Wang, Qing-Ming, Tao Zhang, Qingming Chen, and Xiao-Hong Du, "Effect of DC bias field on the complex materials coefficients of piezoelectric resonators." *Sensors and Actuators A: Physical*, vol. 109, pp. 149-155, 2003.

[13] R. E. Newnham, L. J. Bowen, K. A. Klicker, and L. E. Cross, "Composite piezoelectric transducers", *Materials & Design*, vol. 2, pp. 93-106, 1980.

[14] B. H. Park, B. S. Kang, S. D. Bu, T. W. Noh, J. Lee, and W. Jo, "Lanthanum-substituted bismuth titanate for use in non-volatile memories", *Nature*, vol. 401, pp. 682-684, 1999.

[15] N. Izyumskaya, Y. Alivov, S. J. Cho, H. Morkoc, H. Lee, and Y. S. Kang, "Processing, structure, properties, and applications of PZT thin films", *Critical reviews in solid state and materials sciences*, vol. 32, pp. 111-202, 2007.

[16] E. Aksel and J. L. Jones, "Advances in lead-free piezoelectric materials for sensors and actuators", *Sensors*, vol. 10, pp. 1935-1954, 2010.

[17] M. Brazier, S. Mansour, and M. McElfresh, "Ferroelectric fatigue of Pb (Zr, Ti) O 3 thin films measured in atmospheres of varying oxygen concentration", *Applied physics letters*, vol. 74, pp. 4032-4033, 1999.

[18] M. D. Losego and J. P. Maria, "Reproducibility and ferroelectric fatigue of lead zirconate titanate thin films deposited directly on copper via a composite gel architecture", *Journal of the American Ceramic Society*, vol. 93, pp. 3983-3985, 2010.

[19] T. Zhao, Z.H. Chen, F. Chen, H.B. Lu, G.Z. Yang,and H.S. Cheng, "Electrical and optical properties of strongly reduced epitaxial BaTiO3−x thin films", *Applied Physics Letters*, vol. 77, pp. 4338-4340, 2000.

[20] K. J. Choi et al., "Enhancement of ferroelectricity in strained BaTiO3 thin films", *Science*, vol. 306, pp. 1005-1009, 2004.

[21] X. Du, J. Zheng, U. Belegundu, and K. Uchino, "Crystal orientation dependence of piezoelectric properties of lead zirconate titanate near the morphotropic phase boundary", *Applied physics letters*, vol. 72, pp. 2421-2423, 1998.

[22] L. Egerton and D. M. Dillon, "Piezoelectric and dielectric properties of ceramics in the system potassium—sodium niobate", *Journal of the American Ceramic Society*, vol. 42, pp. 438-442, 1959.

[23] A. Duk, M. Schmidbauer, and J. Schwarzkopf, "Anisotropic one-dimensional domain pattern in NaNbO3 epitaxial thin films grown on (110) TbScO3", *Applied Physics Letters*, vol. 102, p. 091903, 2013.

[24] J. S. Speck, A. Seifert, W. Pompe, and R. Ramesh, “Domain configurations due to multiple misfit relaxation mechanisms in epitaxial ferroelectric thin films. II. Experimental verification and implications”, *Journal of Applied Physics*, vol. 76, pp. 477-483, 1994.

[25] L. Brewer and J. Margrave, "The vapor pressures of lithium and sodium oxides", *The Journal of Physical Chemistry*, vol. 59, pp. 421-425, 1955.

[26] C.-H. Lee et al., "Exploiting dimensionality and defect mitigation to create tunable microwave dielectrics", *Nature*, vol. 502, pp. 532-536, 2013.

[27] G. Shirane, R. Newnham, and R. Pepinsky, "Dielectric Properties and Phase Transitions of NaNb O 3 and (Na, K) Nb O 3", *Physical Review*, vol. 96, p. 581, 1954.

[28] R. E. Jaeger and L. Egerton, "Hot Pressing of Potassium-Sodium Niobates", *Journal of the American Ceramic Society*, vol. 45, pp. 209-213, 1962.

[29] L. Hong, P. Wu, Y Li, V. Gopalan, C.-B. Eom, D. G. Schlom, and L.-Q. Chen, "Piezoelectric enhancement of (PbTiO3)m/(BaTiO3)n ferroelectric superlattices through domain engineering", *Physical Review B*, vol. 90, p. 174111, 2014.

[30] V. M. Goldschmidt, “Die Gesetze der Krystallochemie”, *Die Naturwissenschaften*, vol.14, no 21, pp. 477-485, 1926.

[31] C. A. Randall, A. S. Bhalla, T. R. Shrout, and L. E. Cross, “Classification and consequences of complex lead perovskite ferroelectrics with regard to B-site cation order”, *Journal of Materials Research*, vol. 5, pp. 829-834, 1990.

[32] J. Tellier, B. Malic, B. Dkhil, D. Jenko, J. Cilensek, and M. Kosec, “Crystal structure and phase transitions of sodium potassium niobate perovskites”, *Solid State Sciences*, vol. 11, pp. 320 – 324, 2009.

[33] R. Orlando, http://www.theochem.unito.it, December 2014.

[34] M. W. Lufaso, and P. M. Woodward, “Prediction of the crystal structures of perovskites using the software program SPuDS”, *Acta Crystallographica Section B*, vol. 57, pp. 725-738, 2001.

[35] A. M. Glazer, “The classification of Tilted Octahedra in Perovskites”, *Acta Crystallographica Section B*, vol. 28, pp. 3384-3392, 1972.

[36] M. Athee and A. M. Glazer, “Lattice parameters and tilted octahedra in sodium_potassium niobate solid solutions”, *Acta Crystallographica Section A*, vol. 32, p. 434, 1976.

[37] J. G. Webster (Ed.), *The Measurement, Instrumentation, and Sensors handbook*, ISBN 978-0-8493-8347-2, CRC Press/IEEE Press, Boca Raton, pp. 32–113, 1999.

[38] A. Duk, “Relationships between strain, ferro- and piezoelectric properties in functional oxide thin films” Ph.D. dissertation, 2013.

[39] C. Kittel, *Introduction to Solid State Physics*, 8th ed. Wiley, 2005.

[40] D. Damjanovic, “Ferroelectric, dielectric and piezoelectric properties of ferroelectric thin films and ceramics,” *Reports on Progress in Physics*, vol. 61, no. 9, pp. 1267–1324, 1998.

[41] M. E. Lines, and A. M. Glass, *Principles and applications of ferroelectrics and related materials*, Oxford University Press, 1977.

[42] Philippe Ghosez and Javier Junquera, Chapter 134: First-Principles modeling of ferroelectric oxides nanostructures, in: *Handbook of theoretical and computational nanotechnology*, M. Rieth and W. Schommers (Ed.), American Scientific Publisher (Stevenson Ranch, CA, USA), 2006.

[43] M. Schmidbauer, J. Sellmann, D. Braun, A. Kwasniewski, A. Duk, and J. Schwarzkopf, „Ferroelectric domain structure of NaNbO3 epitaxial thin films grown on (110) DyScO3 substrates”, *Physica Status Solidi RRL*, pp. 1–5, 2014.

[44] J. S. Speck, and W. Pompe, “Domain configurations due to multiple misfit relaxation mechanisms in epitaxial ferroelectric thin films. I. Theory”, *Journal of Applied Physics*, vol. 76, pp. 466-476, 1994.

[45] G. Sheng, J. X. Zhang, Y. L. Li, S. Choudhury, Q. X. Jia, Z. K. Liu, and L. Q. Chen, “Domain stability of $PbTiO_3$ thin films under anisotropic misfit strains: Phase-field simulations”, *Journal of Applied Physics*, vol 104, p. 054105, 2008.

[46] N. A. Pertsev and A. G. Zembilgotov, “Energetics and geometry of 90° domain structures in epitaxial ferroelectric and ferroelastic films,” *Journal of Applied Physics*, vol. 78, no. 10, p. 6170, 1995.

[47] D. Landau and E. Lifshits, “On the theory of the dispersion of magnetic permeability in ferromagnetic bodies,” *Physikalische Zeitschrift der Sowjetunion*, vol. 8, pp. 156–169, 1935.

[48] C. Kittel, *The Physical Review*, vol. 70, p. 965, 1946.

[49] G. Catalan, J. Seidel, R. Ramesh, and J. F. Scott, “Domain wall nanoelectronics,” *Reviews of Modern Physics*, vol. 84, no. 1, pp. 119–156, 2012.

[50] A. H. G. Vlooswijk, B. Noheda, G. Catalan, A. Janssens, B. Barcones, G. Rijnders, D. H. A. Blank, S. Venkatesan, B. Kooi, and J. T. M. de Hosson, “Smallest 90° domains in epitaxial ferroelectric films,” *Applied Physics Letters*, vol. 91, no. 11, p. 112901, 2007.

[51] J. Valasek, “Piezo-electric and allied phenomena in Rochelle salt.” *Physical Review*, vol. 17, no. 4, pp. 475–481, 1921.

[52] A. von Hippel (Ed.), *Dielectric Materials and Applications*, ISBN 0-89006-805-4, Artech House, London, 1954.

[53] J. F. Scott, *Ferroelectric Memories*, ISBN 978-3-662-04307-3, Springer, 2000.

[54] B. Ravel, E. A. Stern, R. I. Vedrinskii, and V. Kraizman, “Local structure and the phase transitions of $BaTiO_3$“, *Ferroelectrics*, vols. 206-207, pp. 407-430, 1998.

[55] G. Rijnders and D. H. A. Blank, Growth kinetics during pulsed laser deposition, in: *Pulsed Laser Deposition of Thin Films: Applications-Led Growth of Functional Materials*, pp. 177-190, R. Eason (Ed), Wiley-Interscience, Hoboken, New Jersey, 2007.

[56] J. A. Venables, “Atomic processes in crystal growth”, *Surface Science*, vols. 299-300, pp. 798-817, 1994.

[57] J. A. Venables, “Nucleation and growth processes in thin film formation”, *Journal of Vacuum Science and Technology B*, Vol. 4, pp. 870-873, 1986.

[58] A. Pimpinelli, and J, Villain, *Physics of Crystal Growth*, Cambridge University Press, 1998.

[59] J. W. Matthews, and A. E. Blakeslee, “Defects in epitaxial multilayers: I. Misfit dislocations”, *Journal of Crystal Growth*, vol. 27, pp. 118-125, 1974.

[60] M. D. Biegalski, *Epitaxially Strained Strontium Titanate*, ISBN: 0549689664, 9780549689669, Pro Quest, 2006.

[61] J. W. Matthews, S. Mader, T. B. Light, “Accomodation of Misfit Across the Interface Between Crystals of Semiconducting Elements or Compounds”, *Journal of Applied Physics*, vol. 41, pp. 3800-3804, 1970.

[62] G. Cohen-Solal, F. Bailly, and M. Barbé, “Critical thickness in heteroepitaxial growth of zinc-blende semiconductor compounds”, *Journal of Crystal Growth*, vol. 138, pp. 68-74, 1994.

[63] R. Uecker, B. Velickov, D. Klimm, R. Bertram, M. Bernhagen, M. Rabe, M. Albrecht, R. Fornari, and D. G. Schlom, “Properties of rare-earth scandate single crystals (RE=ND-Dy)”, *Journal of Crystal Growth*, vol. 310, pp. 2649-2658, 2008.

[64] J. F. Nye, *Physical Properties of Crystals*, Clarendon Press, Oxford, 1957.

[65] R. L. Dirsyte, J. Schwarzkopf, M. Schmidbauer, G. Wagner, K. Irmscher, S. Bin Anooz, and R. Fornari, “Impact of epitaxial strain on the ferromagnetic transition temperature of SrRuO3 thin films”, *Thin Solid Films*, vol. 519, pp. 6264-6268, 2011.

[66] G. N. Greaves, A. L. Greer, R. S. Lakes, and T. Rouxel, “Poisson’s ratio and modern materials”, *Nature Materials*, vol. 10, pp. 823–837, 2011.

[67] M. Zgonik, R. Schlesser, I. Biaggio, E. Voit, J. Tscherry, and P. Günter, “Materials constants of knbo3 relevant for electro- and acousto-optics”, *Journal of Applied Physics*, vol. 74(2), pp. 1287–1297, 1993.

[68] L. D. Landau, and E. M. Lifschitz, *Course on Theoretical Physics*, Vol. VII, Pergamon Press, New York, 1985.

[69] A. D. Akhsakhalyan, Yu. A. Bityurin, S. V. Gaponov, A. A. Gudkov, and V. I. Luchin, "processes occuring in an erosion plasma during laser vacuum deposition of films. I. Properties of a laser erosion plasma in the inertial-expansion state", *Soviet Physics - Technical Physics*, vol. 27, pp. 969-973, 1982.

[70] D. B. Chrisey and G. K. Hubler (Eds.), *Pulsed Laser Deposition of Thin Films*, John Wiley and Sons, Inc., New York, 1994.

[71] R. Eason (Ed.), *Pulsed Laser Deposition Of Thin Films*, Wiley-Interscience, Hoboken, New Jersey, pp. 177-190, 2007.

[72] M. Lorenz and M. S. R. Rao (Eds.), “25 years of pulsed laser deposition", *Journal of Physics D: Applied Physics*, vol. 47, 2014.

[73] S. I. Anisimov, B. S. Luk’yanchuk, and A. Luches, "An analytical model for three dimensional laser plume expansion into vacuum in hydrodynamic regime", *Applied Surface Science*, vol. 96-98, pp. 24-32, 1996

[74] D. B. Geohegan, "Physics and diagnostics of laser ablation plume propagation for high-Tc superconductor film growth", *Thin Solid Films*, vol. 220, pp. 138-145, 1992.

[75] W. Demtröder, *Experimentalphysik 1: Mechanik und Wärme*, ISBN 978-3540260349, Springer, Berlin Heidelberg New York.

[76] C. Cho and A. Grishin, "Self-assembling ferroelectric Na0.5K0.5NbO3 thin films by pulsed laser deposition", *Applied Physics Letters*, vol 75, pp. 268-270, 1999.

[77] J. G. E. Gardeniers, Z. M. Rittersma, and G. J. Burger, "Preferred orientation and piezoelectricity in sputtered ZnO films", *Journal of Applied Physics*, vol. 83, 7844-7854, 1998.

[78] D. B. Geohegan, "Fast intensified-CCD photography of YBa2CuO3O7 - x laser ablation in vacuum and ambient oxygen", *Applied Physics Letters*, vol. 60, pp. 2732-2734, 1992.

[79] Gonzalo, C. N. Afonso, and I. Madariaga, "Expansion dynamics of the plasma produced by laser ablation of BaTiO3 in a gas environment", *Journal of Applied Physics*, vol. 81, pp. 951-955, 1997.

[80] B. Y. Man, X. T. Wang, and A. H. Liu, "Transport of plasmas produced by pulsed laser ablation of HgCdTe", *Journal of Applied Physics*, vol. 83, pp. 3509-3513, 1998.

[81] C. Cho and A. Grishin, "Background oxygen effects on pulsed laser deposited Na0.5K0.5NbO3 films: From superparaelectric state to ferroelectricity", *Journal of Applied Physics*, vol. 87, pp., 4439-4448, 2000.

[82] B. Dam, J. H. Rector, J. Johansson, S. Kars, R. Griessen, "Stoichiometric transfer of complex oxides by pulsed laser deposition", *Applied Surface Science*, vol. 96-98, pp. 679-684, 1996.

[83] M. L. Scullin, C. Yu, M. Huijben, S. Mukerjee, J. Seidel, Q. Zhan, J. Moore, A. Majumdar, and R. Ramesh, "Anomalously large measured thermoelectric power factor in Sr 1-x La x TiO3 thin films due to SrTiO3 substrate reduction", *Applied Physics Letters*, vol. 92, p. 202113, 2008.

[84] E. Hotston, "Threshold energies for sputtering", *Nuclear Fusion*, vol. 15, pp. 544-547, 1975.

[85] S. Chapman and T. G. Cowling, *The Mathematical Theory of Non-uniform Gases: An Account of the Kinetic Theory of Viscosity, Thermal Conduction and Diffusion in Gases*, ISBN: 052140844X, 9780521408448, Cambridge University Press, 1970.

[86] H. Gregory and S. Marshall, "The Thermal Conductivities of Oxygen and Nitrogen", *Proceedings of the Royal Society of London Series A*, vol. 118, pp. 594-607, 1928.

[87] K. Sturm and H. U. Krebs, "Quantification of resputtering during pulsed laser deposition", *Journal of Applied Physics*, vol. 90, pp. 1061-1063, 2001.

[88] D. J. Keeble, S. Wicklein, R. Dittmann, L. Ravelli, R. A. Mackie, and W. Egger, "Identification of A- and B-Site Cation Vacancy Defects in Perovskite Oxide Thin Films", *Physical Review Letters*, vol. 105, p. 226102, 2010.

[89] T. Ohnishi, K. Shibuya, T. Yamamoto, and M. Lippmaa, "Defects and transport in complex oxide thin films", *Journal of Applied Physics*, vol. 103, p. 103703, 2008.

[90] T. Venkatesan, X. D. Wu, A. Inam, and J. B. Wachtman, "Observation of two distinct components during pulsed laser deposition of high Tc superconducting films", *Applied Physics Letters*, vol. 52, p. 1193, 1998.

[91] J. A. Greer, and M. D. Tabat, "Large-area pulsed laser deposition: Techniques and applications", *Journal of Vaccum Sience and Technology A*, vol. 13, pp. 1175-1181, 1995.

[92] M. Lorenz, H. Hochmuth, D. Natusch, M. Kusunoki, V. L. Svetchnikov, V. Riede, I. Stanca, G. Kästner, and D. Hesse, "High-quality Y-Ba-Cu-O Thin Films by PLD – Ready for Market Applications", *Applied Superconductivity, IEEE Transactions on*, vol. 11, pp. 3209-3212, 2001.

[93] J. T. Cheung in: *Pulsed Laser Deposition of thin films*, D. B. Chrisey, and G. K. Hubler (Eds.), John Wiley & Sons, Inc. New York, 1994.

[94] I. Bozovic, J. N. Eckstein, N. Bozovic, "Reflection High-Energy Electron Diffraction as a Tool for Real-Time Characterization of Growth of Complex Oxides", in: *In Situ Process Diagnostics and Intelligent Materials Processing*, O. Auciello and A.R. Krauss (Eds.), Wiley Science, 2000.

[95] M. Lippmaa, N. Nakagawa, M. Kawasaki, S. Ohashi, Y. Inaguma, M. Itoh, and H. Koinuma, "Step-flow growth of SrTiO3 thin films with a dielectric constant exceeding 104", *Applied Physics Letters*, vol. 74, p. 3543, 1999.

[96] G. Koster, J. H. M. Rijnders, D. H. A. Blank, and H. Rogalla, "Imposed layer-by-layer growth by physical laser interval deposition", *Applied Physics Letters*, vol. 74, p. 3729, 1999.

[97] Department of Metallurgy, Materials Science and Materials Procesing, Graduate School of Engineering, Tohoku University, http://www.material.tohoku.ac.jp/~kaimenb/B_RHEED.html, December 2014.

[98] G. Binnig, C. F. Quate, and Ch. Gerber, "Atomic Force Microscopy", *Physical Review Letters*, vol. 56, p. 930, 1986.

[99] S. Jesse, A. P. Baddorf, and S. V. Kalinin, “Dynamic behaviour in piezoresponse force microscopy,” *Nanotechnology*, vol. 17, no. 6, pp. 1615–1628, 2006.

[100] A. Kholkin, S. Kalinin, A. Roelofs, and A. Gruverman, “Review of ferroelectric domain imaging by piezoresponse force microscopy”, in: *Scanning Probe microscopy*, S. Kalinin, A. Gruverman (Eds.), ISBN: 978-0-387-28667-9, Springer, New York, 2007.

[101] M. Laue, Röntgenstrahlinterferenzen, *Akademie Verlag*, Berlin 1962.

[102] U. Pietsch, V. Holy, and T. Baumbach, *High-Resolution X-Ray Scattering - From Thin Films to Lateral Nanostructures*, ISBN 0-387-40092-3, Springer, New York, 2004.

[103] data sheet 00-046-1045, International Centre for Diffraction Data.

[104] L. Spieß, R. Schwarzer, H. Behnken, and G. Teichert, *Moderne Röntgenbeugung - Röntgendiffraktometrie für Materialwissenschaftler, Physiker und Chemiker*, ISBN 3-519-00522-0, Teubner, Wiesbaden 2005.

[105] M. Schmidbauer, *X-Ray Diffuse Scattering from Self-Organized Mesoscopic Semiconductor Structures*. Springer Tracts in Modern Physics, ISBN 3-540-20179-3, Springer, Berlin, Heidelberg, 2004.

[106] M. Schmidbauer, P. Schäfer, S. Besedin, D. Grigoriev , R. Köhler, M. Hanke, A novel multi-detection technique for three-dimensional reciprocal-space mapping in grazing-incidence X-ray diffraction, *Journal of Synchrotron Radiation*, vol. 15, pp. 549-557, 2008.

[107] D. Ligny and P. Richet, "High-temperature heat capacity and thermal expansion of SrTiO3 and SrZrO3 perovskites", *Physical Review B*, vol. 53, p. 3013, 1996.

[108] G. Koster, B.L. Kropman, G.J.H.M. Rijnders, D.H.A. Blank, and H. Rogalla, "Quasi-ideal strontium titanate crystal surfaces through formation of strontium hydroxide", *Applied Physics Letters*, vol. 73, p. 2920, 1998.

[109] M. R. Castell, "Scanning tunneling microscopy of reconstructions on the SrTiO3 (001) surface", *Surface Science*, vol. 505, pp. 1-13, 2002.

[110] T. Nishimura, A. Ikeda, H. Namba, T. Morishita, and Y. Kido, "Structure change of TiO2-terminated SrTiO3 (001) surfaces by anealing in O2 atmosphere and ultrahigh vacuum", *Surface Science*, vol. 421, pp. 273-278, 1999.

[111] A. Vailionis, H. Boschker, W. Siemons, E. P. Houwman, D. H. A. Blank, G. Rijnders, and G. Koster, "Misfit strain accommodation in epitaxial ABO3 perovskites: Lattice rotations and lattice modulations", *Physical Review B*, vol. 83, pp. 064101-064111, 2011.

[112] R. L. Dirsyte, J. Schwarzkopf, G. Wagner, J. Lienemann, M. Busch, H. Winter, and R. Fornari, "Surface termination of NdGaO3 (110)", *Applied Surface Science*, vol. 225, pp. 8685-8687, 2009.

[113] R. L. Dirsyte, "Liquid-Delivery Metal-Organic Chemical Vapour Deposition of Perovskites and Perovskite-Like Compounds", PhD Thesis, 2010.

[114] M. Schmidbauer, A. Kwasniewski, and J. Schwarzkopf, "High-precision absolute lattice parameter determination of SrTiO3, DyScO3 and NdGaO3 single crystals", *Acta Crystallographica B*, vol. 68, pp. 8-14, 2012.

[115] R. Uecker, B. Velickov, D. Klimm, R. Bertram, M. Bernhagen, M. Rabe, M. Albrecht, R. Fornari, D. G. Schlom, "Properties of rare-earth scandate single crystals (Re=Nd−Dy)", *Journal of Crystal Growth*, vol. 310, pp. 2649-2658, 2008.

[116] M. C. Morris, H. F. McMurdie, E. H. Evans, B. Paretzkin, H. S. Parker, N. C. Panagiotopoulos, and C. R. Hubbard, *Standard X-ray Diffraction Powder Patterns*, NBS Monograph, Section 18, Data for 58 Substances, National Bureau of Standards, Gaithersburg, p. 64, 1981.

[117] A.M. Glazer and H.D. Megaw, “Studies of the lattice parameters and domains in the phase transitions of NaNbO3”, *Acta Crystallographica A*, vol. 29, p. 489, 1973.

[118] H. D. Megaw, "The seven phases of NaNbO3", *Ferroelectrics*, vol. 7, p. 87, 1974.

[119] Yu. I. Yuzyuk, E. Gagarina, P. Simon, L. A. Reznitchenko, L. Hennet, and D. Thiaudiere, "Synchrotron x-ray diffraction and Raman scattering investigations of (LixNa1-x)NbO3 solid solutions: Evidence of the rhombohedral phase", *Physical Review B*, vol. 69, pp. 144105-144112, 2004.

[120] J. Dec, "Real domain structure in orthorhombic phase of NaNbO3 crystals", *Crystal Research & Technology*, vol. 18, pp. 195-204, 1983.

[121] A. Torres-Pardo, R. Jiménez, J. M. González-Calbet, and E. García-González, "Room Temperature Ferroelectricity in Na1−xSrx/2x/2NbO3 through the Introduction of Cationic Vacancies", *Chemical Materials*, vol. 20, pp. 6957-6964, 2008.

[122] C. N. W. Darlington, PhD Thesis, 1971.

[123] A. C. Sakowski-Cowley, K. Lukaszewicz, and H. D. Megaw, "The structure of sodium niobate at room temperature, and the problem of reliability in pseudosymmetric structures." *Acta Crystallographica Section B*, vol. 25, pp. 851-865, 1969.

[124] M. Ahtee, A. M. Glazer, and H. D. Megaw, "The structures of sodium niobate between 480° and 575° C, and their relevance to soft-phonon modes", *Philosophical Magazine*, vol. 26, pp. 995-1014, 1972.

[125] A. M. Glazer and Helen D. Megaw, "The structure of sodium niobate (T2) at 600° C, and the cubic-tetragonal transition in relation to soft-phonon modes", *Philosophical Magazine*, vol. 25, pp. 1119-1135, 1972.

[126] S. Yamazoe, A. Kohori, H. Sakurai, Y. Kitanaka, Y. Noguchi, M. Miyayama, and T. Wada, "Laser beam scanning microscope and piezoresponse force microscope studies on domain structured in 001-, 110-, and 111-oriented NaNbO3 films." *Journal of Applied Physics*, vol. 112, p. 052007, 2012.

[127] W. J. Maeng, I. Jung, and J. Y. Son, "Enhanced ferroelectric polarization in tetragonally strained NaNbO3 thin film on single crystal Rh substrate", *Journal of Crystal Growth*, vol. 349, pp. 24-26, 2012.

[128] J. Schwarzkopf, M. Schmidbauer, T. Remmele, A. Duk, A. Kwasniewski, S. Bin Anooz, A. Devi, and R. Fornari, “Strain-induced phase transitions in epitaxial NaNbO3 thin films grown by metal-organic chemical vapour deposition." *Journal of Applied Crystallography*, vol. 45, pp. 1015-1023, 2012.

[129] R. Wördenweber, J. Schwarzkopf, E. Hollmann, A. Duk, B. Cai, and M. Schmidbauer, "Impact of compressive in-plane strain on the ferroelectric properties of epitaxial NaNbO3 films on (110) NdGaO3", *Applied Physics Letters*, vol. 103, p. 132908, 2013.

[130] S. D. Phatak, R. C. Srivastava, and E. C. Subbarao, "Elastic constants of orthorhombic KNbO3 by X-ray diffuse scattering", *Acta Crystallographica Section A*, vol. 28, pp. 227-231, 1972.

[131] G. Shirane, H. Danner, A. Pavlovic, and R. Pepinsky, "Phase Transitions in Ferroelectric KNb O 3", *Physical Review*, vol. 93, p. 672, 1954.

[132] M. Ahtee, and A. W. Hewat, "Structural phase transitions in sodium-potassium niobate solid solutions by neutron powder diffraction", *Acta Crystallographica Section A*, vol. 34, pp. 309-317, 1978.

[133] D. W. Baker, D. William, P. A. Thomas, N. Zhang, and A. M. Glazer, "A comprehensive study of the phase diagram of K x Na 1-x NbO 3", *Applied Physics Letters*, vol. 95, pp. 091903-091903, 2009.

[134] A. Muhtar, M. Somayazulu, R. E. Cohen, P. Ganesh, P. Dera, H. Mao, R. J. Hemley, Y. Ren, P. Liermann, and Z. Wu, "Origin of morphotrophic phase boundaries in ferroelectrics", *Nature*, vol. 451, pp. 545-548, 2008.

[135] L. Wu, J. L. Zhang, C. L. Wang, and J. C. Li, "Influence of compositional ratio K/Na on physical properties in (K x Na 1-x) NbO 3 ceramics", *Journal of Applied Physics*, vol. 103, pp. 084116-084116, 2008.

[136] S. Yamazoe, K. Shibata, K. Kato, and T. Wada, "Needle-like NaNbO3 Synthesis via Nb6O198- Cluster Using Na3NbO4 Precursor by Dissolution-Precipitation Method", *Chemical Letters*, vol. 42, pp. 380-382, 2013.

[137] B. P. Burton and T. Nishimatsu, "First principles phase diagram calculations for the system NaNbO 3–KNbO 3: Can spinodal decomposition generate relaxor ferroelectricity?", *Applied Physics Letters*, vol. 91, pp. 092907-092907, 2007.

[138] T. Schober and R. W. Balluffi, "Quantitative observation of misfit dislocation arrays in low and high angle twist grain boundaries", *Philosophical magazine*, vol. 21, pp. 109-123, 1970.

[139] P. Gaunt, "Ferromagnetic domain wall pinning by a random array of inhomogeneities", *Philosophical Magazine B*, vol. 48, pp. 261-276, 1983.

[140] M. Tyunina, D. Chvostova, O. Pacherova, T. Kocourek, M. Jelinek, L. Jastrabik, and A. Dejneka, “Ambience-sensitive optical refraction in ferroelectric nanofilms of NaNbO3”, *Science and Technology of Advanced Materials*, vol. 15, p. 045001, 2014.

[141] J. Sellmann, J. Schwarzkopf, A. Kwasniewski, M. Schmidbauer, D. Braun, and A. Duk, "Strained ferroelectric NaNbO3 thin films: Impact of pulsed laser deposition growth conditions on structural properties", *Thin Solid Films*, vol. 570, pp. 107-113, 2014.

[142] G. Niu, B. Gautier, S. Yin, G. Saint-Girons, P. Lecoeur, V. Pillard, G. Hollinger, and B. Vilquin, “Molecular Beam Epitaxy growth of BaTiO3 thin films and crucial impact of oxygen content conditions on the electrical characteristics”, *Thin Solid Films*, vol. 520, pp. 4595-4599, 2012.

[143] J. F. Ihlefeld et al., "Optical band gap of BiFeO 3 grown by molecular-beam epitaxy", *Applied Physics Letters*, vol. 92, pp. 142908-142908, 2008.

[144] G. Catalan, M. H. Corbett, R. M. Bowman, J. M. Gregg, "Influence of oxygen content on dielectric and electromechanical properties of Pb(Mg1/3Nb2/3)O3 thin films", *Applied Physics Letters*, vol. 74, pp. 3035-3037, 1999.

[145] C. Wang, B.L. Cheng, S.Y. Wang, H.B. Lu, Y.L. Zhou, Z.H. Chen, and G.Z. Yang, "Effects of oxygen pressure on lattice parameter, orientation, surface morphology and deposition rate of (Ba0.02Sr0.98)TiO3 thin films grown on MgO substrate by pulsed laser deposition," *Thin Solid Films*, vol. 485, pp. 82-89, 2005.

[146] T. Zhao, Z.H. Chen, F. Chen, H.B. Lu, G.Z. Yang, and H.S. Cheng, "Electrical and optical properties of strongly reduced epitaxial BaTiO3−x thin films", *Applied Physics Letters*, vol. 77, pp. 4338-4340, 2000.

[147] J. H. Rector, P. Koster, F. Peerdeman, D. G. de Groo, and B. Dam, "Twin-free YBa2Cu3O7−δ films on (001) NdGaO3 showing isotropic electrical behaviour", *Journal of Alloys and Compounds*, vol. 251, pp. 114-117, 1997.

[148] J. S. Horwitz, K. S. Grabowski, D. B. Chrisey, and R. E. Leuchtner, "In situ deposition of epitaxial PbZrxTi(1-x)O3 thin films by pulsed laser deposition", *Applied Physics Letters*, vol. 59, pp. 1565-1567, 1991.

[149] S. Estradé, J. M. Rebled, J. Arbiol, F. Peiró, I. C. Infante, G. Herranz, F. Sánchez, J. Fontcuberta, R. Córdoba, B. G. Mendis, and A. L. Bleloch, Effects of thickness on the cation segregation in epitaxial (001) and (110) La2/3Ca1/3MnO3 thin films." *Applied Physics Letters*, vol. 95, p. 072507, 2009.

[150] N. Nakagawa, H. Y. Hwang, and D. A. Muller, "Why some interfaces cannot be sharp", *Nature materials*, vol. 5, pp. 204-209, 2006.

[151] O. Nesterov, S. Matzen, C. Magen, A. H. G. Vlooswijk, G. Catalan, and B. Noheda, "Thickness scaling of ferroelastic domains in PbTiO3 films on DyScO3", *Applied Physics Letters*, vol. 103, p. 142901, 2013.

[152] T. Suzuki, Y. Nishi, and M. Fujimoto, “Analysis of misfit relaxation in heteroepitaxial BaTiO3 thin films”, *Philosophical Magazine A*, vol. 79, pp. 2461-2483, 1999.

[153] W. Pompe, X. Gong, Z. Suo, and J. S. Speck, “Elastic energy release due to domain formation in the strained epitaxy of ferroelectric and ferroelastic films,” *Journal of Applied Physics*, vol. 74, p. 6012, 1993.

[154] A. Roelofs, N. A. Pertsev, R. Waser, F. Schlaphof, L. M. Eng, C. Ganpule, V. Nagarajan, and R. Ramesh, “Depolarizing-field-mediated 180° switching in ferroelectric thin films with 90° domains”, *Applied Physics Letters*, vol. 80, pp. 1424-1426, 2002.

[155] J. Schwarzkopf, D. Braun, M. Schmidbauer, A. Duk, and R. Wördenweber, "Ferroelectric domain structure of anisotropically strained NaNbO3 epitaxial thin films", *Journal of Applied Physics*, vol. 115, p. 204105, 2014.

[156] L. Feigl, L. J. McGilly, and N. Setter, "Superdomain Structure in Epitaxial Tetragonal PZT Thin Films Under Tensile Strain", *Ferroelectrics*, vol. 465, pp. 36-43, 2014.

[157] H. Béa and P. Paruch, "Multiferroics: a way foward along domain walls", *Nature Materials*, vol. 8, p. 168, 2009.

[158] J. Seidel et al., "Conduction at domain walls in oxide multiferroics." *Nature materials*, vol. 8, pp. 229-234, 2009.

[159] J. Guyonnet, I. Gaponenko, S. Gariglio, and P. Paruch, "Conduction at Domain Walls in Insulating Pb(Zr0.2Ti0.8)O3 Thin Films", *Advanced Materials*, vol. 23, pp. 5377–5382, 2011.

[160] J. Seidel et al., "Domain wall conductivity in La-doped BiFeO 3", *Physical review letters*, vol. 105, p. 197603, 2010.

[161] G. Catalan, A. Janssens, G. Rispens, S. Csiszar, O. Seeck, G. Rijnders, D. H. A. Blank, and B. Noheda, “Polar Domains in Lead Titanate Films under Tensile Strain”, *Physical Review Letters*, vol. 96, p. 127602, 2006.

[162] O. Diéguez, K. M. Rabe, and D. Vanderbilt, “First-principles study of epitaxial strain in perovskites”, *Physical Review B*, vol. 72, pp. 144101-144110, 2005.

[163] J. S. Speck, A. C. Daykin, A. Seifert, A. E. Romanov, and W. Pompe, "Domain configurations due to multiple misfit relaxation mechanisms in epitaxial ferroelectric thin films. III. Interfacial defects and domain misorientations", *Journal of applied physics*, vol. 78, pp. 1696-1706, 1995.

[164] T. Ishihara, J. A. Kilner, M. Honda, N. Sakai, H. Yokokawa, and Y. Takita, “Oxygen surface exchange and diffusion in LaGaO3 based perovskite type oxides”, *Solid State Ionics*, vols. 113–115, pp. 593–600, 1998.

[165] K. Kamiya, M. Y. Yang, S.-G. Park, B. Magyari-Köpe, Y. Nishi, M. Niwa, and K. Shiraishi, "ON-OFF switching mechanism of resistive–random–access–memories based on the formation and disruption of oxygen vacancy conducting channels", *Applied Physics Letters*, vol. 100, p. 073502, 2012.

[166] V. R. Palkar, J. John, and R. Pinto, “Observation of saturated polarization and dielectric anomaly in magnetoelectric BiFeO3 thin films”, *Applied Physics Letters*, vol. 80, p. 1628, 2002.

[167] K. Y. Yun, M. Noda, M. Okuyama, H. Saeki, H. Tabata, and K. Saito, ”Structural and multiferroic properties of BiFeO3 thin films at room Temperature”, *Journal of Applied Physics*, vol. 96, p. 3399, 2004.

[168] S. Aggarwal, S. Madhukar, B. Nagaraj, I. G. Jenkins, R. Ramesh, L. Boyer, and J. T. Evans, Jr., “Can lead nonstoichiometry influence ferroelectric properties of Pb„Zr,Ti…O3 thin films?”, *Applied Physics Letters*, vol. 75, p. 716, 1999.

[169] M. Abazari and A. Safari, "Leakage current behavior in lead-free ferroelectric (K, Na) NbO3-LiTaO3-LiSbO3 thin films", *Applied Physics Letters*, vol. 97, p. 262902, 2010.

[170] M. Abazari, and A. Safari, "Effects of doping on ferroelectric properties and leakage current behavior of KNN-LT-LS thin films on SrTiO 3 substrate", *Journal of Applied Physics*, vol. 105, pp. 094101-094101, 2009.

[171] N. T. Chua, L. You, J. Ma, and J. Wang, "Properties of (K, Na) NbO3-based lead-free piezoelectric films prepared by pulsed laser deposition", *Thin Solid Films*, vol. 518, pp. 6777-6780, 2010.

[172] T. Saito, H. Adachi, and T. Wada, "Pulsed laser deposition of ferroelectric (Na0.5K0.5)NbO3-based thin films", *Japanese journal of applied physics*, vol. 44, p. L573, 2005.

[173] A. Tian, W. Ren, L. Wang, P. Shi, X. Chen, X. Wu, and X. Yao, "Effect of deposition temperature on orientation and electrical properties of (K0. 5Na0. 5) NbO3 thin films by pulsed laser deposition", *Applied surface science*, vol. 258, pp. 2674-2678, 2012.

[174] E. D. Specht, H. M. Christen, D. P. Norton, and L. A. Boatner, "X-ray diffraction measurement of the effect of layer thickness on the ferroelectric transition in epitaxial KTaO 3/KNbO 3 multilayers", *Physical review letters*, vol. 80, p. 4317, 1998.

[175] H. M. Christen, E. D. Specht, D. P. Norton, M. F. Chisholm, and L. A. Boatner, "Long-range ferroelectric interactions in KTaO 3/KNbO 3 superlattice structures", *Applied physics letters*, vol. 72, pp. 2535-2537, 1998.

[176] Z. Li, T. Lü, and W. Cao, „Phase transition and ferroelectric properties of epitaxially strained KNbO3/NaNbO3 superlattice", *Journal of Applied Physics*, vol. 104, p. 126106, 2008.

[177] W. Hong et al., "Persistent step-flow growth of strained films on vicinal substrates", *Physical review letters*, vol. 95, p. 095501, 2005.

[178] R. C. L. Bosworth, "The Mobility of Sodium on Tungsten", Proceedings of the Royal Society of London A: Mathematical, *Physical and Engineering Sciences*, vol. 150, pp. 58-76, 1935.

[179] R. C. L. Bosworth, "The Mobility of Potassium on Tungsten", Proceedings of the Royal Society of London A: Mathematical, *Physical and Engineering Sciences*, vol. 154, pp. 112-123, 1936.

[180] S. H. Seo, H. C. Kang, H. W. Jang, and D. Y. Noh, "Effects of oxygen incorporation in tensile La0.84Sr0.16MnO3−δ thin films during ex situ annealing", *Physical Review B*, vol. 71, p. 012412, 2005.

[181] L. Goldstein et al., "Growth by molecular beam epitaxy and characterization of InAs/GaAs strainedlayer Superlattices", *Applied Physics Letters*, vol. 47, p. 1099, 1985.

[182] O. G. Vendik, E. K. Hollmann, A. B. Kozyrev, and A. M. Prudan, "Ferroelectric Tuning of Planar and Bulk Microwave Devices", *Journal of Superconductivity*, vol. 12, pp. 325-338, 1999.

[183] A. Chowdhury, J. Bould, M. GS Londesborough, and S. J. Milne, "The effect of refluxing on the alkoxide-based sodium potassium niobate sol–gel system: Thermal and spectroscopic studies", *Journal of Solid State Chemistry*, vol. 184, pp. 317-324, 2011.

[184] D. D. Fong, G. B. Stephenson, S. K. Streiffer, J. A. Eastman, O. Auciello, P. H. Fuoss, and C. Thompson, "Ferroelectricity in ultrathin perovskite films", *Science*, vol. 304, pp. 1650-1653, 2004.

[185] V. A. Stephanovich, I. A. Luk'yanchuk, and M. G. Karkut, „Domain-Enhanced Interlayer Coupling in Ferroelectric/Paraelectric Superlattices", *Physical Review Letters*, vol. 94, p. 047601, 2005.

[186] I. Kanno, S. Hayashi, R. Takayama, and T. Hirao, "Superlattices of PbZrO3 and PbTiO3 prepared by multi-ion-beam sputtering", *Applied physics letters*, vol. 68, 328-330, 1996.

[187] D. Bao, R. Scholz, M. Alexe, and D. Hesse, "Growth, microstructure, and ferroelectric properties of Pb (Zr0. 4Ti0. 6) O3⁄ PbZrO3 superlattices prepared on SrTiO3 (100) substrates by pulsed laser deposition", *Journal of Applied Physics*, vol. 101, p. 0541, 2007.

Acknowledgements

Without the help, kindness and support of many people, it would not have been possible to perform the research work presented in this thesis. To them, I am deeply grateful.

Prof. Dr. Roberto Fornari accepted me as a PhD student at the Leibniz-Institute for Crystal Growth. Prof. Dr.-Ing. Matthias Bickermann supervised this thesis and initiated regular meetings of the PhD students at the institute.

The head of the group of ferroelectric oxide thin films, Dr. Jutta Schwarzkopf, gave me the opportunity to work in the interesting field of functional oxide thin films. Her guidance and the many helpful discussions were invaluable.

My group colleagues, Sebastian Markschies and Michaela Klann, supplied comprehensive technical assistance, Dr. Andreas Duk and Dorothee Braun performed thorough investigations of the piezo/ferroelectric properties of the samples by PFM. Dr. Sonia Gnanapragasam and Philipp Müller prepared, measured, and analyzed numerous alkaline niobate TEM-samples with the support of Thilo Remmele, Toni Markurt and Dr. Martin Albrecht.

Albert Kwasniewski performed most of the XRD measurements. The important scientific discussions of those measurements with Dr. habil. Martin Schmidbauer allowed me to develop a deeper insight into the crystal structure of the films.

The oxides group of Dr. Reinhard Uecker supplied many of the high quality oxide substrates used in this work. In particular, I want to mention Andreas Tauchert for his introduction of the press and oven necessary for the fabrication of the targets and Rainer Bertram for the compositional analysis thereof.

Dr. Ricardo Pinedo Sanchez and the participants of the HZB-Summer school program, Ignat Moskalenko, Joana Fernandes and Asdrúbal Antonio Ramírez Botero greatly helped developing appropriate pressing and sintering routines for the fabrication of the PLD targets.

Dr. Klaus Irmscher and Mike Pietsch tested the electrical properties of samples and substrates.

Dr. habil. Detlef Klimm assisted this work with calculations of and discussions about the thermodynamic stability of alkaline oxides.

All persons mentioned and many more colleagues generated a warm, friendly and productive atmosphere in this institute and particularly in the group of ferroelectric oxide thin films. The flexibility and support given by the head of my group and my colleagues was fundamental for taking as large a part in the early life of my two wonderful children Jasper and Jule as I could have possibly hoped.

I would like to thank Dr. Helena Franke, Dr. Martin Bock, Lars Hartmann and Frank Tool for diligent proofreading of this thesis.

I am deeply grateful to my family and friends, whose kindness and support in the last years was invaluable. Most of all I thank Bente Hansen for her patience, trust and encouragement to pursue this work.

Selbstständigkeitserklärung

Hiermit erkläre ich, dass ich die vorliegende Arbeit selbstständig verfasst und nur die angegebene Literatur und Hilfsmittel verwendet habe.

Ich habe mich an keiner anderen Universität um einen Doktorgrad beworben und besitze keinen entsprechenden Doktorgrad.

Ich habe Kenntnis von der dem Verfahren zugrunde liegenden Promotionsordnung der Fakultät II - Mathematik und Naturwissenschaften der Technischen Universität Berlin.

Berlin, den 29. Januar 2015